

Study of Transition Metal Phosphides as Anode
Materials for Lithium-ion Batteries: Phase
Transitions and the Role of the Anionic Network

by

Denise Carla Cordeiro da Silva Gosselink

A thesis

presented to the University of Waterloo

in fulfillment of the

thesis requirement for the degree of

Doctor of Philosophy

in

Chemistry and Biochemistry

Waterloo, Ontario, Canada, 2006

© Denise Carla Cordeiro da Silva Gosselink 2006

Author's Declaration for Electronic Submission of a Thesis

I hereby declare that I am the sole author of this thesis. This is a true copy of the thesis, including any required final revisions, as accepted by my examiners.

I understand that my thesis may be made electronically available to the public.

Denise Carla Cordeiro da Silva Gosselink

Abstract

This study highlights the importance of the anion in the electrochemical uptake of lithium by metal phosphides. It is shown through a variety of *in-situ* and *ex-situ* analytical techniques that the redox active centers in three different systems (MnP_4 , FeP_2 , and CoP_3) are not necessarily cationic but can rest almost entirely upon the anionic network, thanks to the high degree of covalency of the metal-phosphorus bond and strong P-character of the uppermost filled electronic bands in the phosphides. The electrochemical mechanism responsible for reversible Li uptake depends on the transition metal, whether a lithiated ternary phase exists in the phase diagram with the same M:P stoichiometry as the binary phase, and on the structure of the starting phase. When both binary and lithiated ternary phases of the transition metal exist, as in the case of MnP_4 and Li_7MnP_4 , a semi-topotactic phase transformation between binary and ternary phases occurs upon lithium uptake and removal. When only the binary phase exists two different behaviours are observed. In the FeP_2 system, lithium uptake leads to the formation of an amorphous material in which short-range order persists; removal of lithium reforms some the long-range order bonds. In the case of CoP_3 , lithium uptake results in phase decomposition to metallic cobalt plus lithium triphosphide, which becomes the active material for the subsequent cycles.

Acknowledgments

This is perhaps the most difficult section that I have to write on this thesis. I do not think I will forget the names of all the people that helped to get this done, but it will be really tough to thank them enough. I will nonetheless try...

First and foremost, I want to thank my thesis supervisor, Dr. Linda Nazar, for accepting me in her research, for the financial support, and the patience along the years.

I must surely thank Dr. Mario Gauthier, Dr. Richard Oakley, and Dr. Jacek Lipkowski for serving on my advisory committee and contributing valuable insights to my thesis work. Special thanks go to Gauthier who, despite having to deal with everything but polymers, spent so much time in the final revision of the thesis. My gratitude also to Dr. Holger Kleike, Dr. Robert Hill, and Dr. Stephanie Brock, who drove all the way from Wayne State University on that beautiful and hot summer day to fulfil her duties, for serving on my defence committee.

Many thanks to my lab mates, past and present, for all the help and friendship shared. Special thanks to Gillian Goward, Tracy Kerr, Olivier Crosnier, J el Gaubicher, Guillaume Dazzelle (Flower Power!), Fabien Duchene, Subramanian Herle, Brian Ellis, Mike Makhnouk, Kevin Yin, Jesse Roussel, and Val rie Pralong. Thanks also to Prof. Holger Kleinke and Prof. Tong Leung, and their respective research groups, for teaching me so much of sample preparation and characterization, and for

allowing me to use their equipments and lab space so many times.

I, or any experimental science graduate student for that matter, could never have finished my work without the assistance of the ChemStores, ChemProjects, and Science Shop crews. I will be forever in debt for your kindness and always promptness to help. So here is to you: Scott Nicol, Lisa, Slavica, Lew, Sue, Ravi, Michael, Vidya, Jamus, Stacey, Suehair, Ken, Phil, Chris, Harmen, Jacek, Kruno, Garnet, Reg, Mike, Rick, Peter, John, and Andy. I also want to extend my gratitude to the ladies in the office, Janice Campbell, Bev Wrinkler, and a VERY special thank-you to Cathy van Esch. You girls rock! Thanks also to Jake Fisher, my boss sometimes, my good friend always.

I have now the pleasure of acknowledging those who have provided me with the personal foundation which has been so indispensable to my professional life. First and foremost, I thank my parents, Angelina and Dilton (Mainha and Painho), for providing the bedrock of support on which my life is built upon and the fortress of never-ending love which has enabled me to weather all the storms of life. I also gratefully acknowledge the influence of my parents-in-law, Robert and Mary Karen, and of my big brothers, Scott and Dirk, and small-big-sister Daniela; I would not have made it without your love and support. My appreciation to the Brazilian Community in Waterloo-BRASWAT (good times will never be forgotten), especially to Carlson, Daniela, and Carolina, more than friends you are family to me.

Thanks also to my church families, in Canada (Lincoln Road Chapel, and Westhills Mennonite) and in Brazil (Presbyterian Church of Bahia, specially SAF-Ba and UMP-Ba), for their support through the difficult times, and for the constant prayers lifted to our Lord's Throne. To my very special sisters, Claudia Zini and Angelina So, my love, my prayers, and a big hug. Let God bless you all.

My biggest personal thanks are to my husband, Ken, and my daughter, Marina, for their unconditional love, patience, encouragement, and support. I can never thank God enough for bringing you both into my life.

Finally, my utmost gratitude is to God, faithful and sovereign father. He has set apart a special place just for me so how can I ever thank you enough...

Denise Carla Cordeiro da Silva Gosselink Waterloo, 2006.

Dedictory

To Mainha and Painho, my parents and friends, example of love and strength;

To Denilton, my brother (in memorian);

To Ken, my friend, my lover, my other half;

To Marina, our first daughter;

To the Gosselinks, my second family;

To God, my creator and saviour, all honor and praise!

Contents

1	Introduction	1
1.1	Lithium-Ion Technology	3
1.2	Thesis layout	5
	References	7
2	Theoretical Background	9
2.1	Fundamentals	9
2.1.1	Cell Voltage	11
2.1.2	Cell Capacity	15
2.1.3	Other Performance Parameters	16
2.2	Battery Materials	17
2.2.1	Cathodes	18

2.2.2	Electrolyte	23
2.2.3	Anodes	27
	References	49
3	Techniques and Methodologies	61
3.1	Electrochemistry	61
3.1.1	GITT	61
3.1.2	PITT	62
3.1.3	Experimental	65
3.2	X-ray Diffraction	67
3.2.1	Fundamentals	67
3.2.2	Experimental	78
3.3	Electron Microscopy	78
3.3.1	Experimental	82
3.4	X-ray Photoelectron Spectroscopy	83
3.4.1	Principles	83
3.4.2	Experimental	86
3.5	X-ray Absorption Spectroscopy	87

3.5.1	Experimental	89
3.6	Magnetic Measurements	90
3.6.1	SQUID	91
3.6.2	Mössbauer Spectroscopy	92
3.6.3	Experimental	96
	References	97
4	Manganese Phosphide System	99
4.1	Introduction	99
4.1.1	Structure of MnP_4 and Li_7MnP_4	100
4.2	Experimental	102
4.2.1	Synthesis of MnP_4	102
4.2.2	Synthesis of Li_7MnP_4	103
4.3	Characterization and Properties of MnP_4 and Li_7MnP_4	104
4.3.1	Structure and Composition of the Materials	104
4.3.2	Electrochemical Properties of Manganese Phosphide Systems .	110
4.3.3	<i>Ex-situ</i> Analysis of Cycled MnP_4 and Li_7MnP_4	116
4.3.4	Proposed Mechanism for Phase Transformation	122

4.4	Conclusions	126
4.4.1	Comparison of Results	126
	References	129
5	Iron Phosphide System	132
5.1	Introduction	132
5.2	Experimental	135
5.2.1	Synthesis of FeP ₂ Using a Flux of Tin	135
5.2.2	Synthesis of FeP ₂ Using Iodine Vapour Transport	135
5.3	Characterization and Properties of FeP ₂	136
5.3.1	Structure and Composition of the Materials	136
5.3.2	Electrochemical Studies of FeP ₂	141
5.3.3	<i>Ex-situ</i> Analysis of Cycled FeP ₂	148
5.4	Conclusions	168
	References	171
6	Cobalt Phosphide System	176
6.1	Introduction	176

6.2	Experimental	178
6.2.1	Synthesis of CoP_3	178
6.2.2	Synthesis of LiP	179
6.3	Characterization and Properties CoP_3	179
6.3.1	Structure and Composition of the Materials	179
6.3.2	Electrochemical Studies of CoP_3	183
6.3.3	<i>Ex-situ</i> Analysis of Cycled CoP_3	186
6.3.4	Proposed Mechanism	194
6.4	Conclusions	194
	References	196
7	Conclusions	199
7.1	Summary	199
7.2	Future Work	202

List of Tables

1.1	Characteristics of some battery systems used commercially	2
2.1	Structure and properties of some solvents used for lithium battery electrolytes.	25
2.2	Electrochemical properties of some Li alloys.	32
3.1	Types of photoelectron spectroscopy according to photon source. . . .	86
4.1	Parameters for synthesis of MnP_4	103
4.2	Crystallite size of ball-milled Li_7MnP_4 samples determined by Scherer equation.	108
5.1	Reaction parameters for the preparation of FeP_2 by I_2 vapor transport.	136
5.2	Results of the LeBail fit for FeP_2 XRD data in the space group $Pmnn$.	140
5.3	Matrix for the Factorial Design of Experiments.	145

5.4	Responses of the DOE for electrochemical performance of FeP ₂	146
5.5	Multiple regression and analysis of variance results for D1 and RC1. .	149
5.6	Summary of EXAFS data at the Fe K-edge for the first shell of FeP ₂ .	155
5.7	Results of Curie-Weiss and Langevin fitting of FeP ₂ magnetization data.	162
5.8	Magnetic particle diameter calculated for FeP ₂ samples.	164
5.9	Mössbauer parameters calculated for FeP ₂ samples.	167
6.1	Results of the CoP ₃ XRD pattern Rietveld refinement in the space group $Im\bar{3}$	182
6.2	SAED pattern indexing results for pristine and cycled CoP ₃	191

List of Figures

1.1	Schematic representation of a lithium-ion battery.	5
2.1	Binding energy scale based on Li/Li ⁺ pair.	13
2.2	Reversibility and cycleability of an electrochemical cell.	17
2.3	Electrolyte stability window.	24
2.4	Lithium-graphite intercalation compounds	29
2.5	Phase transformation in η -Cu ₆ Sn ₅ upon lithiation.	33
2.6	Schematic representation of the DOS for oxides, nitrides, and phosphides.	39
2.7	Proposed mechanism for reversible reaction of Li with Zn ₃ P ₂	46
3.1	Typical chronoamperograms of diffusion and nucleation controlled biphasic electrochemical processes	65
3.2	Schematic representation of a Swagelok type cell.	66
3.3	Bragg's law of diffraction from parallel planes	68

3.4	Schematic representation of XRD sample holder for air-sensitive material	78
3.5	Schematic representation of Scanning and Transmission Electron Microscopy.	79
3.6	Schematic representation of the photo-emission process	83
3.7	Schematic representation of XAS process	88
3.8	Schematic representation of Mössbauer effect and spectroscopy	92
4.1	MnP ₄ structures	101
4.2	Li ₇ MnP ₄ structure	101
4.3	XRD patterns of MnP ₄ variants.	105
4.4	XRD patterns of Li ₇ MnP ₄	107
4.5	XRD and SEM of ball-milled Li ₇ MnP ₄	109
4.6	Galvanostatic profiles for MnP ₄	110
4.7	GITT profiles for δ -MnP ₄	112
4.8	Li ₇ MnP ₄ galvanostatic profile	113
4.9	MnP ₄ and Li ₇ MnP ₄ chronoamperograms	114
4.10	Cycling performance of δ -MnP ₄ and Li ₇ MnP ₄	115
4.11	Cycling performance of Li ₇ MnP ₄	117

4.12	<i>Ex-situ</i> XRD patterns of cycled MnP_4 and Li_7MnP_4 samples.	119
4.13	<i>Ex-situ</i> SEM micrographies of cycled MnP_4 and Li_7MnP_4 electrodes.	121
4.14	<i>Ex-situ</i> TEM of manganese phosphides electrodes at different cycling stages.	123
4.15	Schematic of the mechanism for phase transformation between MnP_4 and Li_7MnP_4	125
5.1	Polyhedral representation of the FeP_2 structure	134
5.2	LeBail refinement of XRD pattern of FeP_2 obtained by the tin flux technique	137
5.3	<i>Ex-situ</i> XRD pattern of different FeP_2/I_2 samples	139
5.4	XRD profiles from full pattern matching of FeP_2/I_2	141
5.5	Electrochemical cycling performance of FeP_2	143
5.6	Adequacy of models obtained for the electrochemical performance of FeP_2 during the first cycle.	147
5.7	<i>Ex-situ</i> XRD patterns of cycled FeP_2 samples	150
5.8	<i>Ex-situ</i> Fe K-edge X-Ray Absorption spectra of FeP_2 samples	152
5.9	Pseudo-RDF obtained from the EXAFS signal of FeP_2 samples.	154

5.10	Field-dependent magnetization and temperature-dependent susceptibility curves of pristine FeP ₂	157
5.11	Temperature dependence of magnetization in ZFC and FC modes for FeP ₂ samples.	159
5.12	<i>Ex-situ</i> magnetization curves of discharged FeP ₂	161
5.13	<i>Ex-situ</i> magnetization curves of charged FeP ₂	163
5.14	Mössbauer spectra for FeP ₂ samples.	166
5.15	Comparison between the Li ₃ P and FeP ₂ structures.	169
6.1	Crystal structure of CoP ₃	178
6.2	CoP ₃ and CoP powder XRD pattern.	181
6.3	Galvanostatic profile of CoP ₃	184
6.4	First cycle PITT profile of CoP ₃ at C/5.	185
6.5	<i>Ex-situ</i> and <i>in-situ</i> XRD patterns of cycled CoP ₃	187
6.6	<i>Ex-situ</i> TEM micrographs and SAED patterns of pristine and cycled CoP ₃	190
6.7	<i>Ex-situ</i> XPS spectra of cycled CoP ₃	193

Chapter 1

Introduction

Batteries are energy storage devices that deliver electrical current produced by an electrochemical reaction. They are divided in two main groups, namely primary and secondary, according to their ability of being recharged and reused. Secondary batteries, also called rechargeable batteries, are used on a daily basis in a variety of consumer, industrial, and military applications. The tendency towards small size portable devices, especially the 3C's – camcorders, cellular phones and portable computers, demand lightweight, small volume, high energy-density batteries.^{1,2} An alternative power source for transportation also garners great current interest; combustion engines emit greenhouse gases that have enormous effects on the global climate. The recently developed hybrid electric vehicle (HEV), which uses rechargeable batteries in conjunction with small, energy efficient engines, represents a

step towards the solution of the problem.^{3,4} Size matters even more when considering medical applications such as pacemakers and artificial organs and limbs.⁵

Rechargeable batteries are usually named according to the chemical materials that form their individual parts. A complete description of the different battery systems available in the market is outside of the scope of this work – extensive reviews of the topic are available in the literature.^{1,2,6} Table 1.1 briefly summarizes some basic characteristics of secondary battery systems available commercially, showing the overall superior performance of Li-ion cells.

Table 1.1: Characteristics of some battery systems used commercially.⁷

Battery Type	Pb-acid	Ni-Cd	Ni-MH	Li-ion
Nominal Voltage, V	2	1.25	1.25	3.6
Specific Energy, Wh/kg	30–50	45–80	60–120	110–160
Energy Density, Wh/l	70	100	245	440
Cycle Life ^a	200–300	1500	300–500	500–1000
Self-discharge time ^b , (months)	5	20	30	10
Operating Temperature ^c , °C	-20–60	-40–60	-20–60C	-40–70C

^a 80% of initial capacity

^b At room temperature

^c Discharge

1.1 Lithium-Ion Technology

Owing to its high reactivity and small size, lithium constitutes the most attractive material for negative electrodes in electrochemical cells. On the other side of the battery, intercalation compounds that can repeatedly accept and release Li^+ ions on charge and discharge serve as cathodes for the cell.⁸ On reduction of such an electrode material, Li^+ ions are inserted from the electrolyte into available sites in the host-structure framework, and electrons fill the conduction band in the electronic structure of the host. The first reports of the potential use of intercalation compounds as cathode materials in rechargeable batteries came in the early 70's. These cells contained a lithium-metal anode and a transition-metal oxide (TMO) or chalcogenide cathode, e.g. TiS_2 , TiO_2 , MnO_2 , and V_2O_5 . In 1989, Moli Energy Ltd. (British Columbia, Canada) went into large-scale production of a system containing a MoS_2 host material as cathode but some serious accidents caused these cells to be quickly withdrawn from the market.⁹ The difficulties encountered were all associated with the use of highly reactive lithium metal as anode material. A dramatic increase of the lithium surface area upon cycling, with formation of dendrites which can penetrate the separator, caused short-circuiting and thermal runaway.¹⁰

Replacement of the elemental lithium anode by an intercalation compound that could host Li^+ ions at a low potential *vs.* the Li/Li^+ redox couple overcame the weakness of the metallic negative electrode.¹¹ In this system the lithium ion “rocks”

back and forth as it intercalates in either electrodes and the lack of metallic lithium plating avoids safety problems. During the discharge of this battery, referred to as swing, rocking chair, lithium-ion, or simply Li-ion battery (Figure 1.1), Li^+ ions move out of the anode and into the cathode. The driving force for the process is the difference in the electro-chemical potential experienced by the lithium ion in the anode and the cathode material. Since the electrolyte is an ionic but not an electronic conductor the electrons are forced to travel from the anode to cathode externally. Finally the electrons and Li^+ ions meet again in the cathode. Charging the battery reverses this procedure, the driving force now coming from the applied voltage which is higher than the difference in electro-chemical potential between anode and cathode.

The absence of metallic lithium immensely improves the safety of the cells. The Li^+ ions are usually supplied by some lithium-containing TMO cathode material (LiMO_x), such as LiCoO_2 , LiNiO_2 , or LiMn_2O_4 . Carbonaceous materials make the most appropriate anodes. In 1991, Sony made the first commercial Li-ion battery and, today, more than ten companies produce these batteries.^{13,14} Nonetheless, these batteries still have serious drawbacks and the effects of prolonged cycling and/or storage (*e.g.* capacity loss, poor cycleability, power fade, and self discharge) limit their theoretical or initially excellent performance.¹⁵⁻¹⁷ In addition, the new technologies demand smaller, more durable, improved battery materials.

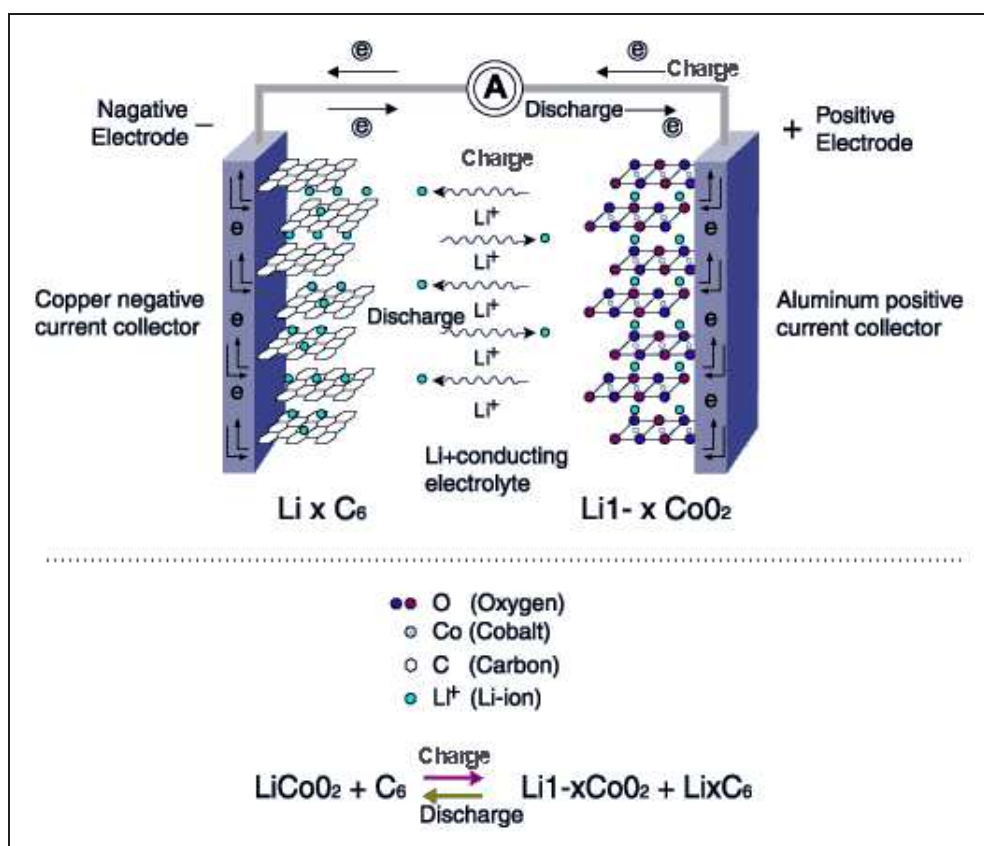


Figure 1.1: Schematic representation of a lithium-ion battery.¹²

1.2 Thesis layout

This thesis reports of new anode materials for Li-ion batteries, more specifically, transition metal phosphides. Three compounds, namely MnP_4 , FeP_2 and CoP_3 , were studied in this context. The next chapter describes some theoretical electrochemistry concepts and briefly reviews the state of the art in the research on Li-ion batteries. Chapter 3 provides theoretical input on the techniques and methodologies employed in the investigations. Chapters 4, 5, and 6 report on the electrochemical performance

and the mechanism for lithium uptake/extraction by the different compounds.

Finally, Chapter 7 summarizes the conclusions.

References

- [1] Manthiran, A. *J. Miner.* **1997**, *March*, 43.
- [2] Jacoby, M. *Chem. Eng. News* **1998**, *August*, 37.
- [3] Arai, J.; Muranaka, Y.; Koseki, M. *Hitachi Rev.* **1900**, *53*, 182.
- [4] Takeda, N.; Imai, S.; Horii, Y.; Yoshida, H. *Tech. Rev.* **2003**, *15*, 68.
- [5] Bruce, P. G. *Science* **2003**, *350*, 1645.
- [6] Nishi, Y. *J. Power Sources* **2001**, *100*, 101.
- [7] Linden, D.; Reddy, T. *Handbook of Batteries*; McGraw Hill: New York, 3rd. ed.; 2002 Chapter 2.
- [8] Winter, M.; Besenhard, J. O.; Spahr, M.; Novak, P. *Adv. Mater.* **1998**, *10*, 725.
- [9] 1989.

- [10] Dahn, J.; Sleight, A.; Shi, H.; Way, B.; Weydanz, W.; Reimers, J.; Zhong, Q.; von Sacken, U. Carbons and Graphites as Substitutes for the Lithium Anode. In *Lithium Batteries - New Materials, Developments and Perspectives*; Pistoia, G., Ed.; Elsevier: Amsterdam, 1994.
- [11] Fong, R.; von Sacken, U.; Dahn, J. *J. Electrochem. Soc.* **1990**, *137*, 2209.
- [12] [http : //www.tech – libat.com](http://www.tech-libat.com).
- [13] Sekai, K.; Azuma, H.; Omaru, A.; Fujita, S.; Imoto, H.; Endo, T.; Yamaura, K.; Nishi, Y.; Mashiko, S.; Yokogawa, M. **1993**, *43*, 241.
- [14] Moshtev, R.; Johnson, B. *J. Power Sources* **2000**, *91*, 86.
- [15] Pistoia, G.; Antonini, A.; Rosati, R.; Zane, D. *Electrochim. Acta* **1996**, *41*, 2683.
- [16] Arora, P.; White, R.; Doyle, M. *J. Electrochem. Soc.* **1990**, .
- [17] Amatucci, G.; Schmutz, C.; Blyr, A.; Sigala, A.; Gozdz, A.; Larcher, D.; Tarascon, J.-M. *J. Power Sources* **1997**, *69*, 11.

Chapter 2

Theoretical Background

2.1 Fundamentals

Electrochemical cells are ordinarily used to study reactions involving ions in solution and solids. They are formed by a positive and a negative electrode (cathode and anode, respectively) which are kept in contact by a suitable ionic conducting electrolyte. The electrodes are separated by an ionically permeable and electronically insulating separator to prevent self discharge of the cell; the electrical contact is thus made by an external circuit. Depending on the spontaneity of the reaction, an electrochemical cell is defined as *galvanic* or *electrolytic*. The spontaneous chemical reactions that occur in the electrodes of galvanic cells generate an electrical current (power out) whereas in electrolytic cells, the reactions occur at the expense of an

externally applied current (power in). The charge and discharge processes in a typical secondary lithium battery (with lithium initially stored in the crystal structure of the host material that forms the cathode, Figure 1.1) can thus be classified respectively as electrolytic and galvanic.

Electrochemical systems store charge *via* four basic mechanisms:¹

Double-layer: small amounts of charge ($\approx 15 \mu\text{F}/\text{cm}^2$) are stored in the electrical double-layer within the electrolyte, in the vicinity of the electrode/electrolyte interface. The amount of stored energy is a linear function of the applied voltage.

Adsorption: charge storage results from the electrodeposition of active species on specific crystallographic sites partially covering the electrode surface at lower potentials than those needed for bulk deposition. This mechanism leads to an “adsorption pseudo-capacitance” in the range of $200\text{--}400 \mu\text{F}/\text{cm}^2$ of interface.

Insertion: electroactive species diffuse and insert into the bulk of an electrode forming a solid solution, allowing for the storage of high amounts of charge since the latter is proportional to the amount of species inserted. The electrochemical potential of the guest species in the solid determines the electrode potential. For random solid solutions, the major contributions to the potential are from the Fermi level of the degenerate electron orbitals and the entropy and enthalpy of the guest species.

Reconstruction: faradic deposition promotes phase transformation reactions in

some battery systems, which results in an open-circuit electrode potential independent of the state of charge. The amount of charge and reaction kinetic depends on the specific characteristics of the system.

The basic characteristic of an electroactive intercalation compound is the thermodynamic voltage-composition relation, which corresponds to the equilibrium phase diagram of the system. This relation depends on the changes in electronic and structural properties upon intercalation/deintercalation. Basically, a continuous dependence of the potential *vs.* composition corresponds to a solid-solution single-phase domain, whereas a potential plateau corresponds to a two-phase domain.² Other properties of interest, particularly in view of possible applications as active electrode in a battery are the potential window of electrochemical stability, kinetics and reversibility of the intercalation process.

2.1.1 Cell Voltage

During the cell discharge the flow of negative charge into the cathode is compensated by a migration of positive alkali metal ions from the electrolyte into the host structure. At the anode the removal of electrons is compensated by a release of cations to the electrolyte. The sum of the two electrochemical half-reactions is the intercalation reaction. The spontaneity of the galvanic reaction results from the difference between

the chemical potential for lithium in the negative and positive electrode materials:³⁻⁶

$$-eV = -\frac{\mu_{Li}^{cathode} - \mu_{Li}^{anode}}{nF} \quad (2.1)$$

where n is the number of electrons transferred, in this case $n = 1$, and F is the Faraday constant. For simplicity, the chemical potential for metallic lithium in the anode is defined as zero and the other compounds are referenced against it. Therefore, equation 2.1 becomes:

$$V(x) = -\frac{\mu_{Li}^{cathode}}{F} \quad (2.2)$$

Equation 2.2 relates the voltage measurements with thermodynamics. Knowledge of the Gibbs free energy of lithium “insertion” into the host material provides information about the intercalation profile since the chemical potential is given by the partial derivative of the Gibbs free energy of lithium in the host with respect to the number of Li ions:

$$\mu = -\left(\frac{\partial G}{\partial N}\right)_{P,T} \quad (2.3)$$

where ∂G is the free energy variation when N moles of Li are inserted at constant temperature T and pressure P . A more detailed insight into different contributions to the driving force for the intercalation reaction has been discussed by Gerischer *et al.*⁷ The “insertion” potential is commonly expressed relative to the pair Li/Li⁺ (Figure 2.1) and this convention is also used in this text.

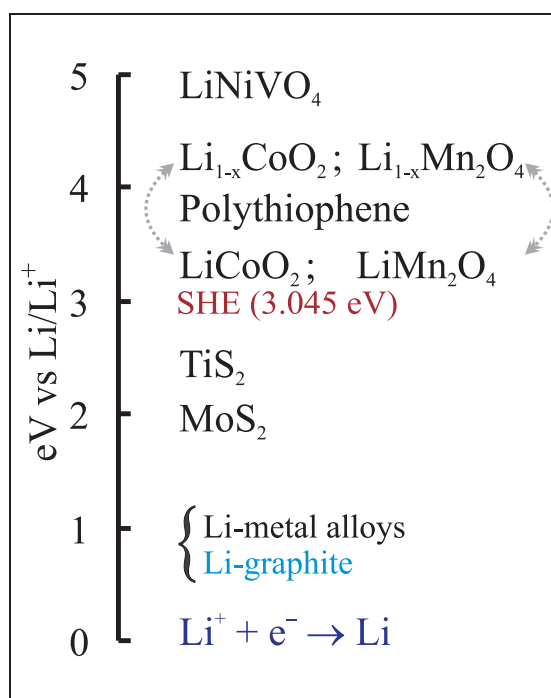


Figure 2.1: Binding energy scale based on Li/Li⁺ pair. Voltage of the Standard Hydrogen Electrode (SHE) shown for comparison.

Polarization

Polarization is the departure of working potential of an electrode from its nernstian value upon the application of a current due to local inhomogeneities. The ionic motion is driven by chemical diffusion which in turn depends on the difference in chemical potentials of the same ions between bulk and surface of the electrode. During measurements, the applied electrical current determines the concentration gradient necessary to establish the appropriate diffusional flux. Since the cell voltage measures the chemical potential of the active species at the electrode surface, measured and

equilibrium voltage differ.

In binary processes, voltage polarization is also related to the extra energy needed to force the electrode reaction to proceed at a required rate (or its equivalent current density). Higher current densities induce larger polarizations which also depend on the “inherent rate” of the electrode reaction. Even for the simplest case, the polarization is the sum of different contributions of three processes which cause changes in potential arising from current flowing across a metal-solution interface:

Activation: the change in potential required just to make the reaction go faster. It can be analyzed in terms of the energy barrier between the reactant and the product states giving rise to a relationship between current and potential. A reaction for which activation polarization dominates is referred to as *activation controlled*.

Concentration: the rate of reactions involving species which participate as reactants in the rate-determining step depends on their concentration. As the reaction consumes the active species, a greater change in potential is required to maintain the current. A reaction for which concentration polarization dominates is referred to as *mass-transport* or *diffusion controlled*.

Resistance: solutions of electrolytes, particularly dilute ones, generally have a rather poor conductivity compared to metals. Solutions with high electrical resistance produce a potential difference between the anodic and cathodic sites,

which is known as resistance polarization. If resistance polarization dominates a reaction, it is referred as *resistance* or *IR controlled* (the latter term arises from Ohm's Law, $V = IR$).

2.1.2 Cell Capacity

Faraday's first law establishes that the mass of anodic material of a galvanic cell depends on the current I passing by the system according to:⁸

$$m = \frac{MI\delta t}{xF} \quad (2.4)$$

with m the mass of active material, M the molar (or formula) mass, x the number of electrons exchanged, δt the elapsed time, and F Faraday's constant. The capacity Q of a cell is given by:

$$Q = I\delta t \quad (2.5)$$

So, rearranging Equation 2.4 one obtains the expression for gravimetric capacity, Q_m :

$$Q_m = \frac{I\delta t}{m} = \frac{xF}{M} \quad (2.6)$$

which, multiplied by the density d of the active material, becomes:

$$Q_v = Q_m \cdot d \quad (2.7)$$

Equation 2.6 defines the **Gravimetric Capacity** of a cell, the amount of electric charge exchanged in 1 hour per unit mass of material. The **Volumetric Capacity**

(Equation 2.7), is of extreme importance for industrial purposes since it determines the limit for miniaturization. This study rates the performance of the materials in terms of gravimetric capacity.

2.1.3 Other Performance Parameters

In addition to the potential at which the redox process occurs and the amount of power delivered by it, electrochemical cells are also evaluated for their rate performance, reversibility, and cycleability.

The rate performance measures how fast the redox reaction proceeds. Clearly, it has a kinetic component innate to the reaction happening in the electrode but particle size also influences the ionic diffusion. The rate performance is usually evaluated by the reversibility of the cell at a given current density or rate. Current density refers to the amount of current flowing per gram of material, hence in units of A/g. The related current rate, C/n , expresses the amount of electrons C (in this case also the amount of Li^+ ions) flowing per n hours. This study adopts the latter definition.

Reversibility corresponds to the reversible amount of lithium ions that can be uptaken or extracted per mole of active material. It is usually measured by the efficiency of a cell which is given by the ratio of reversible to initial capacity in each cycle (Figure 2.2(a)):

$$\text{Efficiency} = \frac{Q_{rev}}{Q_{initial}} \quad (2.8)$$

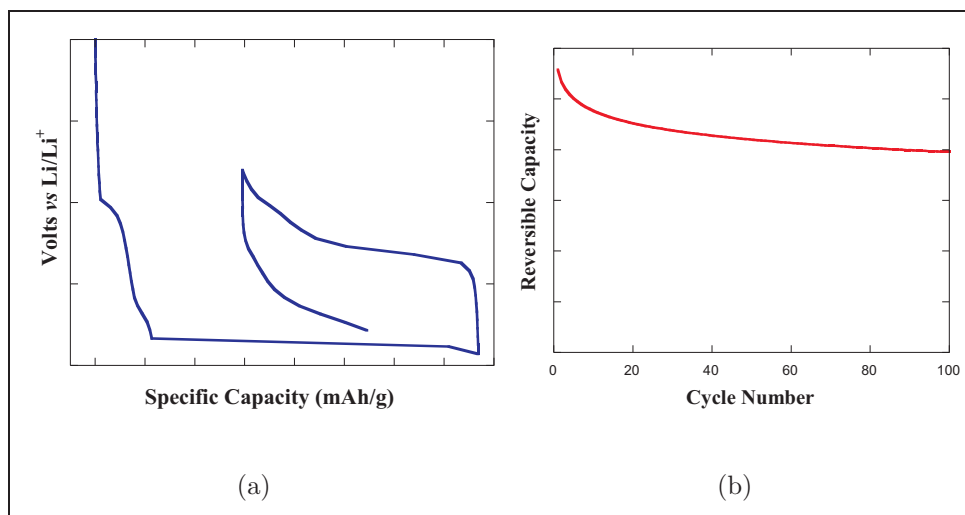


Figure 2.2: Schematic representation of (a) reversibility and (b) cycleability of an electrochemical cell.

Related to the reversibility, the cycleability of a cell depends on the stability of the active material towards repeated cycles of lithium insertion and de-insertion. A cell with good cycleability maintains good reversibility upon charge and discharge exhibiting minute reduction of reversible capacity (Figure 2.2(b)). Both the achieved capacity and cycleability of a cell depend strongly on the cycling rate, morphology and composition of the electrode, and on the active material particle size.

2.2 Battery Materials

Electrode materials for Li-ion batteries must comply with some important criteria established by the equations presented in the previous section: (i) high charge

density, (ii) good electronic and ionic conductivity, (iii) low formula weight, (iv) fast kinetics of de-intercalation (v) reversibility, (vi) adequate oxidation potential (high for cathodes and low for anodes), (vii) structural stability, (viii) low toxicity, and (ix) low cost. Materials that incorporate all these characteristics elude discovery, hence the large amount of research in the area of Li-ion batteries.

Comprehensive reviews on materials for Li-ion batteries are available in the literature.^{9,10} The following sections present a brief description of some systems studied as positive and negative electrodes and their mechanisms of lithium uptake, as well as the electrolytes employed.

2.2.1 Cathodes

Transition Metal Oxides

Because they are air-stable compounds, cathode materials are usually produced in the lithiated form and act as a initial source of lithium when coupled with standard graphitic anodes. Transition metal oxides (TMO) constitute the most studied and commercially used compounds. The strong electronegativity of oxygen guarantees a highly ionic character to the TM-O bond which in turn is associated with a high potential of the metal redox couple. Elements of the first row in the periodic table form TMOs with lowest mass, high valence states, and open structures (channels, layers, or frameworks) that withstand lithium uptake and removal.¹¹

Layered LiCoO_2 is the commonly used cathode material in commercial Li-ion batteries today by virtue of its high working voltage (3.6 V), structural stability and long cycle life.¹² It has a good cycle life but the stability window of the electrolytes limits its specific capacity to only ≈ 140 mAh/g ($x < 0.5$ in $\text{Li}_{1-x}\text{CoO}_2$). In addition, the toxicity and high cost of cobalt spurred recent efforts to find a better alternative. The isostructural LiNiO_2 is an attractive choice because of its high specific capacity and better elevated-temperature performance. Nonetheless, because of the difficult synthetic procedure,¹³ poor structural stability on cycling,¹⁴ and poor thermal stability of the delithiated state,¹⁵ LiNiO_2 has not been commercially successful.

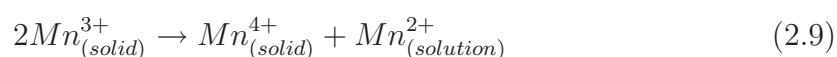
Attempts have been made to improve the electrochemical lithium insertion properties of layered LiMO_2 ($M = \text{Co}$ or Ni). The series of compounds with general formula $\text{LiNi}_x\text{Co}_{1-x}\text{O}_2$ has been extensively investigated.^{14,16,17} These compounds, easier to prepare and presenting lower insertion potentials than the pure cobalt or nickel phases, are less demanding on the electrolyte. Nevertheless, neither specific capacity nor cycleability are improved. Another approach employs partial substitution of Co or Ni by another transition metal (*e.g.* chromium, manganese, and iron).¹⁸⁻²² Unfortunately, such substitutions are deleterious to both capacity and reversibility. Layered LiMnO_2 , LiFeO_2 , and V_2O_5 have also been investigated as possible candidates for cathode materials but they exhibit low reversible capacities.

Manganese dioxide has been the most studied compound with one-dimensional

interstitial space for Li^+ transport and exhibits an initial specific capacity of 200 mAh/g. Polymorphs of MnO_2 with different size channels, comprising of edge and corner shared MnO_6 octahedra, show different stabilities towards lithium intercalation and removal; hence, their performance is strongly affected by methods of synthesis as well as by the cycling current rates.^{23,24} A modification of $\gamma\text{-MnO}_2$, named CDMO (Composite Dimensional Manganese Oxide) by Sanyo Corp., obtained by reaction with LiOH at 375-420°C, shows better stability upon cycling.²⁵⁻²⁷

In the framework class of compounds, research concentrates on manganese, vanadium, cobalt, and titanium oxides and/or lithiated derivatives with a spinel type structure, $\text{A}[\text{B}_2]\text{X}_4$. A vast number of compositions can be prepared with the spinel structure by changing both the type and valency of cations A and B as well as anions X. Lithium transition metal oxide spinels, $\text{Li}_x[\text{B}_2]\text{O}_4$, can be used for both insertion and extraction purposes and, because the oxidation potential depends on the metal cation on the octahedral B sites, the cell voltage can be tailored accordingly.^{28,29} Of these, Li-Mn-O spinels have been extensively studied due to their low cost, abundance of manganese, good electronic conductivity, and high oxidation potential range (3-4 V *vs.* Li). The end member LiMn_2O_4 adopts the spinel type structure with 3D paths for Li^+ diffusion. Its electrochemical performance depends strongly on the preparation method – high crystallinity materials with low amounts of impurities are desirable for maintaining good stability and rechargeability of the cells. Complete lithium extraction from the structure is hindered in practice by the instability of

electrolytes at such potentials. On the other hand, lithium insertion is possible at the 3V range but the cycling performance above this region is compromised by a Jahn-Teller distortion of the structure, reducing the symmetry from cubic to tetragonal.^{28,30,31} At the end of discharge, when high amounts of Mn^{3+} ions are present, a disproportionation reaction followed by loss of Mn^{2+} ions (Eq. 2.9) causes framework dissolution into the electrolyte. Together with the already low specific capacity offered by the compound (≈ 160 mAh/g), these facts preclude the commercial use of $LiMn_2O_4$ in Li-ion batteries.



Phosphates and Sulphates

In recent years, lithium transition metal phosphates and sulphates received significant attention among the research and industrial communities as possible candidates for cathode materials in Li-ion batteries. Compounds with the NASICON (Na = Sodium Super Ionic Conductor) type framework exhibit high diffusion rates for Li^+ transport and demonstrate good cycling reversibility. Namely $Li_3Fe_2(PO_4)_3$, $Li_3V_2(PO_4)_3$, $Li_xFe_2(SO_4)_3$, $Li_3FeV(PO_4)_3$, and $Li_3FeTi(PO_4)_3$, the phospho-olivines modifications $LiFePO_4$ and $LiCoPO_4$, and vanadyl phosphates $VOPO_4$ have been extensively investigated.^{32,33} These compounds intercalate lithium ions at higher potentials than their oxide counterparts, increasing the voltage range available for Li-ion cells, due to a reduction of the electron charge density of oxygen by the highly charged cation

in the $(\text{XO}_4)^{3-}$ group. This is a result of the more ionic character of the TM-O bond which lowers the energy of the transition metal antibonding d orbitals.

Conducting Polymers

Electronically conducting polymers can be molded into different shapes making these materials a very versatile and cheap choice. Their conductivity, however, is usually very low ($\leq 10^{-5} \text{ S cm}^{-1}$) for battery application purposes. Nevertheless, an increase of conductivity by orders of magnitude can be achieved by appropriate doping processes.³⁴ Chemical oxidation or reduction of electrically conducting polymers (p- and n-doping, respectively) form positively or negatively charged polyion complexes associated with their respective counter ions.

The doping process can be achieved electrochemically by reversible polarization of the polymer film.³⁵ The mechanism for lithium insertion by polymeric materials differs from the inorganic counterpart; concomitant anion insertion is required for electronic neutrality of the system. Hence, anodic or cathodic polarization of electronically conducting polymers in the presence of a suitable electrolyte (*e.g.* LiClO_4) can lead to the respective oxidation or reduction of the polymeric material, accompanied by ionic insertion (perchlorate or lithium ions). The ionic conduction process during charge and discharge is very slow and large amounts of electrolyte are necessary. Because of the reduced amounts of lithium in the polymeric material, the specific and volumetric capacities are compromised. Finally, poor cycleability and

large self-discharge contribute to the lack of research interest in these materials.

2.2.2 Electrolyte

Because of the strong reducing power of Li, the working potential for Li-ion cells lies commonly around 4 V, but can be as high as 5 V in some cases. The main requirement for the electrolyte is, therefore, that it must have a wide electrochemical stability window (Figure 2.3). Therefore, aqueous electrolytes cannot be used and only a few aprotic, non-aqueous alternatives are suitable for practical cells, including liquid, solid, and polymeric electrolytes. Liquid alternatives are those most commonly exploited so far because of their superior ionic conductivity at ambient temperature. An extensive review on the subject is available in the literature.³⁶

Solvents

Liquid solvents that fulfill the dual requirement of a high lithium ion conductivity (10^{-3} S cm⁻¹), and a broad electrochemical stability window are mainly carbonates, ethers and esters of various kinds (see Table 2.1). Carbonates are by far the most common choice under ambient conditions, because of their superior cycling behaviour. Ethylene carbonate (EC) and propylene carbonate (PC) provide a sufficiently high conductivity and a broad stability window. Severe exfoliation of graphitic carbon electrodes is observed when using PC, due to extensive co-intercalation during

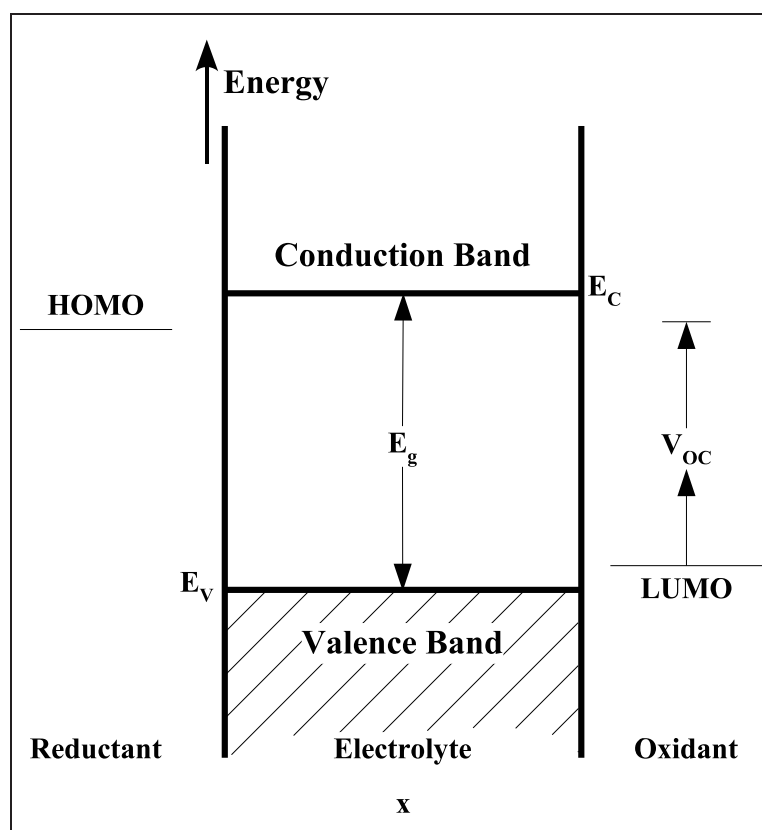
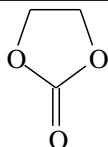
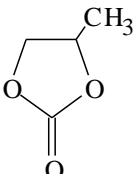
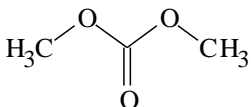
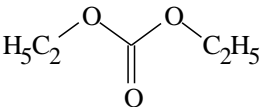
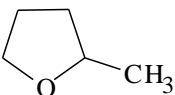
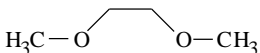
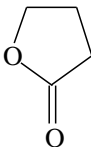


Figure 2.3: Schematic representation of electrode energy relative to electrolyte stability window (E_g).

charging.³⁷⁻³⁹ EC is the preferred solvent in that context but it is a solid at room temperature (RT). It is therefore common to mix these with other solvents with a lower conductivity to obtain a working electrolyte over a wider temperature interval, especially mixtures of EC with dimethyl carbonate (DMC) or diethyl carbonate (DEC). Addition of surface film formation agents, such as carbon sulphide (CS_2) and sulphur dioxide (SO_2) attenuates the degree of solvent co-intercalation.⁴⁰

Table 2.1: Structure and properties of some solvents used for lithium battery electrolytes.^{36,41}

Name and Abbreviation	Structural Formula	Melting Point, °C	Boiling Point, °C	Dielectric Constant, ϵ
Ethylene Carbonate EC		39–40	248	89.6 (40°C)
Propylene Carbonate PC		-49	240	64.4
Dimethyl Carbonate DMC		4.6	91	3.12
Diethyl Carbonate DEC		-43	126	2.82
2-Methyl-Tetrahydrofuran 2Me-THF		37	79	6.29
Dimethoxyethane DME		-58	85	7.2
γ -Butyrolactone γ-BL		-43	204	39.1

Lithium Salts

Soluble lithium salts in the electrolyte solutions act as charge carriers during the electrochemical process. Good solubility and charge separation of anion and cation, normally achieved by choosing bulky anions with low negative charge density, promote high conductivity.³⁶ Examples of such salts are LiClO_4 , LiAsF_6 , LiPF_6 , LiBF_4 , LiCF_3SO_3 and $\text{LiN}(\text{SO}_2\text{CF}_3)_2$. However, LiClO_4 and LiAsF_6 are not realistic options for commercial cells since ClO_4^- is highly explosive and the AsF_6^- anion and its degradation products are very toxic. The other salts are currently used or considered for use in practical cells. LiPF_6 gives high ionic conductivities in carbonate-based solutions, and shows excellent cycling properties at room temperature. It does, however, have poor thermal stability, bad cycling behaviour for some electrode materials at slightly elevated temperature, and is easily hydrolysed by traces of water.^{42–46} LiBF_4 , is much like LiPF_6 but is less hygroscopic and costs one-third of the price.^{43,47}

Lithium trifluoromethane sulfonate (LiCF_3SO_3) and lithium bis-(trifluoromethane sulfone)imide ($\text{LiN}(\text{SO}_2\text{CF}_3)_2$), designed specifically for use in polymer electrolytes, have large anions with a partly delocalized charge, which reduces the formation of ion pairs, hence increasing the conductivity of the lithium ion, especially in polymer electrolytes. They surpass LiPF_6 and LiBF_4 for use in liquid electrolytes, mainly because of their superior chemical and thermal stability. Nevertheless, these salts

do corrode the Al current collector used on the cathode side of Li-ion cells at high potentials.^{42,48}

2.2.3 Anodes

True Insertion Compounds

Carbon

Commercial rechargeable batteries use graphitic carbon as the anode active material. Their electrochemical properties and intercalation processes depend on the structure, crystallinity, size and shape of grains, texture, and morphology of the carbonaceous material⁴⁹⁻⁵¹ In general, they exhibit higher specific capacity and more negative redox potential than most metal oxides, chalcogenides, and polymers; also, carbon-based anodes exhibit excellent dimensional stability, good cycling performance, and are cheap and readily available. In addition, the intercalation chemistry and reactivity of carbon towards lithium is well established.

Graphitic carbon comprises of extended sheets of sp^2 -hybridized carbon atoms arranged in hexagonal rings which extend in two dimensions known as graphene sheets. These sheets can be stacked in an “ABAB” (hexagonal graphite) or “ABCABC” (rhombohedral graphite, less common) pattern. In practice, a pure phase never forms because of the occurrence of stacking faults and structural defects. Therefore, graphitic carbons are characterized by the extension of isolated, perfectly

stacked regions (crystallites), which may vary from nano- to micrometres in the crystallographic a and c directions. Disordered regions (formed of non-stacked graphene sheets) separate the crystallites and, in the case of non-graphitic carbons, dominate the structures.

The electrode potential of graphitic carbon is very close to that of the Li/Li^+ redox couple ($\approx 0.2\text{-}0.05\text{ V vs Li}/\text{Li}^+$). A maximum of one lithium per six carbons (LiC_6) can be intercalated in the Van der Waals gaps above and below a carbon hexagon, limiting the specific theoretical capacity to $\approx 372\text{ mAh/g}$. On intercalation, the graphite structure shifts to an “AA” stacking type (Figure 2.4(a)), passing through a number of characteristic phases, as the amount of lithium increases.⁵²⁻⁵⁴ The different phases (stages I, II, III, and IV), are shown schematically in Figure 2.4(b).

The repulsive energy originating from the interaction between lithium ions is smaller than that required to open the gap between two adjacent graphene layers. As a result, lithium fills one inter-planar gap before filling neighbouring gaps; the intercalation process occurs sequentially through first-order phase transitions. Co-existence of two Li_xC_6 phases at equilibrium within an electrode demands that the chemical potential of lithium, μ_{Li} , in each stage must be equal.⁵⁵ Therefore, the electrode potential is constant during a phase transition from one stage to another, according to the relation

$$E = -\mu_{\text{Li}}/F \quad (2.10)$$

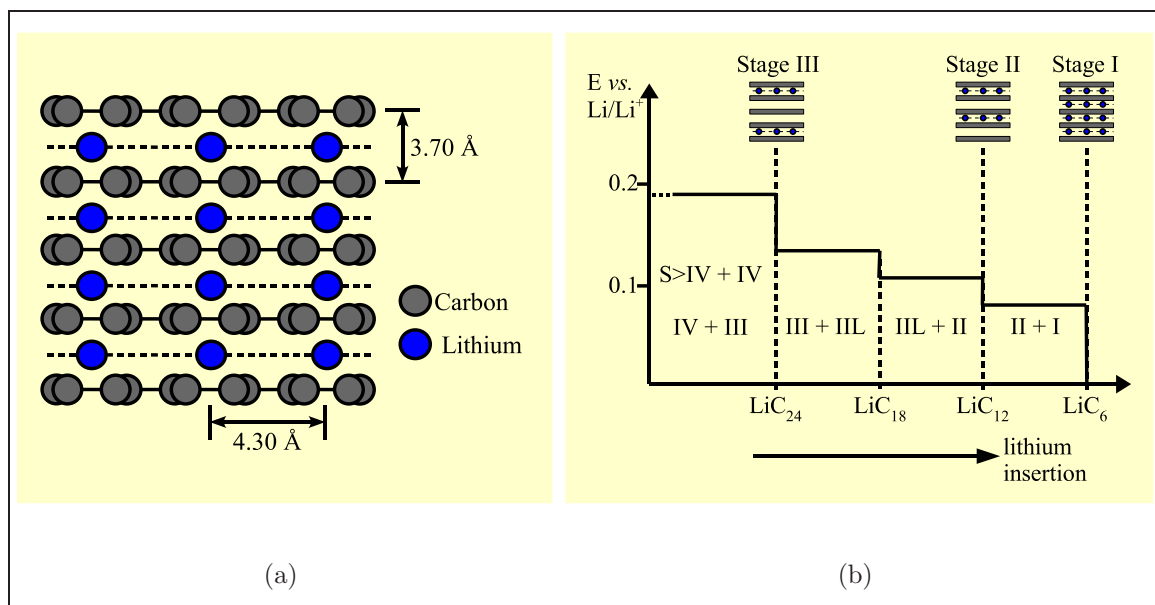


Figure 2.4: Lithium-graphite intercalation compounds: **(a)** structure of LiC₆ and **(b)** schematic representation of potential profile of stage formation.¹²

with F being Faraday's constant. Consequently, the potential profile of lithium intercalation into graphite shows a number of steps, where horizontal and vertical regions correspond to the two-phase and single phase processes, respectively.

In addition to the limited capacity exhibited by graphitic carbons, some of the lithium inserted on the first charge does not de-insert during the following discharge due to a decomposition reaction between carbon and the electrolyte. Reduction of carbonate-based electrolytes at the negative electrode between 1.5 – 0.7 V *vs.* Li/Li⁺ (*i.e.* prior to lithium intercalation), depends on the composition of the electrolyte.³⁷ A surface film, Solid Electrolyte Interphase (SEI), consisting of a variety of solvent and salt reduction products, forms around the carbon particles

as a charge-consumption side reaction, leaving the cathode material under-utilized. To minimize charge loss, the cell must be loaded with an excess of cathode material, which is detrimental to the overall volumetric capacity. On the other hand, the SEI functions as an ionic conductor that allows Li^+ ions to be transported through the film during the subsequent intercalation and de-intercalation processes. The film is also an electronic insulator that prevents the continuous reduction of electrolyte as its thickness reaches a certain limit, thus acting as a passivation layer. This limit has been set as the thickness at which electron tunnelling from the graphite surface to the electrolyte is prevented (a few nm).⁵⁶ Surface films formed on lithium metal and carbon electrodes are very similar and their presence around electrode particles surface renders stability to lithium metal in certain electrolyte systems, that would otherwise be thermodynamically unstable.^{56,57}

Other Compounds

Apart from carbon, $\text{Li}_4\text{Ti}_5\text{O}_{12}$ is the most studied intercalation material due to the minute changes that occur in its unit cell upon insertion of up to one lithium. In the structure, which can be represented as $\text{Li}_{tet}[\text{Li}_{1/3}\text{Ti}_{5/3}]_{oct}\text{O}_4$, Li and Ti occupy half the octahedral (oct) sites and the remaining Li fills the tetrahedral (tet) sites. Ohzuku *et al.* suggested that both inserted Li and those migrating from tetrahedral sites populate the partially filled octahedral sites.⁵⁸ The small structural hysteresis and rapid lithium diffusion in the material produces good electrochemical properties (specific capacity around 150 mAh/g), despite the high average insertion potential

(1.5 V). The related $\text{Li}[\text{CrTi}]\text{O}_4$ demonstrates similar behaviour.⁵⁹

Alloys and Intermetallic Compounds and Composites

In an attempt to achieve better performance, increased cycleability, and improved safety, some studies have substituted lithium-metal alloy anodes for lithium as anode material in Li-ion batteries. Even though lithium-aluminium alloys have formerly been studied in high temperature application cells, their use at low temperature failed due to the low diffusion coefficient of Li^+ in the α -Al phase.⁶⁰ Other alloys proposed as anode materials (e.g. Li_xM , $\text{M} = \text{Si}, \text{Ge}, \text{Sn}, \text{Pb}, \text{and Bi}$) exhibit large differences in the volume of the non-alloyed and alloyed phases (up to 400% for $\text{Si} \rightarrow \text{Li}_{22}\text{Si}_5$), causing the electrode to expand and contract during cycling. These mechanical stresses induce rapid decay of the mechanical properties and finally, pulverization of the electrode, leading to failure of the battery due to loss of contact between the grains.¹²

Despite their poor mechanical properties, lithium alloys exhibit very high specific capacity as seen in Table 2.2. Use of very small particle size, in the micro or nanoscopic regime, might counteract the mechanical degradation of the lithium-metal alloy. In this case, the dimensional changes of the crystallites during cycling do not cause particle cracking, thus suppressing the anode pulverization, and the reduction of the diffusion pathway improves the ionic conductivity of lithium.^{61,62} Nanoparticles, however, tend to agglomerate to form larger, more thermodynamically stable crystals, reestablishing the problem of pulverization. Attempts have been

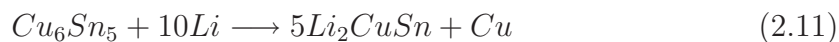
made to circumvent this problem either by surface passivation^{63,64} or by dispersing the particles into a matrix which act like an absorber for the dimensional changes during cycling. Examples of such matrices are intermetallic compounds (MM', where M' is an element that does not alloy with Li and, during the first discharge, forms an inactive matrix surrounding M, helping maintain the integrity of the electrode grains),⁶⁵⁻⁶⁸ polymers,³² oxides,⁶² and carbons.⁶⁹ A suitable matrix, one that guarantees mechanical stability without loss of electronic and/or ionic conductivity nor reduction of the cell's energy density, is yet to be developed.

Table 2.2: Electrochemical properties of some Li alloys.

Initial Phase	Lithiated Phase	Theoretical Capacity (mAh/g)	Volume Changes (%)
Li	Li	3860	—
C	LiC ₆	372	12
Si	Li ₂₁ Si ₅	4010	300
Ge	Li ₁₇ Ge ₄	1570	280
Sn	Li ₁₇ Sn ₄	959	260
Al	Li ₉ Al ₄	2235	240
Bi	Li ₃ Bi	385	115

In addition to the systems that uptake lithium through alloying reactions, intermetallic “insertion” hosts based on Cu-Sn phases have also been proposed.⁷⁰ In

these systems, topotactic Li^+ intercalation leads to high gravimetric and volumetric capacities without excessive dimensional changes. For example, at 0.4 V *vs.* Li^+/Li , $\eta\text{-Cu}_6\text{Sn}_5$ uptakes 10 Li^+ (Equation 2.11).



Only 61% volume change accompanies the lithiation reaction, thought to occur by displacement of half the tin atoms in the NiAs-type structure of $\eta\text{-Cu}_6\text{Sn}_5$. This creates hexagonal channels in the structure where Li can be inserted (Figure 2.5). Further discharge to 0 V leads to decomposition of Li_2CuSn and extrusion of Cu

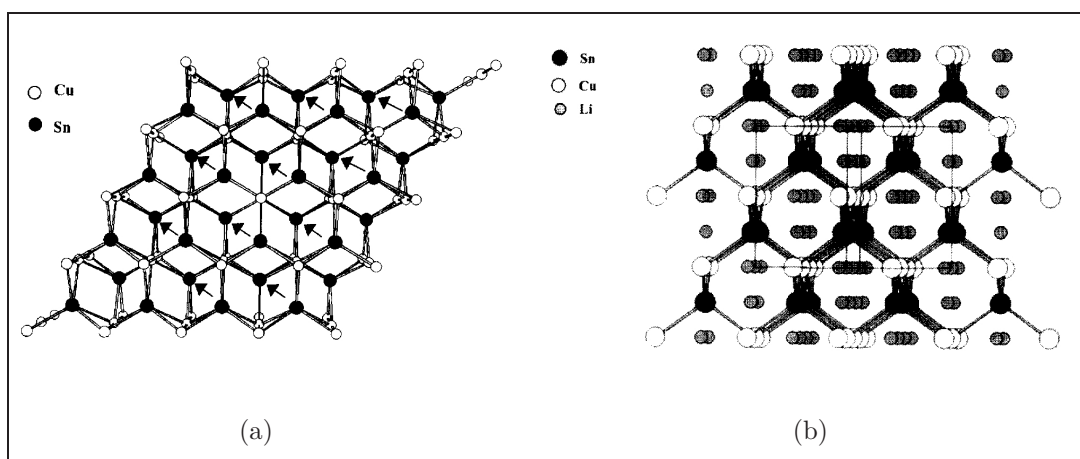
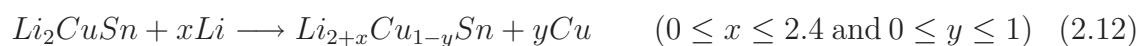


Figure 2.5: Phase transformation in (a) $\eta\text{-Cu}_6\text{Sn}_5$ upon lithiation forming (b) Li_2CuSn .

according to Equation 2.12. The specific capacity for the fully lithiated electrode is reported as 360 mAh/g. At such levels of discharge, however, Li_xSn alloys form.



Conversion or Disproportionation Materials

The capacities of these materials originate from the reaction with lithium to form another material which is the active specie. Reformation of the starting phase is not always observed.

Oxides

A high potential and large hysteresis are observed during charge, consonant with the need of oxygen transport within the bulk during oxidation. Consequently, good reversibility in these materials demands an intimate mixture of the metal sub-oxide (or pure metal, depending on the degree of Li uptake) and oxygen from the lithium oxide matrix. Transition metal oxides with spinel structure, e.g. α -Fe₃O₄ and Co₃O₄, intercalate lithium at moderate voltage by the referred process.^{71,72} In these systems, the transition metal cations migrate from the tetrahedral to the empty octahedral sites during lithium insertion. Cobalt monoxide also uptakes lithium at relative low voltages but the reaction mechanism involves the decomposition of the material with the formation of Li₂O and nanoscopic reduced Co, all surrounded by a solid electrolyte interface.⁷³

Interest in compounds containing main group elements arose after the development of Tin composite oxide (TCO), an amorphous material containing Sn²⁺ ions (Sn_xAl_yB_zP_pO_o).⁷⁴ Studies indicate that in such material the initial Li uptake corresponds to an irreversible reaction forming metallic Sn and Li₂O. Subsequent

cycling occurs basically by reversible alloying and de-alloying reactions forming $\text{Li}_{4.4}\text{Sn}$ nanoparticles embedded in a Li_2O matrix.^{75,76} The process seems to occur in a size-limiting regime with strong influence of the particles' surface energy on the thermodynamics; surface and interstitial oxygen bound to the matrix is thought to facilitate the uptake of Li by Sn.^{77,78}

Antimonides

The uptake of lithium by intermetallic (or intermetalloid) antimonide compounds always involves the extrusion of antimony from the lattice with formation of lithium antimonide, Li_3Sb , independent of the starting stoichiometry or structure.^{79–83} The systems exhibit high initial capacities (theoretical capacity 660 mAh/g), which decay rapidly upon cycling due to expansion/contraction effects. Improvement of cycleability usually involves the use of an inactive transition metal matrix.

Copper antimonide, Cu_2Sb , behaves similarly to the Cu-Sn system (see page 33). In this case, however, extrusion of 50% of Cu atoms from the structure leads to the binary phase, CuSb , before the formation of ternary Li_2CuSb .⁸⁴ Further discharge leads to a $\text{Li}_{2+x}\text{Cu}_{1-x}\text{Sb}$ solid solution terminating in Li_3Sb . The extruded Copper particles are thought to render better ionic conductivity to the electrode and cause the good reversibility obtained with a specific capacity of 290 mAh/g.

Silicides

Mg_2Si has been extensively investigated due to its anti-fluorite structure which

is reported propitious for Li insertion. In spite of a large initial specific capacity (1370 mAh/g at an average 350 mV vs Li^+/Li), the mechanical instability of the electrode causes a drastic capacity fade, even at reduced voltage windows. The reaction mechanism is cause for debate. Moriga *et al.* proposed that lithium inserts into the vacant sites, leading to the formation of a ternary phase LiMg_2Si , then Li_2MgSi , along with extrusion of Mg that reacts to form Li/Mg alloys.⁸⁵ On the other hand, a simple dissociation reaction followed by the formation of lithium alloys with Mg and Si is proposed by other groups.^{86,87} Studies on Mg_2Sn ⁸⁸ and Mg_2Ge ,⁸⁹ show better cycling performance (for the tin compound) than the isostructural Mg_2Si and capacities of 300 mAh/g after 60 cycles.

Nitrides

The quest for alternative anode materials for Li-ion batteries has led the scientific community to the investigation of transition metal nitrides. These compounds show a lower intercalation potential compared to the respective oxides due to the lower formal oxidation state of the metal, and strong covalent character of the metal-pnictogen bond, which leads to high-lying mixed anion-metal bands, and a high degree of electron delocalization.^{90,91}

The mechanisms associated with the lithium uptake and extraction in transition metal nitrides have been investigated to some extent.⁹² Low lithium content nitrides usually crystallize as a solid solution with a Li_3N -type layered structure. Lithium

extraction from these materials induces the formation of an amorphous phase LiM_xN ($\text{M}=\text{Co}, \text{Fe}, \text{Ni}$ and Cu).^{93,94} The theoretical capacity of the material is thus inversely proportional to the content of transition metal atoms, but a low degree of substitution diminishes reversibility. Shodai *et al* attributed this dependence to the stabilization of the formed amorphous phase by the strong M–N covalent bond and co-participation of nitrogen in the redox process.

Highly lithiated transition metal nitrides tend to crystallize with cubic symmetry – for example, Li_7VN_4 has an antiferite-type structure and in Li_7MnN_4 the MnN_4 tetrahedra occupy the corner, face, and centre positions and lithium atoms are distributed on the remaining tetrahedral sites.^{95,96} Nishijima and co-workers reversibly removed up to 1.25 Li^+ from Li_7MnN_4 through a two-phase reaction that leads to the formation of a cubic structure of smaller lattice parameter.⁹² Nevertheless, they identified neither the new formed phase nor the phase transformation mechanism. Later, Susuki and Shodai studied the charge balance mechanism between Li_7MnN_4 and Li_6MnN_4 .⁹⁷ The authors showed that the lowest unoccupied orbitals of Li_7MnN_4 have a strong nitrogen $2p$ character and that removal of lithium from the structure introduces holes in these orbitals rather than into the manganese $3d$ ones. These results indicate once again that, in contrast to transition metal oxides, the anionic network plays an important role in the redox process of nitrides.

Regardless of the mechanism involved in lithium removal and uptake by the

nitrides, the electrochemical properties of the materials are not very encouraging. Vanadium and manganese nitrides exhibit initial specific capacities, 170 and 166 mAh/g, respectively, which are not competitive values relative to carbon electrodes (352 mAh/g). In addition, the lithiated transition metal nitrides are extremely reactive phases; the assembly of batteries using such material is not very practical and the anode acts as a source and not a sink of lithium.

Phosphides

Phosphides exhibit a combination of the other Group V members' chemical behaviour. As in nitrides and antimonides, the metal has a low formal oxidation state due to high-lying mixed anion-metal bands, a high degree of electron delocalization, and strong covalent character of the M-pnictogen bond, leading to lower intercalation potentials than the respective oxides.⁹⁰ Moreover, phosphides display more covalent bonding than the corresponding nitrides, but less than the predominantly semi-metallic antimonides. These bonding differences are reflected in the band structure (Figure 2.6) and chemistry of the materials.

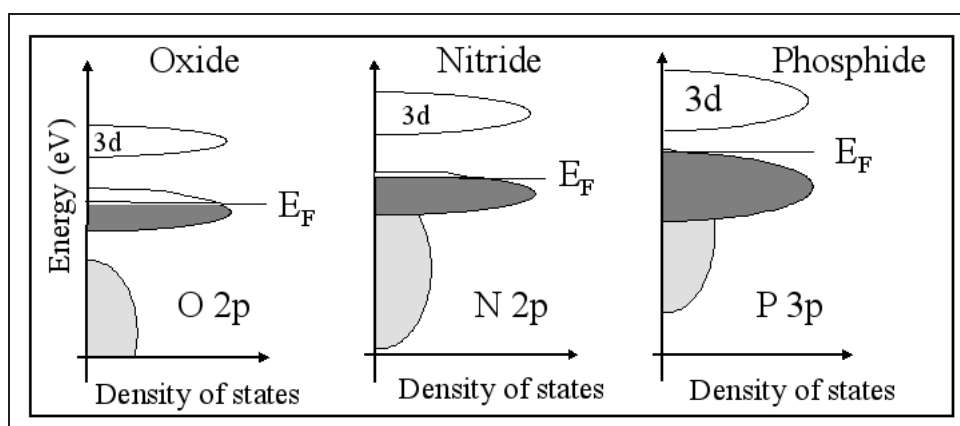


Figure 2.6: Schematic representation of the DOS for oxides, nitrides, and phosphides.

In nitrides, the upper band is densely populated with nitrogen orbitals such that oxidation generates holes in the nitrogen orbitals with consequent evolution of N_2 on overcharge.⁹⁸ In antimonides, the redox reactions involve the metal-Sb bond, and hence Li uptake/extraction results in phase separation to form metal and Li_xSb alloys. In phosphides, the chemistry seems to lie midway between the two. The differences in strength of the M-pnictogen (P_N) bond, and relative contribution of the P_N-P_N bond explain the small amount of transition metal-poor binary nitrides known (and abundance of antimonides). For example, MnN_4 , analogous to MnP_4 , does not exist. As no binary nitrides are known to uptake Li^+/e^- , the lithium ions must first be removed from the structure to give reversible cycling. This constitutes a deficiency of these materials since the negative electrode in a cell should act as a reservoir, not a source, of Li. In this respect, phosphides have advantages over nitrides. Additionally, the delithiation process of ternary nitrides results in irreversible collapse into an

amorphous structure.

At the beginning of this research project, no metal phosphide had been evaluated as anode material for Li-ion batteries; our report in *Science Magazine* was the first of its kind.⁹⁹ Since then, our research group and others have investigated different transition metal phosphides. The following list depicts their main electrochemical properties:

VP:¹⁰⁰ First discharge exhibits a plateau at 0.05 V but subsequent cycling shows typical solid solution behaviour with a reversible capacity on 2 cycles equivalent to 230 mAh/g. X-ray diffraction data indicates that topotactic reaction (true insertion) takes place.

VP₄:¹⁰¹ First discharge produces 1460 mAh/g in a four step reaction; three steps between 1.0 and 0.5 V and one close to 0 V. The reported reversible specific capacity in the voltage window of 0.77–2.5 V is 430 mAh/g for 100 cycles. Based on *ex-situ* analysis of cycled material the authors suggest a reaction mechanism as follows:

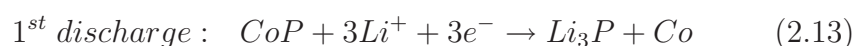
1. Before 0.77 V: topotactic insertion of 3 Li in monoclinic VP₄;
2. Between 0.77 and 0.65 V: non-topotactic uptake of 3 Li (phase transformation: monoclinic ↔ cubic);
3. Between 0.65 and 0.50 V: uptake of 3 Li accompanied by structure decomposition with formation of Li₃P and VP;

4. Below 0.50 V: lithium insertion into VP lattice.

MnP₄ and Li₇MnP₄:^{102,103} Gillot and co-workers reported the uptake of up to 7Li by MnP₄ between 1.7 and 0.5 V of these, only 4.5 were extracted on oxidation. Increasing the voltage window to 1.7 and 0.01 V led to the uptake of 3 additional Li⁺ corresponding to an alleged incomplete decomposition reaction of Li₇MnP₄ into Li₃P and Mn⁰. Starting the electrochemical redox process with the lithiated ternary phase gave similar initial capacity results, but very poor cycling performance. Molecular electronic structure calculations based on the extended Hückel tight-binding method (EHTB) showed that the redox center involved in the MnP₄ + 7Li reaction is primarily the phosphorus atoms. Through first-principles electronic structure calculations, the authors also suggested that the charge process occur *via* a two-phase reaction between Li₇MnP₄ and Li₅MnP₄.

Li_{5.5}Mn_{2.5}P₄:^{102,103} The system exhibits a specific capacity of up to 900 mAh/g after the first charge process and only 10% capacity fading after 25 cycles. The electrochemical Li uptake/removal processes occur through smooth evolution of the lattice parameters while preserving the crystalline nature of the material. By comparison with the Li₇MnP₄, the authors claim that the crystal structure, and moreover, the stoichiometry of heavy metal atoms, plays a key role in the electrodes cycling performances.

CoP and CoP₃:^{104,105} Alcántara *et. al.* showed that lithium reacts electrochemically with CoP₃ through a single extended quasi-plateau at about 0.4–0.25 V during the first discharge. The authors concluded that the process involves reduction of cobalt to Co⁰, formation of hexagonal Li₃P, and amorphization of the material. Additionally, they suggested that part of the lithium can be reversibly extracted upon charging, yielding a reversible capacity of 487 mAh/g on second discharge. On the other hand, Zhang and co-workers showed that samples prepared by high-energy ball-milling consisted of mixtures of CoP₃ and CoP, their relative amounts depending on the duration of milling. The initial electrochemical lithiation of CoP and CoP_x (CoP₃+CoP) yielded reversible capacities of 533 and 878 mAh/g, respectively. The authors noted a higher efficiency for CoP (74%) in the first cycle than the expected theoretical value (66.7%), calculated in the basis of a inactive Co formation mechanism similar to that proposed for CoP₃:¹⁰⁵

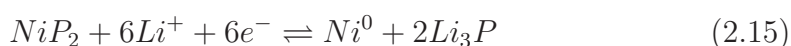


The authors suggested that the reduced metallic Co takes part, at least partially, in the oxidation reaction and that, for milled samples, a multi-step insertion process occurs, associated with a LiP intermediate phase. Furthermore, partial mechanical lithiation of the samples with Li₃N (reduction of CoP₃ to CoP) suppressed the initial irreversibility to only 5% at the expense of capacity.

NiP₂:¹⁰⁶ Cubic and monoclinic NiP₂ polymorphs react reversibly with 4.2 and 5.0 Li per unit formula, respectively. The phases exhibited different reaction paths during the first discharge: the cubic phase undergoes direct decomposition into metallic nickel and Li₃P, whereas Li₂NiP₂ forms as an intermediate insertion phase upon reduction of monoclinic NiP₂. The authors attributed the different behaviours to a combination of two factors:

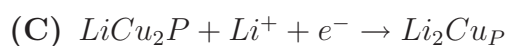
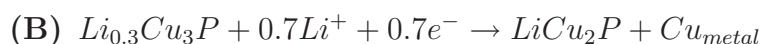
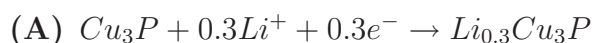
1. Different oxidation states and local environments for Ni in the two polymorphs, and
2. Close packed nature of cubic phase, which favours the direct conversion reaction, as opposed to the presence of interlayer space in monoclinic NiP₂, which in turn can accommodate lithium ions, allowing for an insertion reaction prior to conversion.

Whatever the starting phase, however, the final reduced material had similar composition, namely Li₃P and Ni nanoparticles. On subsequent cycling both polymorphs react with Li according to a direct conversion process represented in Equation 2.15. Self supported electrodes, made by vapour-phase transport of the monoclinic phase on commercial Ni-foam, displayed good cycling performance (95%) and enhanced rate capability.



Cu₃P:^{107–111} In 2004 Crosnier and Nazar reported on the two-step electrochemical

reaction of Cu_3P with 3Li. The authors identified a two-phase process in which copper is extruded from the Cu_3P lattice and a metastable intermediate phase “ $\text{Li}_x\text{Cu}_{3-x}\text{P}$ ” is formed, followed by decomposition into Cu^0 and Li_3P upon further lithiation. The hexagonal close-packed (hcp) arrangement of phosphorus atoms in lithiated and non-lithiated phases made such a process possible. Studies carried out by other research groups showed that the electrochemical properties of Cu_3P , specially the initial capacity and capacity retention, depend strongly on the powder morphologies, suggesting a slightly more complex mechanism for lithium uptake by nanoscopic crystalline Cu_3P .^{108–111}



(D) *Reversible reaction of electrolyte with lithium*



Self-supported films of Cu_3P on copper foil also uptake lithium, however, through a different non-elucidated mechanism.

Li_2CuP :¹¹² This phosphide showed a rather surprising reversible crystalline-amorphous transformation upon lithium extraction/uptake. In this system, the Cu–P framework structure reformed at the end of the reduction remains during the second oxidation. Oxidation and reduction involves the cleavage

and reformation of Li–P bonds. Band structure calculations showed that the majority of the (filled) Cu *d*-bands are narrow and lie well below the Fermi level, indicating that these *d*-orbitals do not participate in the redox process. Alternatively, the uppermost band that lies just below the Fermi level includes both Cu and P bonding states. Along with cleavage of the Li–P bonds, extraction of electron density from this band affects the Cu–P bonding in the hexagonal framework; the authors suggested this as responsible for the observed increase in structural disorder on oxidation. Thus, a significant role in the electrochemical process is adopted by the phosphorus anions.

Zn₃P₂:¹¹³ Zinc phosphide powders of varied morphology and particle size were synthesized by three different routes: ball-milling, ball-milling followed by annealing, and ceramic processing at high temperature. The electrochemical reaction of Zn₃P₂ with lithium led to a high initial capacity (995 mAh/g). Bichat *et. al.* suggested an insertion mechanism that involves two distinct but parallel reversible pathways (Figure 2.7): one implies exclusively phosphide phases (Zn₃P₂, LiZnP, Li₄ZnP₂, and Li₃P) and the second involves only Li-Zn alloys (Zn, LiZn₄, and LiZn). The various phases involved in the overall reaction are structurally close allowing a high reversibility of the process, although some of the observed transitions impoverishes the electrochemical performances of these materials, especially capacity retention.

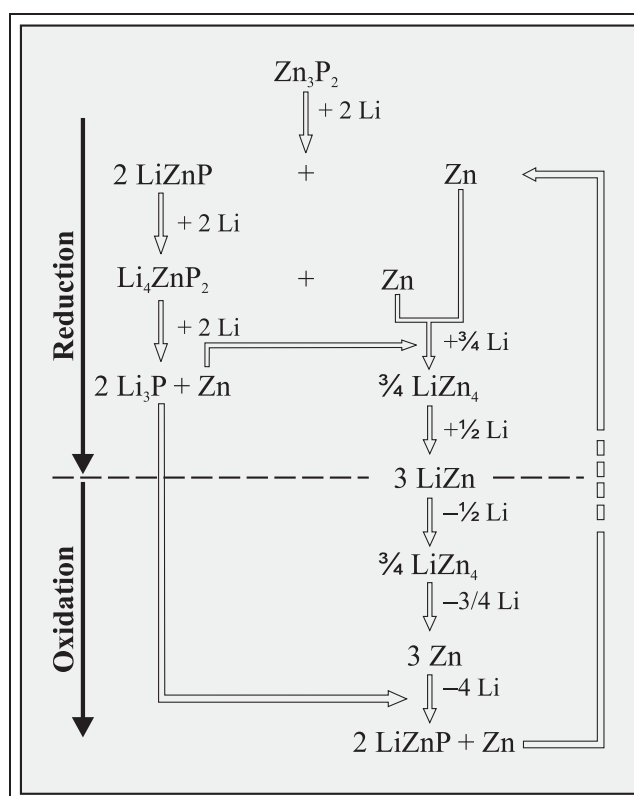
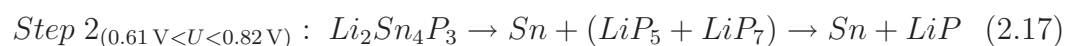
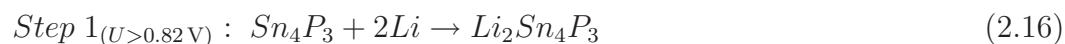


Figure 2.7: Proposed mechanism for reversible reaction of Li with Zn_3P_2 .¹¹³

Sn_4P_3 :¹¹⁴ Kim and co-workers evaluated the electrochemical and local structural characteristics of nanosized layered Sn_4P_3 during charge/discharge in lithium batteries. The phosphide showed a good cycleability and sustained 370 mAh/g for up to 50 cycles when cycled within a limited voltage window (0–0.72 V). With increasing lithium uptake, the tin phosphide was converted into lithium phosphides followed by formation of a lithium-tin alloy, indicating that both tin and phosphorus act as active redox centers. Capacity fading at the voltage region above 0.9 V was attributed to the irreversible formation of LiP and the

agglomeration of tin atoms. The following three-step reaction mechanism was suggested to explain the electrochemical process:*



Li₉TiP₄:¹¹⁵ Electrochemical extraction/insertion of lithium by Li₉TiP₄ yields a specific capacity of 830 mAh/g at an average potential close to 1V. The reversible structural phase transition observed upon cycling was correlated to a loss/reconstruction of the unit cell cubic-*fcc* symmetry. The authors proposed a reaction mechanism in terms of Ti–P bond contraction/elongation in the tetrahedral TiP₄^{-x} electronic entities. The two phases involved in the oxidation process correspond to nearly size-equivalent cubic structures in which P atoms are ordered (Li-rich) and disordered (Li-poor), hence favouring a redox-induced mechanism without significant electrode volume change. Nevertheless, the different kinetic barriers associated with Li⁺ extraction from P–ordered, and insertion into P–disordered phases, induce different mechanisms upon charge and discharge. The authors pointed out that the *fcc* pnictogen (P_N) networks exhibit most of the crystallographic and electronic features required for competitive electrode materials: a large number of cationic vacancies, a large unit cell volume, and large band of nearly P_N–P_N non-bonding levels.

* Non-balanced equations extracted from original reference.

Provided that this band is involved in electrochemical redox processes, a host material structural change should therefore be prevented.

Li_xVP₄:¹¹⁶ The ternary phases Li_xVP₄ show a high specific capacity in their first charge/discharge cycle, associated with a large variation of lithium content per formula unit ($3 \leq x \leq 7.5$). XRD analysis and first-principle electronic structure calculations evidence the stability of the Li_xVP₄ crystal structure for various lithium compositions. Likewise, in the Li₉TiP₄ system, the host matrix behaves as a structurally stable network of weakly interacting tetrahedra, able to store (or release) a large number of additional electrons (concomitant with the intercalation or deintercalation of lithium) into a nearly non-bonding Pn-Pn band. This leads to very small volume variations of the unit cells (< 1%) upon cycling.

References

- [1] Huggins, R. Mat. Res. Soc. Symp. Proc.. In *Solid States Ionics IV*, Vol. 369; MRS: Boston, 1995; Chapter Pulse Applications of Electrochemical Cells Containing Insertion Reacton Electrodes, page 3.
- [2] Armand, M. Materials for Advanced Batteries. In ; Plenum: New York, 1980; Chapter Intercalation Electrodes, page 145.
- [3] Ceder, G.; Aydinol, M. K.; Kohan, A. F. *Comput. Mater. Sci.* **1997**, 8, 161.
- [4] Aydinol, M. K.; Ceder, G. *J. Electrochem. Soc.* **1997**, 144, 3832.
- [5] Ceder, G.; der Ven, A. V. *Electrochim. Acta* **1999**, 44, 254.
- [6] Aydinol, M. K.; Kohan, A. F.; Ceder, G.; Cho, K.; Joannopoulos, J. *Phys. Rev. B: Condens. Matter* **1997**, 56, 1354.
- [7] Gerischer, H.; Decker, F.; Scrossati, B. *J. Electrochem. Soc.* **1994**, 141, 2297.
- [8] Alberty, R.; Silbey, R. *Physical Chemistry*; John Wiley: New York, 1996.

- [9] Tirado, J. L. *Mater. Sci. Eng. R: Reports* **2003**, *40*, 103-136.
- [10] Nazri, G.-A.; Pistoia, G., Eds.; *Lithium Batteries: Science and Technology*; Springer: New York, 2004.
- [11] Thackeray, M. M. The Structural Stability of Transition Metal Oxide Insertion Electrodes for Lithium Batteries. In *Handbook of Battery Materials*; Besenhard, J., Ed.; Wiley-VCH: Weinheim, 2000.
- [12] Winter, M.; Besenhard, J. O.; Spahr, M.; Novak, P. *Adv. Mater.* **1998**, *10*, 725.
- [13] Arai, H.; Okada, S.; Ohtsuk, H.; Ichimura, M.; Yamaki, J. *Solid State Ionics* **1995**, *80*, 261.
- [14] Ohzuku, T.; Ueda, A.; Nagayama, M. *J. Electrochem. Soc.* **1993**, *140*, 1862.
- [15] T. Ohzuku, T. Yanagawa, M. K.; Ueda, A. *J. Power Sources* **1997**, *68*, 131.
- [16] Gummow, R.; Thackeray, M. *J. Electrochem. Soc.* **1993**, *140*, 3365.
- [17] Dahn, J.; von Sacken, U.; Juzkow, M.; Al-Janaby, H. *J. Electrochem. Soc.* **1994**, 2207.
- [18] Garcia, B.; Farcy, J.; Pereira-Ramos, J.; Perichon, J.; Baffier, N. *J. Power Sources* **1995**, *54*, 373.
- [19] Li, W.; Reimers, J.; Dahn, J. *Solid State Ionics* **1994**, *67*, 123.

- [20] Sawai, K.; Ueda, A.; Nagayama, M.; Iwakoshi, Y.; Ohzuku, T. *Denki Kagaku* **1993**, *61*, 715.
- [21] Moshtev, R.; ; Zlatilova, P.; Manev, V.; Sato, A. *J. Power Sources* **1995**, *54*, 109.
- [22] Broussely, M.; Pertont, F.; Biesan, P.; Bodet, J.; Labat, J.; Lecerf, A.; Delmas, C.; Rougier, A.; Peres, J. *J. Power Sources* **1995**, *54*, 109.
- [23] Ohzuku, T.; Kitagawa, M.; Hirai, T. *J. Electrochem. Soc.* **1989**, *136*, 3169.
- [24] Ohzuku, T.; Kitagawa, M.; Hirai, T. *J. Electrochem. Soc.* **1990**, *137*, 40.
- [25] Nohman, T.; Saito, T.; Furukawa, N.; Ikeda, H. *J. Power Sources* **1989**, *26*, 389.
- [26] Nohman, T.; Yamamoto, Y.; Nishio, K.; Nakane, I.; Furukawa, N. *J. Power Sources* **1990**, *32*, 373.
- [27] Nohman, T.; Yamamoto, Y.; Nakane, I.; Furukawa, N. *J. Power Sources* **1992**, *39*, 51.
- [28] Thackeray, M. M.; David, W.; Bruce, P.; Goodenough, J. *Mater. Res. Bull.* **1983**, *18*, 461.
- [29] Thackeray, M. M.; Johnson, P.; "de Picciotto", L.; Bruce, P.; Goodenough, J. *J. Solid State Chem.* **1984**, *55*, 280.

- [30] Goodenough, J.; Thackeray, M. M.; David, W.; Bruce, P. *Rev. Chem. Miner.* **1984**, *21*, 435.
- [31] Yamada, A.; Tanaka, M. *Mater. Res. Bull.* **1995**, *30*, 278.
- [32] Kerr, T. *Synthesis, Characterization, and Electrochemical Investigation of Novel Electrode Materials for Lithium Ion Batteries*, Ph.D. thesis, University of Waterloo, 2002.
- [33] Yin, S. *Understanding Structure-Property Relationships in Lithium Metal Phosphates and Oxide Electrode Materials: X-ray/Neutron Diffraction and ^7Li MAS-NMR Coupled with Li-Ion Electrochemistry*, Ph.D. thesis, University of Waterloo, 2005.
- [34] Chiang, C.; ad A.J. Heeger, Y. P.; Shirakawa, H.; Louis, E.; MacDiarmid, A. *J. Chem. Phys.* **1978**, *69*, 5098.
- [35] MacDiarmid, A.; Maxfield, M. Organic polymers as electroactive materials. In *Electrochemical Science and Technology of Polymers*, Vol. 67; Elsevier: London, 1987.
- [36] Aurbach, D. *Nonaqueous Electrochemistry*; Marcel Dekker, Inc.: New York, 1999.
- [37] Besenhard, J.; Winter, M.; Yang, J.; Biberacher, W. *J. Power Sources* **1995**, *54*, 228.

- [38] Yazami, R.; Genies, S. *Denki Kagaku* **1998**, *66*, 1293.
- [39] Chung, G.; Kim, H.; Yu, S.; Jun, S.; Choi, J.; Kim, M. *J. Electrochem. Soc.* **2000**, *147*, 4391.
- [40] Ein-Eli, Y. *J. Electroanal. Chem.* **2002**, *531*, 95.
- [41] Linden, D.; Reddy, T. *Handbook of Batteries*; McGraw Hill: New York, 3rd. ed.; 2002 Chapter 2.
- [42] Krause, L.; Lamanna, W.; Summerfield, J.; Engle, M.; Korba, G.; Loch, R. *J. Power Sources* **1997**, *68*, 320.
- [43] Nagayama, K.; Kamioka, K.; Iwata, E.; Oka, H.; Tokunaga, Y.; Okada, T. *Electrochemistry* **2001**, *69*, 6.
- [44] Smagin, A.; Matyuka, V.; Korobtsev, V. *J. Power Sources* **1997**, *68*, 326.
- [45] Zhang, X.; Ross, P.; KostECKI, R.; Kong, F.; Sloop, S.; Kerr, J.; Streibel, K.; Cairns, E.; McLarnon, F. *J. Electrochem. Soc.* **2001**, *148*, A463.
- [46] DuPasquier, A.; Blyr, A.; Courjal, P.; Larcher, D.; Amatucci, G.; Gand, B.; Tarascon, J.-M. *J. Electrochem. Soc.* **1999**, *146*, 428.
- [47] Armstrong, D.; Perkins, P. *Electrochim. Acta* **1974**, *10*, 77.
- [48] Naoi, K.; Mori, M.; Narupka, Y.; Lamanna, W.; Atanasoski, R. *J. Electrochem. Soc.* **1999**, *146*, 462.

- [49] Dahn, J.; Sleigh, A.; Shi, H.; Way, B.; Weydanz, W.; Reimers, J.; Zhong, Q.; von Sacken, U. Carbons and Graphites as Substitutes for the Lithium Anode. In *Lithium Batteries - New Materials, Developments and Perspectives*; Pistoia, G., Ed.; Elsevier: Amsterdam, 1994.
- [50] Billaud, D.; Henry, F.; Willmann, P. *J. Power Sources* **1995**, *54*, 383.
- [51] Shi, H.; Barker, J.; Koksang, R. *J. Electrochem. Soc.* **1996**, *143*, 3466.
- [52] Hérold, A. *Bull. Soc. Chim.* **1955**, *187*, 999.
- [53] Daumas, N.; Hérold, A. *Bull. Soc. Chim.* **1971**, *5*, 1598.
- [54] Dahn, J. *Phys. Rev. B: Condens. Matter* **1991**, *44*, 9170.
- [55] McKinnon, W. Insertion electrodes I: Atomic and electronic structure of the hosts and their insertion compounds. In *Solid State Electrochemistry*; Cambridge University Press: Cambridge, 1995.
- [56] Peled, E. *J. Electrochem. Soc.* **1979**, *126*, 2047.
- [57] Aurbach, D.; Markovsky, B.; Schechter, A.; Ein-Eli, Y. *J. Electrochem. Soc.* **1996**, *143*, 3809.
- [58] Ohzuku, T.; Ueda, A.; Yamamoto, N. *J. Electrochem. Soc.* **1995**, *142*, 1431.
- [59] Ohzuku, T.; Tatsumi, K.; Matoba, N.; Sawai, K. *J. Electrochem. Soc.* **2000**, *147*, 3592.

- [60] Owen, J. *Colloids Surf. Rev.* **1997**, *26*, 259.
- [61] Yang, J.; Winter, M.; Besenhard, J. O. *Solid State Ionics* **1996**, *90*, 281.
- [62] Idota, Y.; Kubota, T.; Matsufuji, A.; Maekawa, Y.; Miyasaki, T. *Science* **1997**, *276*, 1395.
- [63] Taylor, B.; Kauslaurich, S.; Delgado, G.; Lee, H. *Chem. Mat.* **1999**, *11*,.
- [64] Mayeri, D.; Phillips, B.; Augustine, M.; Kauzlarich, S. *Chem. Mat.* **2001**, *13*, 765.
- [65] Anani, A.; Crouch-Baker, S.; Huggins, R. *J. Electrochem. Soc.* **1988**, *135*, 2103.
- [66] Besenhard, J.; Komenda, P.; Paxinos, A.; Wudy, E.; Josowicz, M. *Solid State Ionics* **1986**, *18-19*, 823.
- [67] Mao, O.; Turner, R. L.; Courtney, I. A.; Fredericksen, B. D.; Buckett, M. I.; Krause, L. J.; Dahn, J. R. *Electrochem. Solid State Lett.* **1999**, *2*, 3.
- [68] Kepler, K. D.; Vaughey, J. T.; Thackeray, M. M. *J. Power Sources* **1999**, *82*, 383-387.
- [69] Li, H.; Huang, X.; Chen, L.; Wu, Z.; Liang, Y. *Electrochem. Solid State Lett.* **1999**, *2*, 547.

- [70] Kepler, K. D.; Vaughey, J. T.; Thackeray, M. M. *Electrochem. Solid State Lett.* **1999**, *2*, 307.
- [71] Thackeray, M. M.; David, W.; Goodenough, J. *J. Solid State Chem.* **1984**, *55*, 280.
- [72] Picciotto, L.; Thackeray, M. M. *Mater. Res. Bull.* **1986**, *21*, 583.
- [73] Poizot, P.; Laruelle, S.; Grugeon, S.; Dupont, L.; Tarascon, J.-M. *Nature* **2000**, *407*, 496.
- [74] Iodata, Y.; Kubota, T.; Matsufuji, A.; Maekawa, Y.; Miyasaka, T. *Science* **1997**, *276*, 1395.
- [75] Courtney, I. A.; Dahn, J. R. *J. Electrochem. Soc.* **1997**, *144*, 2045.
- [76] Courtney, I. A.; Dahn, J. R. *J. Electrochem. Soc.* **1997**, *144*, 2943.
- [77] Goward, G.; Leroux, F.; Power, W.; Egami, T.; Dmowski, W.; Nazar, L. F. *Electrochem. Solid State Lett.* **1999**, *2*, 367.
- [78] Goward, G.; Nazar, L. F.; Power, W. *J. Mater. Chem.* **2000**, *10*, 1.
- [79] Yang, J.; Raistrick, I.; Huggins, R. *J. Electrochem. Soc.* **1986**, *133*, 457.
- [80] Alcántara, R.; Fernandez-Madrigal, F.; P. Lavela, J. T.; Jumas, J.-C.; Olivier-Fourcade, J. *J. Chem. Mat.* **1999**, *9*, 2517.

- [81] Fernandez-Madrigal, F. J.; Lavela, P.; Vicente, C. P.; Tirado, J. L. *J. Electroanal. Chem.* **2001**, *501*, 205.
- [82] Crosnier, O.; Souza, D. C. S.; Greedan, J. E.; Nazar, L. F. Reversible Lithium Uptake by FeP₂. In *Material Research Society Symposium*; MRS: Boston, 2002.
- [83] Fransson, L. M. L.; Vaughey, J. T.; Edström, K.; Thackeray, M. M. *J. Electrochem. Soc.* **2003**, *150*, A86.
- [84] Fransson, L. M. L.; Vaughey, J. T.; Benedek, R.; Edström, K.; Thomas, J. O.; Thackeray, M. M. *Electrochem. Comm.* **2001**, *3*, 317.
- [85] Moriga, T.; Watanabe, K.; Tsuji, D.; Massaki, S.; Nakabayashi, I. *J. Solid State Chem.* **2000**, *153*, 386.
- [86] Santos-Pena, J.; Brousse, T.; Schleich, D. *Ionics* **2000**, *6*, 133.
- [87] Kim, H.; Cho, J.; Sohn, H.-J.; Kang, T. *J. Electrochem. Soc.* **2000**, *146*, 4401.
- [88] Sakaguchi, H.; Maeta, H.; Kubota, M.; Honda, H.; Esaka, T. *Electrochemistry* **2000**, *68*, 632-635.
- [89] Kim, Y. I.; Yoon, C. S.; Park, J. W. *J. Solid State Chem.* **2001**, *160*, 388-393.
- [90] Lefebvre-Devos, M. L.; Wallart, J. Olivier-Fourcade, L. M.; Jumas, J.-C. *Phys. Rev. B: Condens. Matter* **2001**, *63*, 125110.

- [91] Nazar, L. F.; Crosnier, O. Anode and composite anodes: an overview. In *Lithium Batteries: Science and Technology*; Springer: New York, 2004.
- [92] Nishijima, M.; Tadokoro, N.; Takeda, Y.; Nobuyuki, I.; Yamamoto, O. *J. Electrochem. Soc.* **1994**, *141*, 2966-2971.
- [93] Pralong, V.; Rowsell, J. L. C.; Nazar, L. F. *J. Am. Chem. Soc.* **2001**, *123*, 8598-8599.
- [94] Shodai, T.; Okada, S.; Tobishima, S.; Yamaki, J. *Solid State Ionics* **1995**, *86-85*, 785.
- [95] Gudat, A.; Haag, S.; Kniep, R.; Rebenau, A. *Z. Naturf.* **1990**, *456*, 111.
- [96] Juza, R.; Anschutz, E.; Puff, H. *Angew. Chem.* **1959**, *71*, 161.
- [97] Suzuki, S.; Shodai, T. *Solid State Ionics* **1999**, *116*, 1-9.
- [98] Shodai, T.; Sakurai, Y.; Suzuki, T. *Solid State Ionics* **1999**, *122*, 85.
- [99] Souza, D.; Pralong, V.; Jacobson, A.; Nazar, L. *Science* **2002**, *296*, 2012.
- [100] Kim, Y.-U.; Sohn, H. "Novel vanadium monophosphide (VP) insertion anode material for lithium secondary batteries". In *Proceedings of the 207 ECS Meeting*; Electrochemical Society: QC-Canada, 2005.
- [101] Kim, Y.-U.; Cho, B. W.; Sohn, H. *J. Electrochem. Soc.* **2005**, *152*, A1475.

- [102] Gillot, F.; Monconduit, L.; Morcrette, M.; Doublet, M.-L.; Dupont, L.; Tarrascon, J.-M. *Chem. Mat.* **2005**, *17*, 3627.
- [103] Gillot, F.; Monconduit, L.; Doublet, M.-L. *Chem. Mat.* **2005**, *17*, 5817.
- [104] Zhang, Z.; Yang, J.; Nuli, Y.; Wang, B.; Xu, J. *Solid State Ionics* **2005**, *176*, 693.
- [105] Alcántara, R.; Tirado, J.; Jumas, J.; Monconduit, L.; Ollier-Fourcade, J. *J. Power Sources* **2002**, *109*, 308.
- [106] Gillot, F.; Boyanov, S.; Dupont, L.; Doublet, M.-L.; Morcrette, M.; Monconduit, L.; Tarrascon, J.-M. *Chem. Mat.* **2005**, *17*, 6327.
- [107] Crosnier, O.; Nazar, L. F. *Electrochem. Solid State Lett.* **2004**, *7*, A187.
- [108] Bichatt, M.-P.; Politova, T.; Pfeiffer, H.; Tancret, F.; Monconduit, L.; Pascal, J.; Brousse, T.; Favier, F. *J. Power Sources* **2004**, *136*, 80.
- [109] Bichatt, M.-P.; Politova, T.; Pascal, J.; Favier, F.; Monconduit, L. *J. Electrochem. Soc.* **2004**, *151*, A2074.
- [110] Pfeiffer, H.; Tancret, F.; Brousse, T. *Electrochim. Acta* **2004**, *50*, 4763.
- [111] Pfeiffer, H.; Tancret, F.; Bichatt, M.-P.; Monconduit, L.; Favier, F.; Brousse, T. *Electrochem. Comm.* **2004**, *6*, 263.

- [112] Crosnier, O.; Mounsey, C.; Herle, P. S.; Taylor, N.; Nazar, L. F. *Chem. Mat.* **2003**, *15*, 4890.
- [113] Bichatt, M.-P.; Pascal, J.; Gillot, F.; Favier, F. *Chem. Mat.* **2005**, *17*, 6761.
- [114] Kim, Y.-U.; Lee, C.; Sohn, H.; Kang, T. *J. Electrochem. Soc.* **2004**, *151*, A933.
- [115] Bichatt, M.-P.; Gillot, F.; Monconduit, L.; Favier, F.; Morcrette, M.; Lemoigno, F.; Doublet, M.-L. *Chem. Mat.* **2004**, *16*, 1002.
- [116] Doublet, M.-L.; Lemoigno, F.; Gillot, F.; Monconduit, L. *Chem. Mat.* **2002**, *14*, 4126.

Chapter 3

Techniques and Methodologies

3.1 Electrochemistry

The voltage-composition relation was determined using intermittent techniques in either current or potential controlled mode. These two techniques, usually referred to as “Galvanostatic Intermittent Titration Techniques” (GITT)¹ and “Potentiostatic Intermittent Titration Techniques” (PITT),² are described below.

3.1.1 GITT

In this method one applies a constant current to the system for a period of time, generating successive charge increments. The system is then allowed to relax at open circuit until it establishes equilibrium (no significant variation in voltage with

time). This technique allows the determination of equilibrium potential for a given reaction. Additionally, it gives information on the kinetics of the process (*e.g.* ohmic drop, chemical diffusion coefficient, partial ionic conductivity, etc.) with an accuracy that depends on the conditions of the experiment, particularly the duration of the current-on period and the geometry of the electrode.

3.1.2 PITT

In the case of PITT, small steps of voltage are imposed to the electrode while recording the current response over a period of time. The system is then relaxed at open circuit until its potential reaches equilibrium, which will be as close to the previously applied potential as the final current was negligible at the cut-off. Integration of the chronoamperometric response gives the charge increment ($\Delta Q = \int I(t)\delta t$), whereas its shape can give information on the kinetics of the process.

Thompson proposed an extension of the PITT protocol as a technique named Electrochemical Potential Spectroscopy (EPS).^{3,4} It consists of applying a series of small voltage steps to the electrochemical cell and allowing it to relax until the current decays to a limit value ($I_{limit} = C/300$), considered negligible compared to the capacity of the system, thus obtaining quasi-equilibrium incremental capacities at periodic potential intervals corresponding to the potential step amplitude. The plot of ΔQ vs. V in such an experiment is the incremental capacity voltamogram

of the reduction/oxidation, *i.e.* a spectrum of the redox states of the system, obtained with the resolution of the potential step amplitude. This technique permits the determination of the system phase diagram, with identification of single-phase domains and two-phase equilibrium, and of thermodynamic and kinetic properties.^{5,6} Following is a brief version of the detailed derivation presented in the literature.⁷

Monophasic Systems

Ionic diffusion controls the kinetics of a monophasic electrochemical reaction. For short times, the diffusion is approximately infinite and the system obeys Fick's law:

$$Flux = J = -D \frac{dc}{dx} \quad (3.1)$$

$$I = \frac{nFD^{1/2}c}{\pi^{1/2}t^{1/2}} \quad (3.2)$$

with D the diffusion coefficient, c the concentration of the diffusing species, x the path of diffusion, F Faraday's constant, and n the number of electrons involved in the overall reaction. Solution of Equation 3.1 leads to the Cottrell equation 3.2, which describes the chronoamperometric behaviour of single-phase processes in transient state. At equilibrium conditions, the over-potential $\eta = E - E^0$ is small and the current is given by the Tafel equation:

$$I = \frac{nFI_0}{RT}(E - E^0) \quad (3.3)$$

Biphasic Systems

Electrochemical reactions leading to the formation of immiscible phases display very different *I vs. t* transient behaviour, usually containing a rising portion, indicative of the presence of a nucleation step. Charge transport through the inter-phase surface *S* by carriers with mobility μ generates a current defined as:

$$I \propto \mu S(E - E^0) \quad (3.4)$$

where $(E - E^0)$, the driving force for the reaction, originates from:

1. For a phase transformation involving homogeneous nucleation of the new phase, the mobility of the charge carriers in the two phases controls the reaction and the current tends to have a constant value, proportional to the over-potential. Extrapolation of the potential to the limit of zero current (Figure 3.1(a)) gives the approximate value of the equilibrium potential for the reaction:
2. The mobility of the inter-phase A-B limits the reaction kinetics of reactions controlled by the heterogeneous nucleation of the phase B on surface A; the current response to an applied potential *V* (above the equilibrium) varies with time and the area of the inter-phase (Figure 3.1(b)). The nucleation process can be of two types, instantaneous and progressive, and overlap of the growth centers may occur leading to two expressions for the current density:

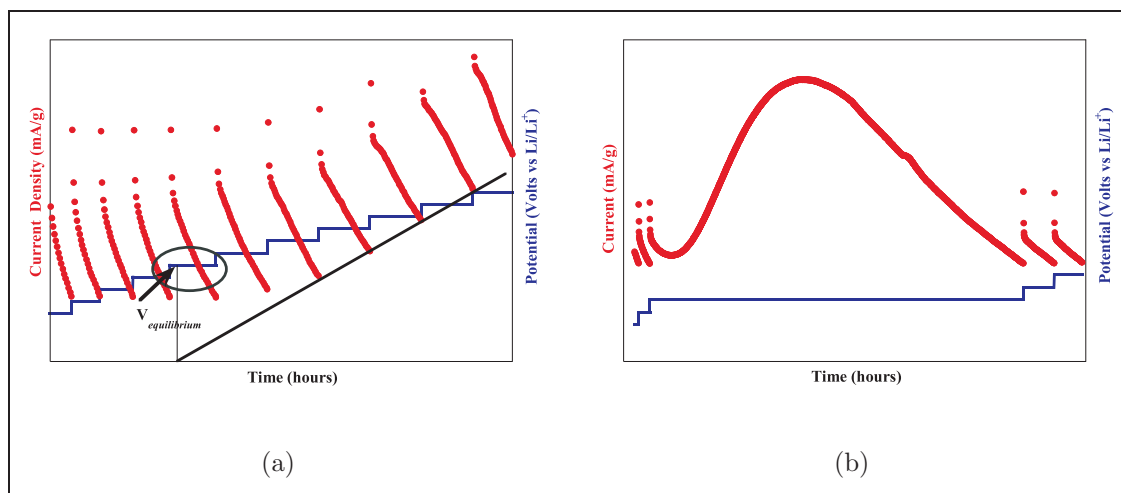


Figure 3.1: Typical chronoamperograms of (a) diffusion and (b) nucleation controlled biphasic electrochemical processes.

Instantaneous Nucleation:

$$I_{inst} = \frac{2\pi nFMhN_o k^2 t}{\rho} \exp\left(-\frac{\pi N_o M^2 k^2 t^2}{\rho^2}\right) \quad (3.5)$$

Progressive Nucleation:

$$I_{inst} = \frac{2\pi nFMhAN_o k^2 t^2}{\rho} \exp\left(-\frac{\pi AN_o M^2 k^2 t^3}{3\rho^2}\right) \quad (3.6)$$

3.1.3 Experimental

Electrochemical performance of the materials was evaluated using lithium metal as the counter-electrode in Swagelok[®] type cells (Figure 3.2). In a typical experiment, active materials were first sieved through a 625 mesh grid, then mixed with 20wt % carbon black (Chevron[®]50) for enhanced electronic conductivity and 5wt % of polymeric binder (poly-vinylidene fluoride, PVDF, Aldrich). A slurry of the mixture

in cyclopentanone was then cast on nickel disks and weighed after solvent evaporation. The cast material was dried for at least 4 hours at 120 °C and then transferred to an argon-filled glove-box where the cells were assembled using a fibreglass separator between the anode and the cathode. Except for the study of the influence of electrolyte composition on the electrochemical properties of FeP₂ system, presented in Chapter 5, a 1 M solution of LiPF₆ in a 1:1 mixture of EC/DMC (Selectipur[®], Merck) was employed as electrolyte. Electrochemical experiments were carried out in a MacPile[®]

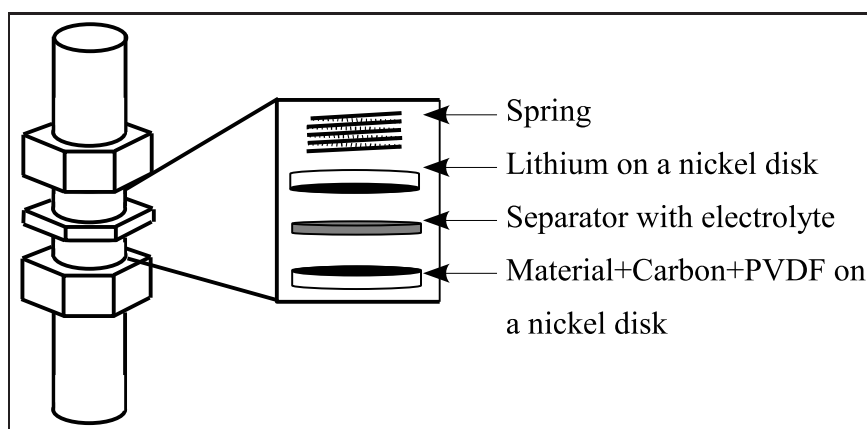


Figure 3.2: Schematic representation of a Swagelok type cell.

potentiostat controller (Biologic S.A., Claix, France). Galvanostatic experiments were carried out at different rates of intercalation (C/n , where C is the number of lithium intercalated per n hours) between preset voltage limits. GITT data was collected using current pulses of equivalent galvanic rate $C/30$ or $C/50$, followed of relaxation periods at OCV limited by voltage changes equal or less than 1 mV. Potentiostatic experiments were performed using voltage steps of 5 to 15 mV. Relaxation periods,

limited by the time to reach an equilibrium current equivalent to the galvanic rate of C/n for each cell (PCGA, Potentiostatic Control with Galvanic Acceleration) or a preset number of hours (whichever is less), were added to the protocols in PITT type experiments.

3.2 X-ray Diffraction

3.2.1 Fundamentals

In 1912 Friedrich, Knipping and von Laue performed the first diffraction experiment using single crystals of copper sulfate and zinc sulfite. Based on these experiments Max von Laue developed his theory of X-ray diffraction. At the same time W. L. Bragg and W. H. Bragg performed their diffraction experiments and in turn used an equivalent alternative and simpler way of explaining the observed diffraction phenomena – the Bragg's law of diffraction (illustrated in Figure 3.2.1). Two X-ray beams impinging upon a crystalline sample are reflected from various crystal planes at specific angles relative to the incident beams. The incident beams 1 and 2 are in phase and, in order to obtain constructive interference, so must be the reflected beams 1' and 2'. To satisfy this condition, beam 2' must travel an extra distance ABC relative to beam 1' and this distance must be equal to a whole number of wavelengths. The distance d (d -spacing) between the two planes of atoms and the

angle of incidence θ (Bragg angle) are related to the distances AB and BC by:

$$AB = BC = d \sin\theta \quad (3.7)$$

such that

$$ABC = 2d \sin\theta \quad (3.8)$$

and since $ABC = n\lambda$, the Bragg's law is derived as:

$$2d \sin\theta = n\lambda \quad (3.9)$$

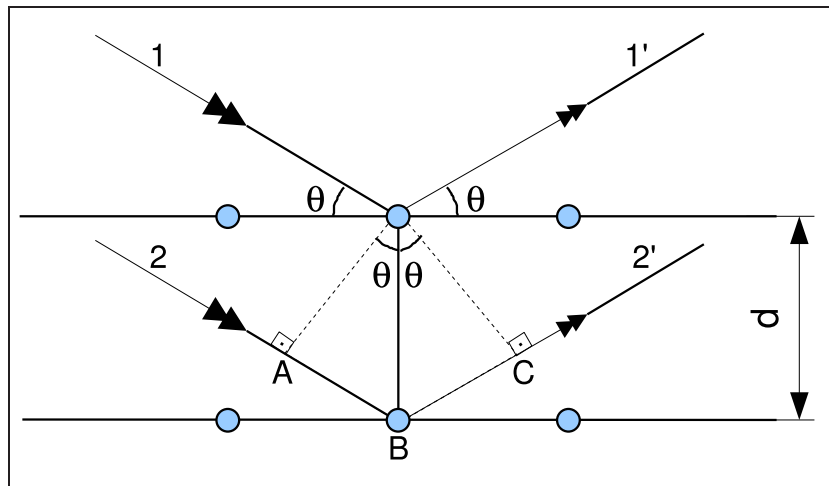


Figure 3.3: Schematic representation of Bragg's diffraction from two consecutive planes of atoms.

At angles of incidence different than the Bragg angle, the reflected beams are out of phase and interact destructively. Correlation of d with standard data such as from the JCPDS (Joint Committee on Powder Diffraction Standards) file, allows for

the identification of polycrystalline samples. The PDF method of analysis follows the procedure outlined by HRF (Hanawalt, Rinn, and Frevel⁸). Basically, the d values and intensities of the diffraction lines for the sample is compared with those of the standard files; positive identification of a phase demands agreement within experimental errors for both position and intensity of all lines. Since a powder sample can be regarded as a polycrystalline mass with crystallites spread in all possible orientations, powder XRD can also be used for structure determination. Despite the early development of the powder diffraction method in 1916, however, it was used for nearly half a century almost exclusively for qualitative and semi-quantitative phase analysis. This changed completely with the development of the Rietveld method, a technique for the refinement of crystal structures using the entire information of a powder diffraction pattern.

Position of the Bragg Reflection

The dimensions of the unit cell defines the positions of the Bragg-reflections. If the unit cell parameters are known, indexing of the diffraction pattern can be done by applying the general formula:

$$d_{hkl} = \sqrt{h^2 a^{*2} + k^2 b^{*2} + l^2 c^{*2} + 2hka^*b^* \cos\gamma^* + 2hla^*c^* \cos\beta^* + 2klb^*c^* \cos\alpha^*} \quad (3.10)$$

where a^* , b^* , c^* , α^* , β^* , and γ^* are the reciprocal lattice parameters.⁹

Intensity of the Bragg Reflection

The factors influencing the intensity of reflection lines are:

The atomic form factor (f_0): Phase differences arise due to the facts that atomic radii is of the order of X-ray wavelengths and the electrons are distributed over the entire atomic volume. A reduction of the intensity of the scattered wave with increasing scattering angle θ is observed. The numerical values for the atomic form factors for most atoms and ions are tabulated in the International Tables for Crystallography.¹⁰

The structure factor (F_{hkl}): It can be expressed as the Fourier sum over all atoms j in a unit cell with the phase ϕ of the reflection (Equation 3.11) and the intensity of a diffraction peak (Equation 3.12) is thus proportional to its squared value (multiplication of the structure factor by its conjugate complex). Because of the squaring, the differences in scattering power of the atoms are magnified. If heavy atoms are present in the crystal structure, the phases of diffraction peaks are mainly determined by these strong scatterers and the determination of the positions of light atoms is of limited precision.

$$F_{hkl} = \sum_{j=1}^N f_j \exp[2\pi i(hx_j + ky_j + lz_j)] = |F| \exp(i\phi) \quad (3.11)$$

$$I \approx |F_{hkl}|^2 = \left(\sum_{j=1}^N f_j \cos 2\pi(hx_j + ky_j + lz_j) \right)^2 + \left(\sum_{j=1}^N f_j \sin 2\pi(hx_j + ky_j + lz_j) \right)^2 \quad (3.12)$$

When the intensities are extracted from a diffraction pattern, several systematic errors must be taken into account and the intensities corrected accordingly:

- The electrons oscillate perpendicularly to the direction of the beam. Therefore, the component of the oscillation vector in the plane of incoming and diffracted beam decreases with increasing diffraction angle 2θ . The *polarization factor* corrects this effect.
- Diffraction arises when a reciprocal lattice node, which has a finite volume, crosses the Ewald sphere. The intensity is proportional to the time that the lattice node remains within the Ewald sphere. The so-called *Lorentz factor* takes this effect into account and corrects for it.
- Absorption of X-rays in a crystalline material decreases the intensity depending on the path-length through the sample. The intensity of the diffracted X-rays is thus reduced by the factor

$$I/I_0 = e^{-mx} \quad (3.13)$$

where x is the total path-length and m is the linear absorption coefficient of the material.

- Intensity changes can occur after the X-ray generator is turned on to full power. It is good practice to wait at least 12 hours before performing a measurement.
- *In flat plate powder diffraction geometry, the X-ray beam frequently spills over the sample at low diffraction angles, underestimating the peak intensities.
- *Because of the large number of crystallites in random orientation present in powder samples, the diffraction patterns are superimposed and form one or more arcs depending on the orientation of the crystallites.
- *The multiplicity M stands for the number of reflections of a face set $\{hkl\}$, which have identical d -spacings and therefore overlap systematically in a powder diffraction pattern. Depending on the crystal system, M can take values from 2 to 48; these values appear in the International Tables of Crystallography.¹⁰
- *Depending on the crystals' preferred cleavage the powder grains usually assume needle or plate-like shapes. On flat plate geometry measurements, the grains are distributed preferably on the cleavage orientations promoting an enhancement of the intensities of reflections with plane vectors similar to those of the preferred orientation.

* These factors specifically influence measurements of powder samples.

Shape of the Bragg Reflection

The profile of a powder diffraction peak consists of three parts: the background, the integrated intensity of the reflection, and the profile of the reflection. According to the theory of diffraction, the pattern of polycrystalline samples consists of sharp lines (Full Width at Half Maximum (FWHM) in the order of seconds of an arc).⁹ In practice, the lines always present some degree of broadening which is determined by the crystallite-size distribution, by the presence, nature and extension of lattice strains, and by the spectral distribution of energy. The peak profile can thus be regarded as a interaction of the spectral distribution of the X-ray radiation with the instrument (instrumental broadening) and the real structure of the sample (sample broadening). A flexible and physically meaningful description of the profile function of a powder diffraction peak is crucial for the precise determination of peak parameters like the position, FWHM, and intensity. Especially for intensity extraction from single peak or whole powder pattern fitting, the selection of the 'correct' peak profile function mainly determines the quality of the results.

Pseudo-Voigt function: If all geometrical and physical properties of the X-ray source, the diffractometer and the sample were known, it would be straightforward to calculate the peak profile function. In practice the realization of such procedure is quite complicated; for routine work semi-empirical functions describing the entire profile of a powder pattern using only few refinable and physically

meaningful parameters are used. Since most contributions to the line profile can somehow be related to Lorentz or Gauss distributions, a combination of the two functions is often used, the so called pseudo-Voigt function.

Axial divergence: The diffracted radiation in X-ray powder diffraction is distributed over cones (Debye-Scherrer cones) with opening angle 4θ . These cones intersect the surface of a cylinder that contains the receiving slit of the detector forming ellipsoids. Only the segments of ellipsoids which have the same height as the receiving slits are measured. The smaller the diffraction angle, the smaller the radius of the diffraction cones and the larger the bending of the ellipsoids and therefore the asymmetry of the recorded diffraction peaks. The asymmetry is further increased by the height of the sample, which causes additional diffraction cones with axes above and below the central cone.

Sample broadening: Two sources for broadening of the powder diffraction profiles are related to the sample history, namely:

Crystallite size: In 1918 Scherrer introduced a treatment approaching the particle size effect.¹¹ According to Scherrer, it is possible to determine the average coherence length, which can be roughly approximated to the average crystallite size, by measuring the FWHM of the diffraction peaks corrected for the contributions from the diffractometer. The thickness of a crystallite consisting of p lattice planes of thickness d calculates to

$L_{hkl} = p \cdot d$. The relation between L_{hkl} and the FWHM of the diffraction peak can be derived from the Bragg equation

$$B_{hkl} = 4\varepsilon_{1/2} = \frac{4 \cdot 1.4\lambda}{2\pi p d \cos\theta} = \frac{0.89\lambda}{L_{hkl} \cos\theta} \quad (3.14)$$

where B_{hkl} is FWHM, λ the wavelength of incident beam, L the average size of crystallites, and θ the diffraction angle. The instrumental contribution can be subtracted from the experimental data by running a strain-free, flawless standard either mixed with the sample or in a separate experiment under the same conditions, or by annealing part of the sample and obtain its diffraction pattern. The annealed material supposedly consists of perfect crystals large enough so that any line broadening should be caused solely by instrumental effects. By subtracting these effects from the pattern of the non-annealed sample, the remaining broadening is due to the particle size distribution.

Lattice strain: Strain in a crystal lattice is a distribution of lattice parameters around an average value caused by defects, not by an external force. A sample with anisotropic strain produces peak broadening in reciprocal space which is augmenting with increasing distance of the reflections from the origin.

The Rietveld Method

The Rietveld¹² method consists of calculating the entire powder pattern using a variety of refinable parameters. The calculated intensity $y_{i(calc)}$ for a mixture of phases p contributing H Bragg reflections to the pattern at point i of the powder pattern is given by

$$y_{i_{calc}} = \sum_p \left(S_p \cdot \sum_{pH} \left(M_{pH} \cdot A_{pH}(2\theta_i) \cdot P_{pH} \cdot |F_{pH_{calc}}|^2 \cdot LP(2\theta_i) \right) \right) + B_{i_{obs}} \quad (3.15)$$

where S_p , M_{pH} , $A_{pH}(2\theta_i)$, P_{pH} , $|F_{pH_{calc}}|^2$, $LP(2\theta_i)$, $\Phi_{pH}(2\theta_i)$, and $B_{i_{obs}}$ represent the scale factor, multiplicity, absorption correction, preferred orientation correction, squared absolute value of the structure factor, Lorentz-polarization correction, normalized profile function, and background contribution, respectively. These parameters can roughly be divided into three categories: structural parameters, which mainly affect the intensity of the Bragg reflections; profile parameters, which are determined by the instrument and the sample; and background parameters. For the calculation of any single point of the diffraction pattern, all reflections contributing to this point as well as the height of the background must be taken into account. The scale factor is used for quantitative phase analysis, the structure factor for refinement of the crystal structure, and the profile function for the refinement of the micro-structure (micro-strain, domain size). The weighted sum of the squared differences between the observed and the calculated powder pattern is minimized by refining a selection of parameters using least squares methods. The quality of a Rietveld

refinement is commonly judged using the weighted profile R_{wp} -factor:

$$R_{wp} = \sqrt{\frac{\sum_i w_i (y_{i_{obs}} - y_{i_{calc}})^2}{\sum_i w_i y_{i_{obs}}^2}} \quad (3.16)$$

The graphical representation of a Rietveld refinement shows the observed powder pattern, the best Rietveld fit profile, the reflection positions and the difference curve between observed and calculated profiles as the trace below. Due to the decrease of scattering power at higher diffraction angles, the high angle part is often enlarged. The major advantage of the Rietveld procedure is the iterative improvement of the structural information. On the other hand, a reasonably good structural model is required in advance to ensure the convergence of the refinement.

The LeBail Method

The LeBail¹³ method is a widely used technique to refine the total envelope of a powder pattern without knowing the crystal structure and to extract intensities which can later be used for crystal structure determination by direct methods. The basic idea is relatively simple as the Le Bail method iterates the Rietveld decomposition formula, meaning that whereas calculated structure factors $|F|$ are entered in the Rietveld decomposition formula, a set of identical $|F|$ is given instead. The Rietveld refinement calculates a set of “ $|F_{obs}|$ ” from the decomposition formula, which are then used as new $|F_{calc}|$ and so on.

3.2.2 Experimental

X-Ray Powder diffraction (XRD) patterns of the compounds were obtained using Siemens D5000 or Bruker D8 Advantage diffractometers using $\text{CuK}\alpha$ radiation; both diffractometers are equipped with diffracted beam monochromator. The analysis of air-sensitive samples was done under argon atmosphere using a homemade hermetically sealed sample holder (Figure 3.4).

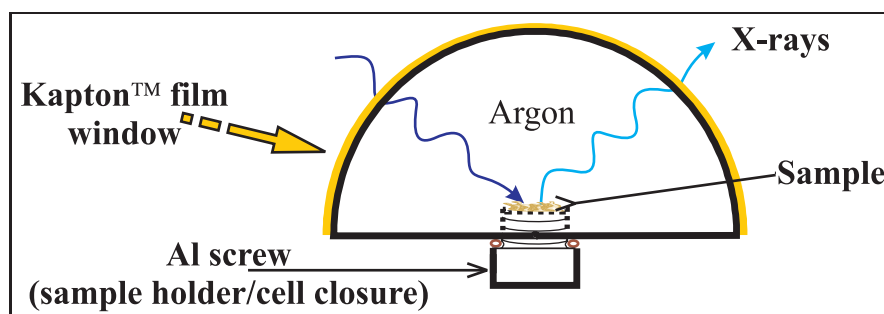


Figure 3.4: Schematic representation of XRD sample holder for air-sensitive material.

3.3 Electron Microscopy

Electron microscopy (EM) takes advantage of the wave nature of rapidly moving electrons. Whereas visible light has wavelengths from 4000 to 7000 Å, electrons accelerated to 10 keV have a wavelength of 0.12 Å, well suited as an inter-atomic probe. For the same reason, optical microscopes have their resolution limited by the diffraction of light to about 1000 diameters magnification while modern electron microscopes scan specimens with resolution of 1 nm at magnifications of up to

1 million times.

Electron microscopes are often coupled with x-ray analyzers. The interactions between high energy electron beam and sample generated x-rays are characteristic of the elements present in the sample. Placing a suitable detector (Energy Dispersive X-ray detector, EDX) near the specimen allows for the determination of the sample composition as well as distribution of elements throughout the surface. Quantities down to one thousandth of a picogram or less can thus be detected.

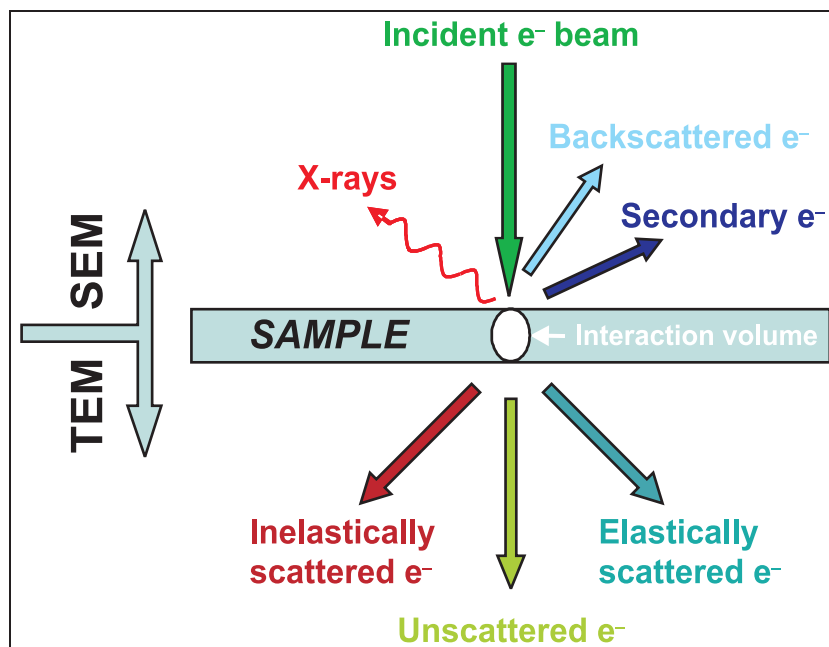


Figure 3.5: Schematic representation of Scanning and Transmission Electron Microscopy.

When using a Scanning Electron Microscope (SEM), insulating or poorly conductive samples are first coated with a metal that readily reflects electrons. This coating also provides a conducting surface for electrons to avoid charging of the

sample. The incoming electron beam is condensed into a small beam which is scanned over the object. An image is formed by the electrons that bounce off the surface of the specimen and are then collected onto the imaging screen. The observer therefore sees a picture of the surface of the sample, without any internal information.

The primary imaging method used in SEM (Figure 3.5) is by collecting secondary electrons that are released by the sample. The secondary electrons are detected by a scintillation material that produces flashes of light from the electrons. The light flashes are then detected and amplified by a photomultiplier tube. By correlating the sample scan position with the resulting signal, an image strikingly similar to what would be seen through an optical microscope forms, with quite natural looking surface topography. Another imaging mode uses the intensity of the electrical current induced in the specimen by the illuminating electron beam to produce an image, often used to show subsurface defects. A third option is the analysis of backscattered high energy electrons that emerge nearly 180 degrees from the illuminating beam direction. The backscatter electron yield is a function of the average atomic number of each point on the sample, and thus can give compositional information.

In Transmission Electron Microscopy (TEM, Figure 3.5) the image formed is a projection of the entire object under investigation, including the surface and internal structures. An electron beam is focused onto a thin sample and magnetic lenses focus the image onto a fluorescent screen, a film plate or a video camera. With samples of 200 nm thickness, scattering from the interaction with matter are limited

and beam coherence is maintained. In the presence of crystalline phases, a diffracted beam also originates from the sample. Two imaging modes are defined in TEM, namely Bright Field (when the aperture is positioned to pass only the transmitted electrons) and Dark Field (when the aperture is positioned to pass only specific diffracted electrons). Contrast images can be originated by transmission, showing inhomogeneities in thickness or composition (with light and heavy atoms unevenly distributed), or by diffraction. In the vicinity of a lattice defect, a diffraction inhomogeneity may occur, which corresponds to a local variation of the diffracted vs. transmitted intensity. In high-resolution mode at high magnification, periodic fringes may be visible representing a direct resolution of Bragg diffraction planes. The observed contrast is then referred to as a phase contrast. In addition to the direct image, a diffraction pattern of a selected area of the specimen can be generated by positioning an intermediate aperture in the image plane of the objective lens. The image formed by Selected Area Electron Diffraction (SAED) is a series of spots or rings which reflect the reciprocal space of the crystal lattice. The distance r between the spots is related to d , the interplanary spacings of the crystals, by the “camera equation”:

$$rd = \lambda L \quad (3.17)$$

where the camera-length, L , is characteristic of the microscope.

3.3.1 Experimental

SEM

SEM analysis of pristine and cycled samples were performed using a LEO Gemini 1530 microscope with Field Emission Gun XL-30 using both secondary and backscattered electrons for imaging and an EDX detector for compositional evaluation. Small amounts of samples were loaded on a holder previously covered with carbon tape. To prevent charging, all samples were coated with a thin layer of gold using a sputtering device. Air sensitive cycled samples were assembled inside an argon filled glove-box and transferred to individual air-tight vials and from these to the coating chamber under nitrogen flow.

TEM

TEM analysis of pristine and cycled samples was performed using a Phillips CM12 microscope equipped with an EDX detector. Both bright and dark field images were obtained as well as selected area diffraction patterns of crystalline samples. The specimens were prepared by immersing a carbon grid in a suspension of the sample in dry hexane. Air sensitive samples were mounted on the sample holder inside an argon filled glove-box, enclosed in an air-tight plastic bag and then quickly transferred to the vacuum chamber to avoid contact with air.

3.4 X-ray Photoelectron Spectroscopy

3.4.1 Principles

The principle of photo-emission was first explained by Einstein in 1905, in the frame of his theory on light quanta.¹⁴ Photons can interact and transfer energy to electrons, exciting them from an occupied to a higher unoccupied state. If the excitation energy $h\nu$ is larger than the binding energy W of the electrons to a system, the electron will escape the system with a kinetic energy E_k (Figure 3.6). According to the energy conservation principle:

$$E_k = h\nu - W \quad (3.18)$$

A solid sample irradiated with x-rays in vacuum emit electrons that can be counted

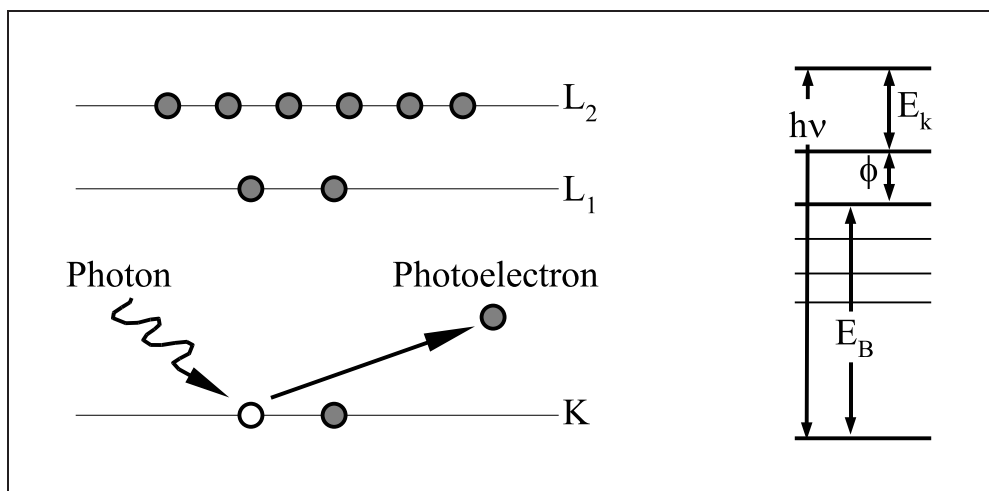


Figure 3.6: Schematic representation of the photo-emission process (E_B refers to the binding energy).¹⁵

within a selected energy range to obtain the energy distribution curve, a plot of the number of electrons collected as a function of their kinetic energy. The number of collected electrons corresponds in a first approximation to the density of (occupied) electronic states (DOS). For convention, W is split into two terms, the binding energy BE and the work function Φ , so that the energy distance of the emitting electronic state from the sample Fermi level (E_F) is BE , which is the typical value used to represent the energy scale. Equation 3.18 can then be written as

$$E_k = h\nu - (BE + \Phi) \quad (3.19)$$

Sample and spectrometer are kept in electrical contact to achieve a common Fermi level; however, the analyzer work function Φ^S is generally different from that of the sample. The kinetic energy E_k^S measured by the analyzer differs from E_k because of the acceleration (or retardation) due to the electrical field between sample and analyzer. The measured kinetic energy is thus

$$E_{kin}^S = h\nu - (BE + \Phi^S) \quad (3.20)$$

If a metallic sample is used, E_k^S measured for the Fermi edge ($BE = 0$) can be readily identified as the largest kinetic energy where signal is detected. Given the photon energy, the Φ^S plus BE scale is obtained:

$$E_k^{S(E_F)} - E_k^S = BE \quad (3.21)$$

Photoelectron spectroscopy is based on photonic excitation from a monochromatic source.¹⁵ Two adequate light sources and therefore two different techniques are

known, namely XPS and UPS (X-ray and Ultraviolet Photoelectron Spectroscopy, respectively) as summarized in Table 3.1. Because electrons must travel from the sample to the analyzer, a vacuum of at least 10^{-6} mbar is required. Owing to the technique's surface sensitivity, any adsorbate present (chemical or physical) significantly alters the spectra. With a partial pressure of 10^{-10} mbar, one mono-layer of species with unity sticking probability would deposit in 3 hours; practically, a total pressure 10^{-10} mbar generally prevents contamination for a period much longer than the time required for the measurement. These vacuum levels can be achieved with standard UHV (Ultra High Vacuum) equipment based on turbo molecular pumps connected to rotary vane or membrane rough pumps – typically able to reach a pre-vacuum of $4 \cdot 10^{-2}$ mbar. In the absence of leaks, after venting, pressures of the order of 10^{-10} mbar are promptly reached by baking the system for at least 8 hours at $130 - 180$ °C, depending on the chamber size. Each element has a characteristic disposition of electronic states that can be easily recognized in a spectrum which extends between 1000 and 0 eV. With the exception of H and He, each element can be detected down to a sensitivity of the order of 0.1 atom percent. The peak position can vary within several eV, depending on the element's chemical environment, which can be used for chemical identification. Usually, the larger the electron density at an atom, the lower the *BE* of the corresponding core levels. As a consequence, the oxidation state of the species controls the chemical shift (electrons from a more reduced atom have a lower binding energy) and the differences can reach some units

Table 3.1: Types of photoelectron spectroscopy according to photon source.

Spectroscopy	Photon Type	Source	Application
XPS	X-rays	Al and Mg $K\alpha$	Core Level Orbitals
		Synchrotron	Adsorbates and Surface States
UPS	UV	He $I\alpha$ and $II\alpha$	Valence Shells Molecular Orbitals Energy Bands

of eV. Characteristic binding energies for many compounds are given in several literature surveys.¹⁵ The peak positions may also change due to sample charging after the ionization process. For conducting specimens this is avoided because emitted electrons are replaced with an electron flow from the spectrometer in electric contact with the sample. In insulators a static charge (usually positive) builds up, changing the observed binding energies by up to several eV. This change can be minimized using a low energy flood gun or ion neutralizers.

3.4.2 Experimental

XPS analysis was performed using a VG Scientific XPS Microprobe ESCALab 250 (with focused monochromatic Al $K\alpha$ radiation of energy 1486.6 eV, with a chamber pressure $<10^{-10}$ mbar) on an irradiated area of $0.4 \times 1 \text{ mm}^2$. The cycled samples

were opened in the dry-box, washed with acetonitrile and transferred to the XPS analysis chamber through a sample load-lock system to prevent air exposure. Charge compensation was employed during data collection using a combination of a low energy flood gun and low energy ions. The electron binding energies were calibrated setting the positions of Cu $3p$ at 75.14 eV.¹⁶ Throughout this text (Chapter 6), the binding energies are given as the difference from the Fermi level. Thus, a lower kinetic energy corresponds to a higher BE. The peaks corresponding to the core levels are indicated with the main quantum number and the orbital angular momentum (s, p, d, f) of the hole left in the final state.

3.5 X-ray Absorption Spectroscopy

The intensity of an X-ray beam is attenuated after passing through a medium according to

$$I = I_0 e^{-\mu t} \quad (3.22)$$

where I_0 and I are the intensities of incident and transmitted beams and μ and t the linear absorption coefficient and thickness of the absorber. EXAFS (Extended X-ray Fine Structure) and XANES (X-ray Absorption Near Edge Structure) spectroscopies are based on the measurement of the absorption coefficient μ as a function of the photon energy E above the threshold of an absorption edge. A photoelectron ejected from X-ray absorption by an isolated atom travels as a spherical wave. In the presence

of neighbouring atoms, however, the outgoing photoelectron can be backscattered. The outgoing and incoming wave can interfere either constructively or destructively causing an oscillatory behaviour of the absorption rate. The amplitude and frequency of the sinusoidal modulation of μ vs. E depend on the number, type, and bonding of the neighbouring atoms and their distances away from the absorber.¹⁷ Figure 3.7 illustrates this process qualitatively.

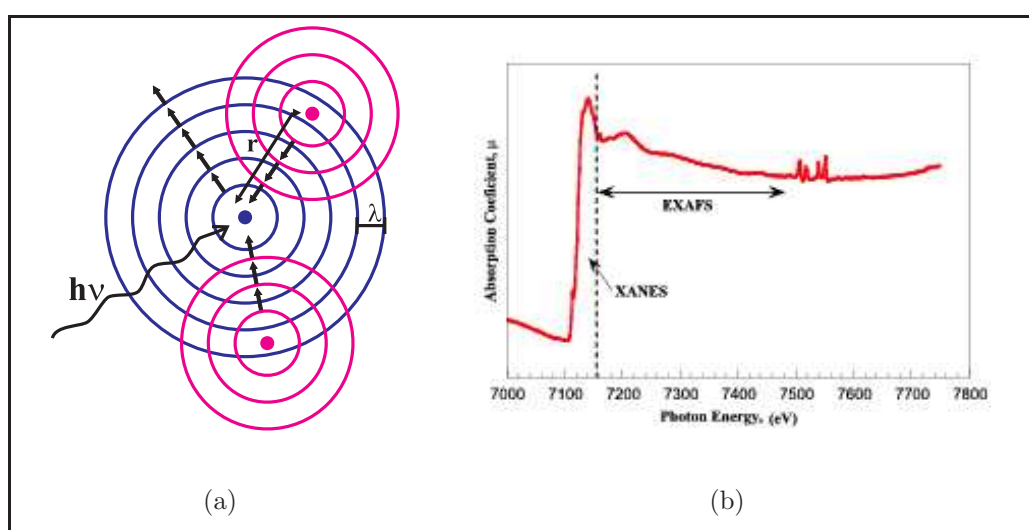


Figure 3.7: Schematic representation of (a) electron backscattering process and (b) resulting spectrum in XAS experiment.

In XANES analysis, the region of the absorption edge is under scrutiny. The exact position of the edge depends upon the oxidation state, site symmetry, surrounding ligands, and nature of bonding.¹⁸ On the other hand, in EXAFS a wider energy range is examined (up to 1 keV above the absorption edge). Fourier transform can be employed in the analysis of the ripple pattern present in this region, providing

information on local structure and bond distances. Because in EXAFS the absorption edge of each element present in a sample can be monitored, the local structure of each element may be determined. As a result, EXAFS constitutes a valuable tool for studying disordered materials.

3.5.1 Experimental

XAS analysis of pristine and cycled FeP₂ samples (Chapter 5) was performed at LURE (Orsay, France) using X-ray synchrotron radiation emitted by the DCI storage ring (1.85 GeV, average intensity 250 mA). Data were collected in the transmission mode at the FeK edge on XAS 4 spectrometer, using a double-crystal monochromator Si(111) for EXAFS analysis and Si(311) for XANES analysis. XANES spectra were recorded by steps of 2 eV with 1 second of accumulating time per point within the 7060–7090 and 7140–7310 eV energy range and 0.25 eV with an accumulating time of 1 second between 7090 and 7140 eV. For each sample, three EXAFS spectra were recorded between 7000 and 8100 eV, with an accumulating time of 2 seconds for each point, split by 2 eV steps. The analysis of the data was performed in a classical way using the WINXAS code.¹⁹ The amplitude and phase functions were extracted from the F_{eff} tables.

3.6 Magnetic Measurements

Materials may be classified by their response to externally applied magnetic fields as diamagnetic, paramagnetic, or ferromagnetic, which differ greatly in strength. *Diamagnetism* is a property of all materials and opposes applied magnetic fields, but is very weak. *Paramagnetism*, when present, is stronger than diamagnetism and produces magnetization proportional to and in the direction of the applied field. *Ferromagnetic* effects produce magnetizations sometimes orders of magnitude greater than the applied field and as such are much stronger than either diamagnetic or paramagnetic effects. The magnetization of a material is expressed in terms of density of net magnetic dipole moments m in the volume V of material. The *magnetization* M is defined by $M = m_{total}/V$ so the total magnetic field B in the material is given by

$$B = B_0 + m_0 M \quad (3.23)$$

where m_0 is the *magnetic permeability* of space and B_0 is the externally applied magnetic field. When magnetic fields inside of materials are calculated using Ampere's law or the Biot-Savart law, then the m_0 in those equations is replaced by just m which is defined as

$$m = K_m m_0 \quad (3.24)$$

where K_m is the relative permeability. If the material does not respond to the external magnetic field by producing any magnetization, then $K_m = 1$. For diamagnetic

materials the relative permeability is very close to 1 and the magnetic susceptibility very close to zero. Paramagnets, on the other hand, exhibit mass susceptibilities in the range $10 - 300 \text{ m}^3/\text{kg}$, whereas for ferro-, ferri-, and antiferromagnetic materials, these quantities can reach values in the order of $100000 \text{ m}^3/\text{kg}$. Another way to deal with the magnetic fields which arise from magnetization of materials is to introduce a quantity called *magnetic field strength* H , defined by the relationship

$$H = \frac{B_0}{m_0} = \frac{B}{m_0} - M \quad (3.25)$$

The magnetic field strength unambiguously differentiates the magnetic influence from external currents in a material, independent of the material's magnetic response. The relationship for B above can be written in the equivalent form

$$B = m_0 (H + M) \quad (3.26)$$

The ratio of the magnetization M to the applied field H is defined as the *magnetic susceptibility*:

$$\chi = \frac{M}{H} \quad (3.27)$$

3.6.1 SQUID

A SQUID (Superconducting Quantum Interference Device) consists of a closed superconducting loop. If a sample is moved through the superconducting coils, it induces an electric current in the detection coils that is proportional to the change

in magnetic flux. Hence, the SQUID functions as a highly linear current-to-voltage convertor, so the variations in the voltage output are proportional to the magnetic moment of the sample.

3.6.2 Mössbauer Spectroscopy

The recoil-free absorption of γ -ray photons by nuclei in a crystalline solid is known as the Mössbauer effect. One of the few isotopes which exhibits the Mössbauer effect is ^{57}Fe which is naturally occurring in iron. The Mössbauer effect is used in the corresponding spectroscopy in which a radioactive element is mechanically vibrated back and forth to Doppler shift the energy of the emitted gamma radiation. The source is moved relative to the sample and the intensity of the beam after it has passed through the sample is monitored (Figure 3.8). The shift of the energy levels

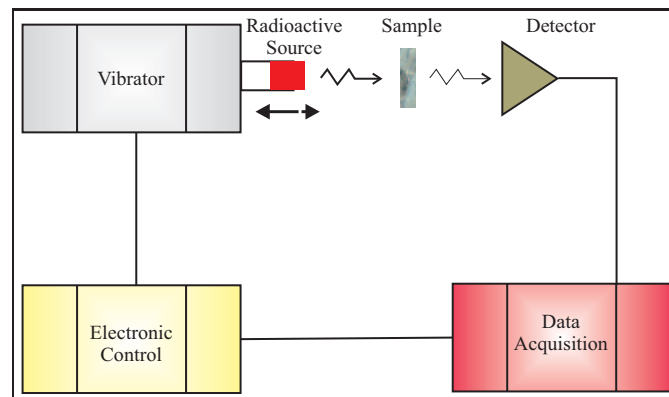


Figure 3.8: Schematic representation of Mössbauer effect and spectroscopy.

of the target nuclei, due to a variation in atomic environment, is measured in the

absorption spectrum as a function of velocity. If the sample nuclear levels are not split and the $I = 3/2$ to $I = 1/2$ transition energy equals that of the source, then the effective cross-section for absorption is a function of gamma energy as given by²⁰

$$s_{eff} = [(2^{I^*} + 1)/(2I + 1)][l^2/2p][f'/2(1 + a)]G_{nat}^2/[(E - E_g)^2 + G_{nat}^2] \quad (3.28)$$

where $I = 1/2$ and $I^* = 3/2$ are the ground and excited nuclear spins, $a = 9.0$ is the internal conversion coefficient (ratio of betas to gammas in the 14.4 keV decay), $l = 8.61 \times 10^{-9}$ cm is the wavelength of the radiation, $E - E_g$ is the difference between mean incident and resonant gamma energy, G_{nat}^2 is the energy width of the excited nucleus, and f' is the probability of recoilless absorption. The spectrum will be a single Lorentzian centered at $v = 0$ with a line-width (FWHM) of $2G_{nat} = 0.19$ mm/sec. Hyperfine interactions will split the nuclear levels of the sample and complicate the Mössbauer spectrum.

Isomer Shift

The nucleus and its electrons interact in several ways, the most obvious being the electrostatic attraction. In fact the excited Fe^{57} nucleus is 0.1% smaller in radius than the ground state nucleus, which causes the Mössbauer transition energy to depend on the electron density at the nucleus. This effect produces the so-called isomer shift of the Mössbauer spectrum, which may be written as

$$\delta = KS_s|y_0|^2 - S_a|y_0|^2 \quad (3.29)$$

where d is the isomer shift, K is a positive constant depending on the change in the nuclear radius, $S_s|y_0|^2$ is the electron density at the source nucleus, and $S_a|y_0|^2$ is the electron density at the absorber nucleus. The isomer shift provides information on the valence state of the absorber. To allow isomer shifts to be measured independently of the nature of the source, the centroid of the room temperature spectrum of metallic iron has been adopted as the zero of energy level and all shifts are measured relative to it. This convention yields

$$\delta_n = K_0 - K S_a |y_0|^2 \quad (3.30)$$

where K_0 is a constant. The 1s and 2s electron density at the nucleus is independent of the chemical environment of the Fe ion. However, the 3d electrons shield the 3s electrons and cause a decrease in the electron density at the Fe⁵⁷ nucleus. The more delocalized the 3d electrons, the smaller the isomer shift.²¹ The electronic contribution to the isomer shift is essentially temperature-independent but a decrease at high temperatures occurs due to the relativistic second order Doppler shift.

Electric Quadrupole Interaction

The excited state of the Fe⁵⁷ nucleus possesses an electric quadrupole moment, and the presence of a low symmetry electric field will tend to orient the nuclear spin. The interaction may be written as

$$H^Q = -(Q/6) I V \quad (3.31)$$

where Q is the nuclear quadrupole moment, I is the nuclear spin, and V is the electric field gradient (efg) tensor. Reversal of the sign of the nuclear spin does not change the nuclear charge distribution. Therefore, the efg incompletely lifts the fourfold degeneracy of the $I = 3/2$ states; the quartet is split into two doublets, while the $I = 1/2$ states remain degenerate. Since two transition energies are now possible, two absorption peaks will appear in the Mössbauer spectrum. If the recoil-free fraction does not depend on the orientation of the γ -beam relative to the Fe site, a sample with randomly oriented sites in zero applied field will produce a symmetric quadrupole pair.²¹

Magnetic Hyperfine Interaction

The Fe^{57} nucleus possesses a magnetic moment and its energy levels will be perturbed by the local magnetic field. Depending on the magnetic properties of the sample, the internal field may or may not equal zero in the absence of the applied field. The magnetic interaction is given by the sum of:²¹ (i) the field at the nucleus due to the orbital motion of the electrons, (ii) the field due to the dipole moment of the electrons, (iii) a Fermi contact term which accounts for any net polarization of the electronic spin at the nucleus.

3.6.3 Experimental

Magnetic susceptibility and hysteresis loop measurements of pristine and cycled FeP₂ samples (Chapter 5) were obtained with a SQUID MPMS 9T magnetometer. The magnetic susceptibility $\chi(T)$ was measured in zero-field cooling (ZFC) and field cooling (FC) modes in the temperature range 2–350 K and with an applied field of 500 G. The magnetization curves $M(H)$ were obtained after cooling the sample to the measurement temperature in zero field and then increasing the field from 0 to 5 G. In all cases, the powders were compacted into quartz sampling tubes; cycled samples were prepared inside an argon filled glove-box.

The ⁵⁷Fe Mössbauer spectra of pristine and cycled FeP₂ samples (Chapter 5) were recorded using a ⁵⁷Co/Rh γ -ray source mounted on an electromagnetic drive and using a triangular velocity form. Spectra were obtained in zero magnetic field at 78 K. The Mössbauer spectra were analyzed by least-squares fitting to a Lorentzian function. The isomer shifts (IS) were referenced α -Fe at 300 K. The sample (area = 3 cm²) was prepared by dispersion of the material (100–140 mg) in a specific resin.

References

- [1] Weppner, W.; Huggins, R. *J. Electrochem. Soc.* **1977**, *124*, 1569.
- [2] Weppner, W.; Huggins, R. *Ann. Rev. Mater. Sci.* **1978**, *8*, 269.
- [3] Thompson, A. *Phys. Rev. Lett.* **1978**, *40*, 1511.
- [4] Thompson, A. *J. Electrochem. Soc.* **1979**, *126*, 603.
- [5] Chabre, Y. *J. Electrochem. Soc.* **1991**, *128*, 329.
- [6] Chabre, Y. *NATO ASI Series* **1992**, *B305*, 181.
- [7] Southampton Electrochemistry Group, *Instrumental Methods in Electrochemistry*; Ellis Horwood Series in Physical Chemistry John Wiley & Sons: Chichester, 1985.
- [8] Hanawalt, J.; Rinn, H.; Frevel, L. *Ind. Eng. Chem. Anal. Ed.* **1938**, *10*, 457.
- [9] Klug, H.; Alexander, L. *X-Ray Diffraction Procedures for Polycrystalline and Amorphous Materials*; John Wiley & Sons: New York, 2nd ed.; 1974.

- [10] International Union of Crystallography, *International Tables of Crystallography*; volume I-IV D. Riedel: Holland/Boston, 1983.
- [11] Scherer, P. *Zsigmondy's Kolloidchemie*; Verlag: Berlin, 3rd. ed.; 1920.
- [12] Rietveld, A. *Acta Cryst.* **1967**, *22*, 151.
- [13] LeBail, A.; Duroy, H.; Fourquet, J. *Mater. Res. Bull.* **1988**, *23*, 447.
- [14] Einstein, A. *Ann. Phys.* **1905**, *17*, 132.
- [15] Chastain, J., Ed.; *Handbook of X-ray Photoelectron Spectroscopy*; Perkin Elmer Corporation: Eden Prairie, 1992.
- [16] Seah, M. *Surf. Interf. Anal.* **1989**, *14*, 488.
- [17] Teo, B. Extended x-ray absorption fine structure (EXAFS) spectroscopy: techniques and applications. In *EXAFS Spectroscopy Techniques and Applications*; Teo, B.; Joy, D., Eds.; Plenum Press: New York, 1979.
- [18] West, A., Ed.; *Basic Solid State Chemistry*; John Wiley & Sons, Ltd: Sussex, 1999.
- [19] Ressler, T. *J. Phys IV* **1997**, *C2*, 269.
- [20] Fraunfelder, H. *The Mössbauer Effect*; W.A. Benjamin: New York, 1963.
- [21] Greenwood, N.; Gibb, T., Eds.; *Mössbauer Spectroscopy*; Chapman and Hall: London, 1971.

Chapter 4

Manganese Phosphide System

4.1 Introduction

The desirable candidate for an anode material in lithium-ion batteries should present low formula weight, high lithium content variation, low redox potential relative to the pair Li/Li^+ , and highly reversible lithium uptake/extraction reactions. Following this rationale, new materials have been investigated as substitutes for graphitic carbon. Many transition metal pnictides have been known for years but none was evaluated for such applications until our seminal work,¹ although many subsequent publications have appeared since then (see Section 2.2.3, page 38).

4.1.1 Structure of MnP_4 and Li_7MnP_4

The phase diagram for the system Mn–P shows three metal rich (Mn_3P , Mn_2P , and Mn_3P_2), MnP, and one phosphorus rich (MnP_4) compound.² The first variant of manganese tetrphosphide was synthesized in 1975 and five years later two other variants were obtained, all with structure related to that of CrP_4 .³ The structure can be viewed as a stacking of puckered networks of manganese and phosphorus atoms. Bonding within and between the layers are of the same kind but the orientation and connectivity of the layers vary. Depending on the number of subsequent layers necessary for the formation a unit cell the three different manganese tetrphosphide phases are formed, namely 2-MnP_4 , 6-MnP_4 , and 8-MnP_4 . Manganese is in distorted octahedral coordination with six P in all structures; however, the octahedra are connected by edge or corner sharing depending on the stacking order of the structure. Figure 4.1 shows the polyhedral representation for the three structures.

Li_7MnP_4 crystallizes with the antiferite-type structure in the space group $\text{Fm}\bar{3}\text{m}$ (Figure 4.2).⁴ Phosphorus atoms form a face-centered cubic (fcc) lattice, with parameter of about 5.977 Å and the tetrahedral sites are randomly occupied by lithium and manganese in a 7:1 ratio. Additionally, Juza and Bohmann reported the existence of thirteen other phases of general stoichiometry $\text{Li}_{8-x}\text{Mn}_x\text{P}_4$, where $0.67 \leq x \leq 4.0$; compounds with higher manganese contents ($x \geq 1.4$) crystallize in tetragonal symmetry.

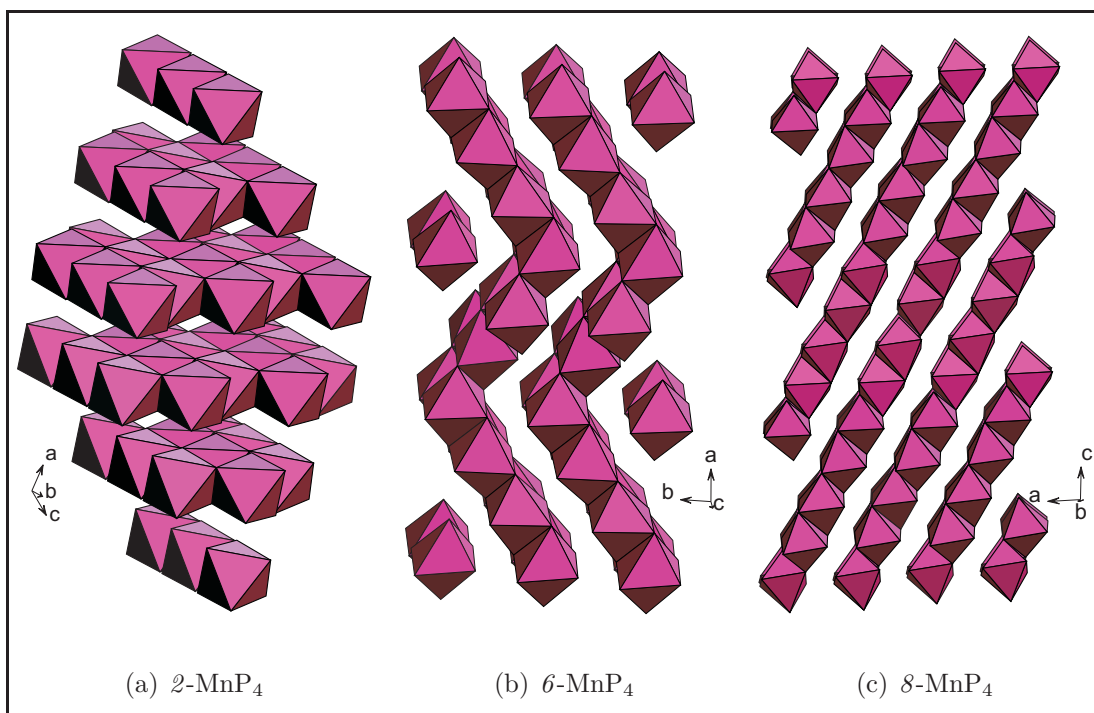


Figure 4.1: Polyhedral representation of the MnP_4 structures.

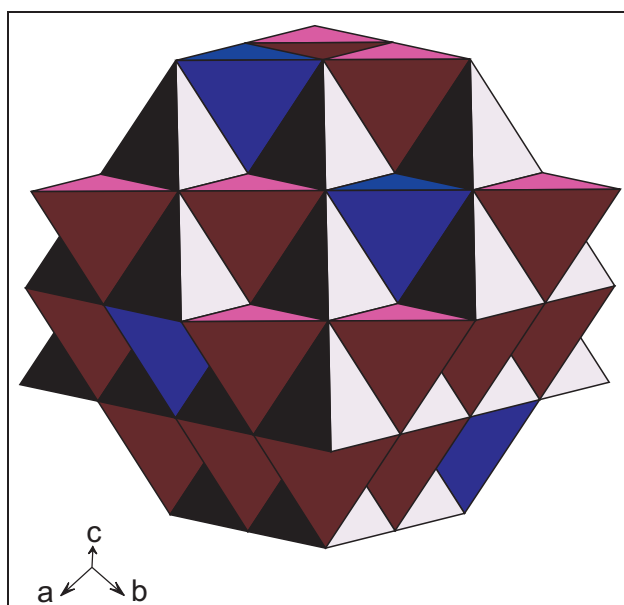


Figure 4.2: Polyhedral representation of the antifluorite-type Li_7MnP_4 structure.

The existence of thermodynamically stable lithiated and non-lithiated manganese phosphide phases with the same Mn:P ratio raises some questions: (*i*) can lithium ions be electrochemically added to the binary matrix? (*ii*) if so, is the process reversible? (*iii*) what is the structure of the lithiated phase obtained? (*iv*) what is the mechanism involved? Contemplation of these matters must not disregard the marked difference between the structures of Li_7MnP_4 and MnP_4 . Transformation between the two structures demands substantial rearrangement of the atoms within the lattice as well as bond breaking and reforming. These aspects were investigated and are reported herein.

4.2 Experimental

4.2.1 Synthesis of MnP_4

Appropriate amounts of manganese, red phosphorous, and tin were mixed inside an argon filled glove-box with the aid of a mortar and pestle and transferred to a quartz tube (18 mm OD x 16 mm ID). The tube was evacuated, sealed (final length ≈ 20 mm), transferred to a tube furnace and then heated to a specific temperature range for two weeks. After this period, the quartz tube was quenched to room temperature in a water bath. Table 4.1 summarizes the synthesis parameters employed in each reaction variant. The resulting solid material was treated with at least three portions of 1:1

aqueous solution of hydrochloric acid (to dissolve the Sn flux and excess P), manually ground with mortar and pestle, and sieved through a 400 mesh nylon grid.

Table 4.1: Parameters for synthesis of MnP_4 .

Variant	Molar Ratio			Reaction Temperature (°C)
	Mn	P	Sn	
2-MnP_4	1	10	2	570-630
6-MnP_4	1	10	6	600
8-MnP_4	1	10	6	630-670

4.2.2 Synthesis of Li_7MnP_4

Stainless-steel crucibles were made by crimping and arc-welding one end of 7 cm long pieces of tubing (0.903 cm OD x 0.703 cm ID). The crucibles were etched with a mixture of concentrated hydrofluoric, nitric and sulphuric acids (2:3:5 volumetric ratio, respectively), rinsed with distilled water, and dried at 125 °C for at least 2 hours. Afterwards, the crucibles were transferred to an argon filled glove-box, loaded with metallic lithium (0.365 g, 0.053 mol), manganese (0.412 g, 0.0075 mol), and phosphorus (0.92 g, 0.030 mol), and finally sealed by arc-welding under argon atmosphere. The tubes and their contents were heated for different lengths of time (12, 24, 48 hours, and 1 week) at 800 °C under a small flow of nitrogen. After quenching the reactions in a cold water bath, the tubes were returned to the glove-

box and cut open. Samples with different particle sizes were obtained by either hand-grinding, using a mortar and pestle and sieving through a 200 mesh nylon grid, or by ball milling. In the second case, a silicon nitride crucible was loaded with zirconia balls (7.5 mm in diameter) and 2 g of material inside an argon filled glove box and mounted onto a high energy planetary mill (Pulverisette® 6). The samples were milled at 500 rpm for different periods of time (15, 30, and 60 min) and using two different ball-to-powder mass ratios (1:9 and 1:15).

4.3 Characterization and Properties of MnP_4 and Li_7MnP_4

4.3.1 Structure and Composition of the Materials

The binary manganese phosphides were obtained as small black crystals. Figure 4.3 shows the diffraction patterns of the three variants, which match those reported in the literature.^{3,5,6} Similarly to the early findings, the products always contain very small amounts of another MnP_4 variant or, to a lesser extent, of a lower phosphide.

The methodology described in the scientific literature for the synthesis of Li_7MnP_4 consists of a multi-step procedure: (i) preparation of LiP by melting lithium in a tantalum open crucible (200 °C) and slowly adding small portions of phosphorus, taking care that the reaction temperature does not raise above 400 °C. After 2 to

3 hours at this temperature, the material is cooled to room temperature, ground, sealed inside a Ta tube and reheated at 600°C for 4 hours, (ii) preparation of Li_3P by reaction of LiP with lithium using exactly the same procedure and temperatures as for LiP, and (iii) reaction of Li_3P with manganese and phosphorus, first grinding the starting materials, pressing a pellet, sealing it in a stainless-steel tube, that in turn is sealed inside a quartz tube, annealing at 800 °C for 4-6 hours, and finally quenching in cold water and grinding.⁴

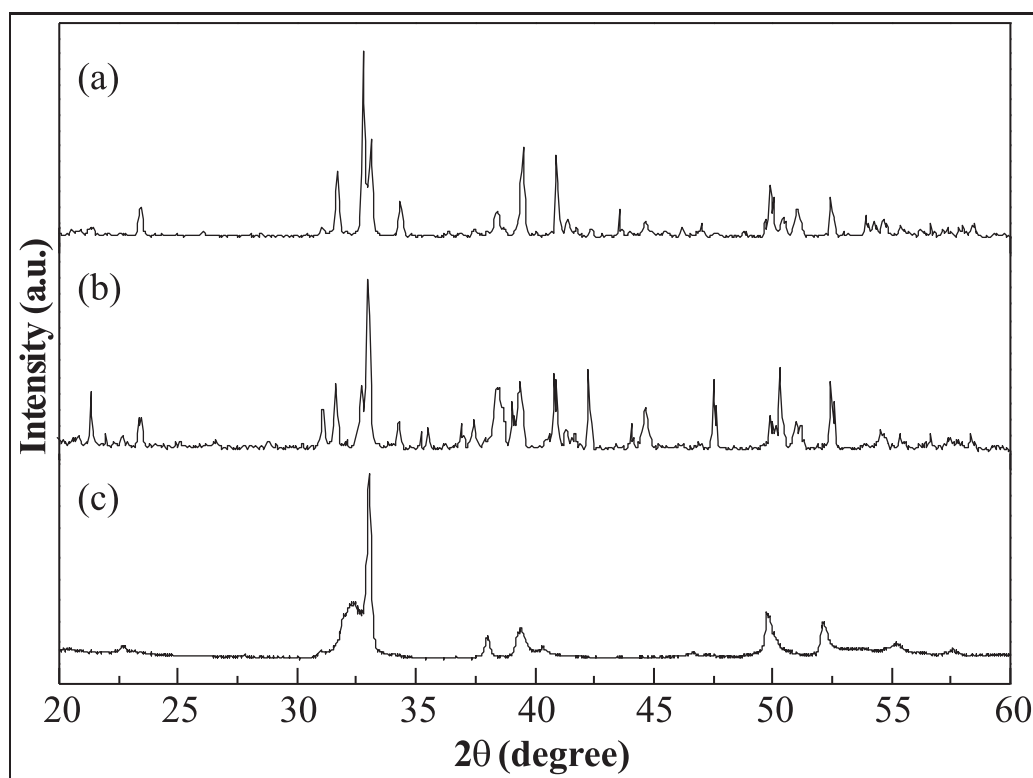


Figure 4.3: XRD patterns of the variants (a) 8-MnP_4 , (b) 6-MnP_4 , and (c) 2-MnP_4 prepared by the Sn flux technique.

Undoubtedly, this is an intricate and time consuming procedure; however, it

did indicate that stainless-steel was not attacked by the Li_3P , MnP , or Li_7MnP_4 phases. Based on this information, stainless-steel AISI-304 tubes were used to make the reaction crucibles. This is a much cheaper alternative than the commonly used noble metals (niobium, tantalum, and molybdenum). Although the melting point of the AISI-304 stainless-steel is in the range of 1400-1420 °C, the tube contents are very reactive and despite all manipulations being done under inert atmosphere, when transferred to the welding chamber the tubes were briefly exposed to air. In case a tube was not properly sealed, air could eventually penetrate the tube and reactions of the elements with oxygen and/or water could result in explosion. Additionally, oxidation of the crucible outer walls at high temperatures, thereby exposing the tube contents, would also promote fire and/or explosive reactions. For these reasons, the reactions were carried out under a small flow of nitrogen in order to reduce risk of accidents. All in all, the developed procedure, *i.e.* through direct reaction of the elements, constituted a much cheaper and safer route to obtain the desired ternary phosphide.

XRD results (Figure 4.4) show that reactions stopped before 24 hours produced materials contaminated with various amounts of LiP . The material obtained after 24 hours consisted of pure Li_7MnP_4 and, although above this time threshold one can see a slight improvement on the phase crystallinity, heating for 1 week promoted some decomposition of into LiP . The XRD analysis shows no evidence of sample contamination with by-products or decomposition of the crucible.

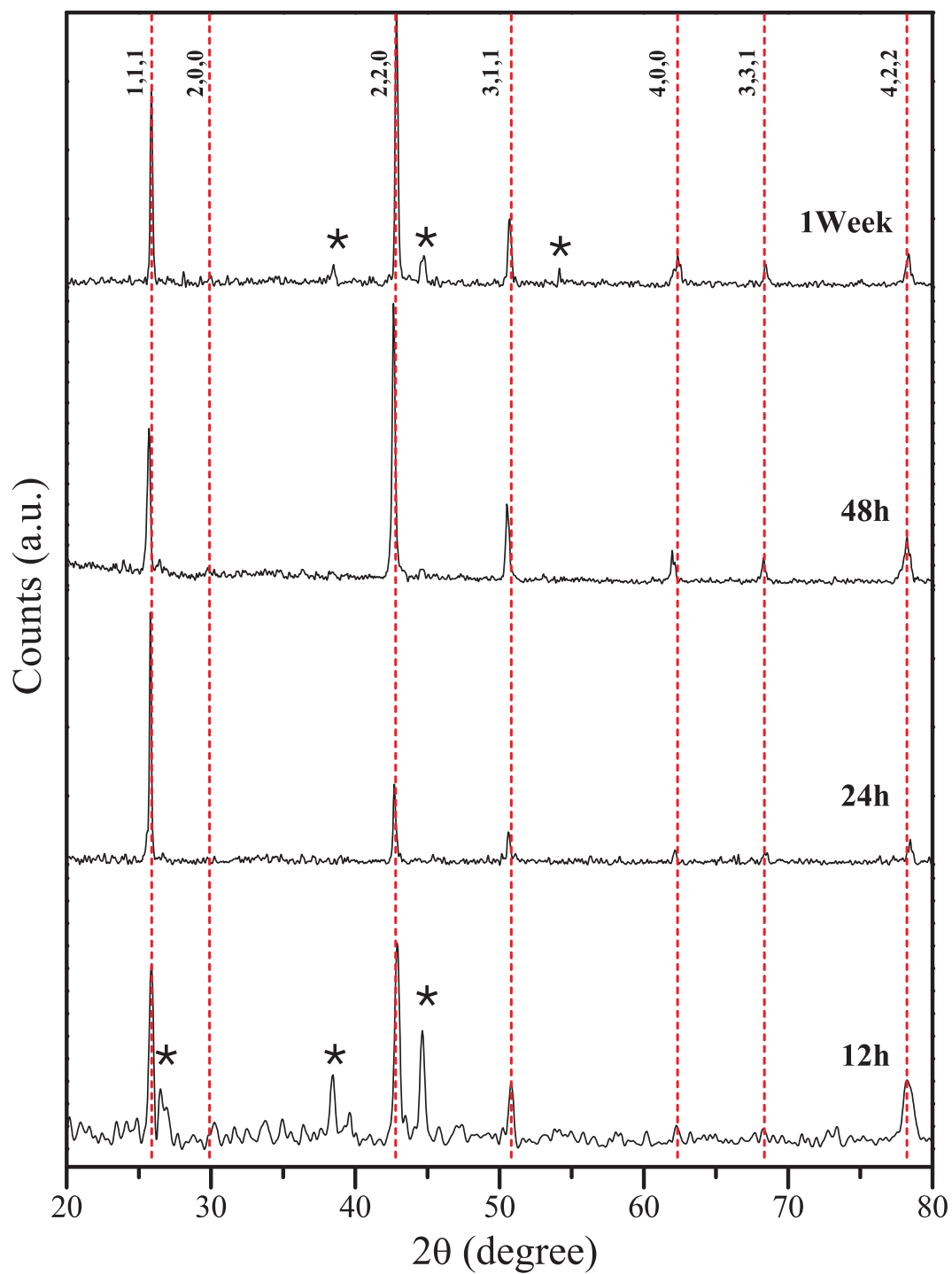


Figure 4.4: XRD patterns of Li_7MnP_4 samples obtained at 800°C after different reaction times; * depicts lines relative to LiP contamination.

High energy mechanical ball milling under inert atmosphere (N_2) was established as a safe and efficient process for reducing the particle size of Li_7MnP_4 samples. Elemental analysis of the milled samples based on SEM/EDAX confirmed the presence of manganese and phosphorus, and the X-ray patterns solely display broadened lines assigned to Li_7MnP_4 (Figure 4.5).

Using Scherer's equation (see Chapter 3 Section 3.2, page 75), the average coherence length (which can be roughly approximated to the average size of crystallites) of the ball-milled samples was determined and compared to the material before milling. The results obtained are presented in Table 4.2.

Table 4.2: Crystallite size of ball-milled Li_7MnP_4 samples determined by Scherer equation.

Sample	Crystallite Size (nm)
Li7B	27
Li7C	82
Li7D	27
Li7E	68

No decomposition of the Li_7MnP_4 phase upon ball milling can be observed by XRD, as shown in Figure 4.5; however, the particle size is noticeably reduced and, generally, their coherent path length decreases from 72 nm in the pristine material down to 27 nm in the ball-milled samples.

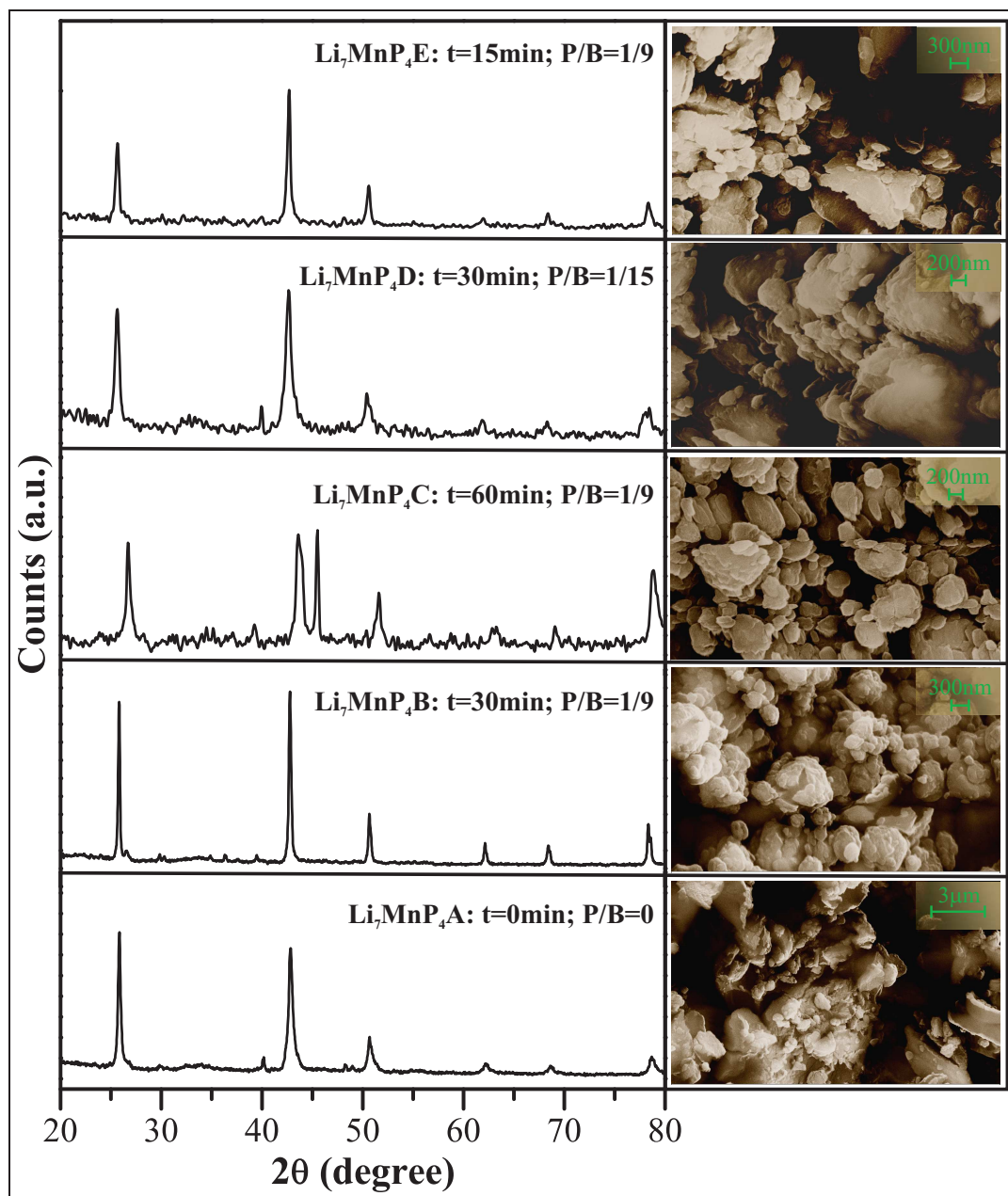


Figure 4.5: XRD and SEM of Li_7MnP_4 samples ball-milled under inert atmosphere for various length of time (t) using different powder to ball weight ratios (P/B).

4.3.2 Electrochemical Properties of Manganese Phosphide Systems

Figure 4.6(a) shows the performance of δ - MnP_4 during the first cycle between 0.57 V and 1.7 V at different galvanic rates. Little or no lithium uptake was observed at a rate of C/2 and up to seven Li^+ (corresponding to a specific capacity of 1050 mAh/g) were progressively inserted when the galvanic rate decreased to C/5 and C/10.

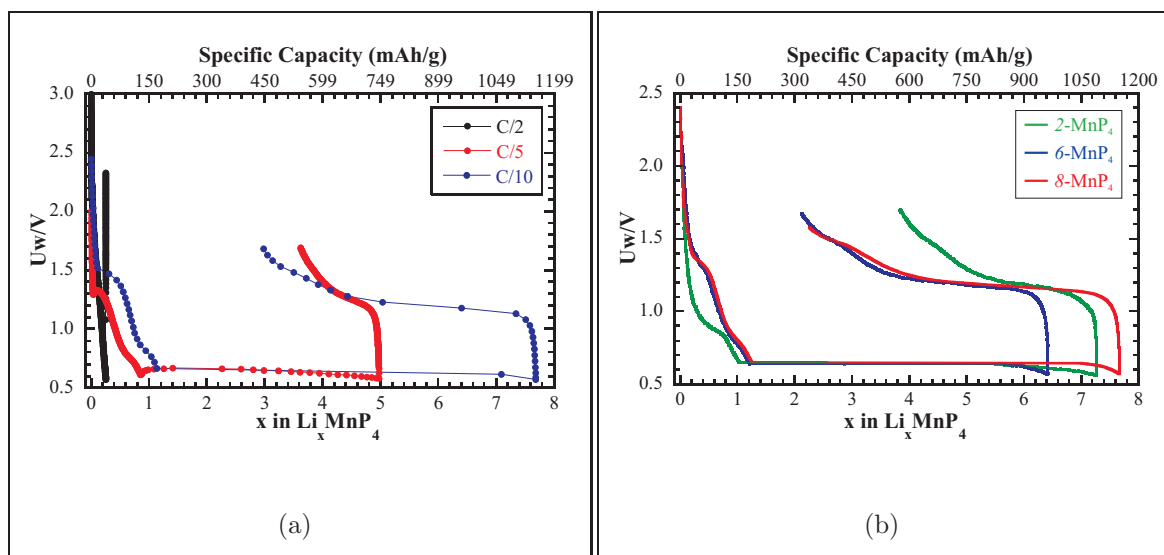


Figure 4.6: Galvanostatic voltage-composition profiles for (a) δ - MnP_4 at different rates and (b) different variants of MnP_4 at C/10.

Figure 4.6(b) reveals that the electrochemical profiles for different variants are quite similar both in terms of “intercalation” voltage and amount of lithium uptake. This suggests that the stacking fault does not interfere with the intercalation

mechanism. Therefore, since a larger amount of the δ - MnP_4 variant was obtained, the investigations proceeded using mainly this sample. All variants present a large polarization between discharge and charge voltages at any rate of intercalation. The equilibrium voltage for both processes was determined using GITT at very low rate (C/50). As Figure 4.7 reveals, the difference in the equilibrium voltages is only 30 mV indicating that the reduction and oxidation processes are indeed the same. The hysteresis observed in the voltage composition curves in Figure 4.6 result from the over-potential needed for the transport of the phase-boundary in the phase transformation process (see page 113).

The voltage-composition profile obtained for Li_7MnP_4 is very similar to that of the non-lithiated material (Figure 4.8) with up to 7 lithium ions being removed and re-inserted in the structure on the first cycle at equivalent voltages. Again, a large polarization between the charge and discharge segments is observed and the curves are also similar regarding the presence of *plateaus* at 0.64 V and 1.1 V on the discharge and charge sweeps, respectively, evidencing the occurrence of a binary (phase transformation or/and decomposition) process. From this result one can infer that the electrochemical behaviour of the electrodes does not depend on the starting material (lithiated or non-lithiated). In good agreement with the GITT data obtained for MnP_4 , the PITT curves (Figure 4.8(b)) show that the equilibrium voltages for oxidation and reduction are 1.07 and 1.02 V, respectively. Gillot and co-workers calculated the density of states diagram for Li_7MnP_4 indicating the presence of a

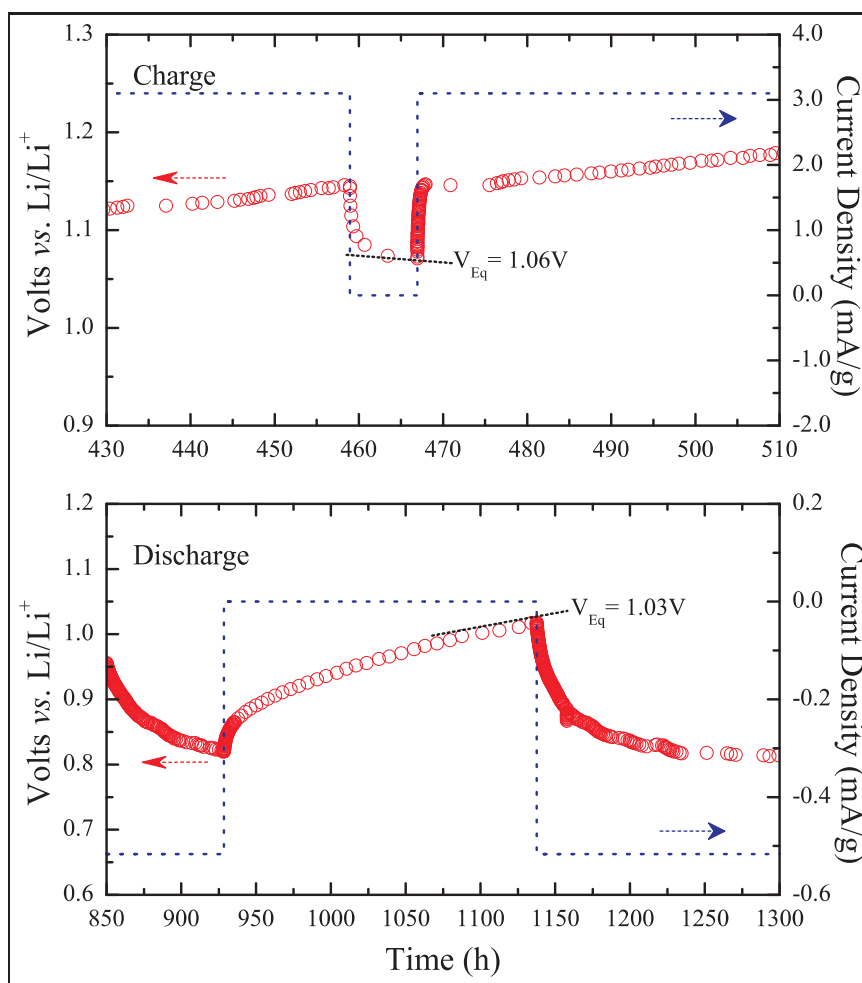


Figure 4.7: GITT profiles during charge and discharge for δ - MnP_4 at C/50.

strongly correlated system, with the Fermi level lying in the Mn-P anti-bonding e -type orbital.⁷ This suggests that a lithium removal from the this ternary phosphide most likely involves a two phase reaction, in accordance with the electrochemical results.

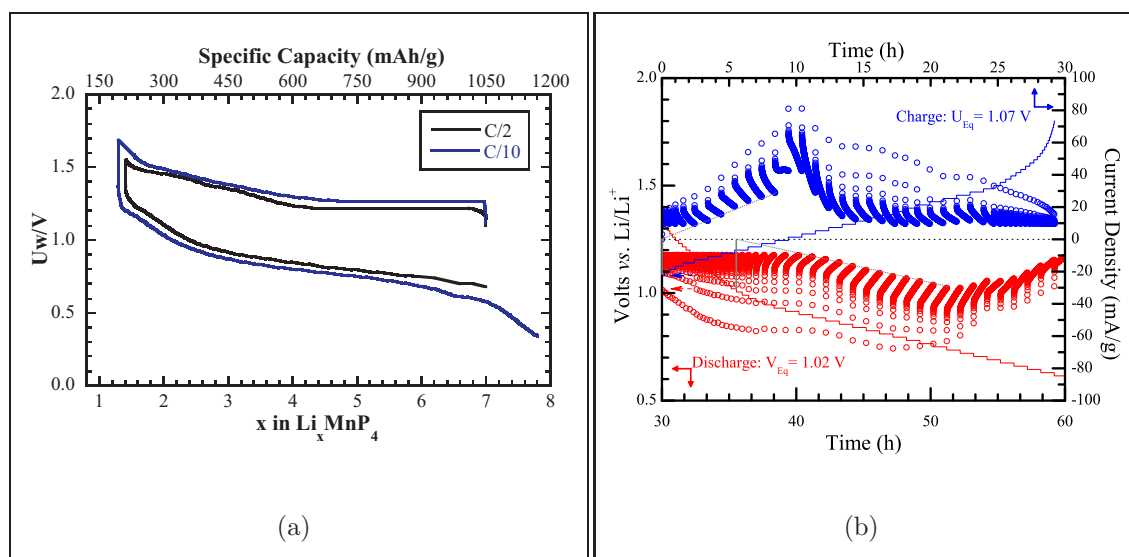


Figure 4.8: (a) Galvanostatic voltage-composition at different rates and (b) PITT profiles for Li_7MnP_4 .

Chronoamperometric Studies

The variation of the intercalation potential and the current response with time for the cycle of binary and ternary phases is shown on Figure 4.9. A bell-shaped current *vs* time curve is observed for the corresponding intercalation *plateau* at 0.62 V during the first discharge of MnP_4 but not in the subsequent cycle; Li_7MnP_4 exhibits the same behaviour under similar conditions. These results indicate the

occurrence of a phase transformation or decomposition process during the first cycle; in the subsequent cycles, the pattern is that of a monophasic process controlled by the diffusion of the Li^+ ions in and out the particles.^{8,9,9-11} Considering the large difference between the structures of the non-lithiated and lithiated forms of manganese phosphide, a phase transformation step upon cycling is in fact expected. It is not obvious, however, whether this phase process occurs only during the first discharge step, with partial reduction of manganese to form of a new structure, or by complete reduction to Mn^0 and Li_xP_y followed by a simple intercalation/de-intercalation process on subsequent cycles. Another possibility is that binary and ternary phases completely inter-convert upon cycling and, in this case, the transformation process could involve an intermediate phase. To investigate these hypotheses, the structure and morphology of cycled samples were analyzed (Section 4.3.3).

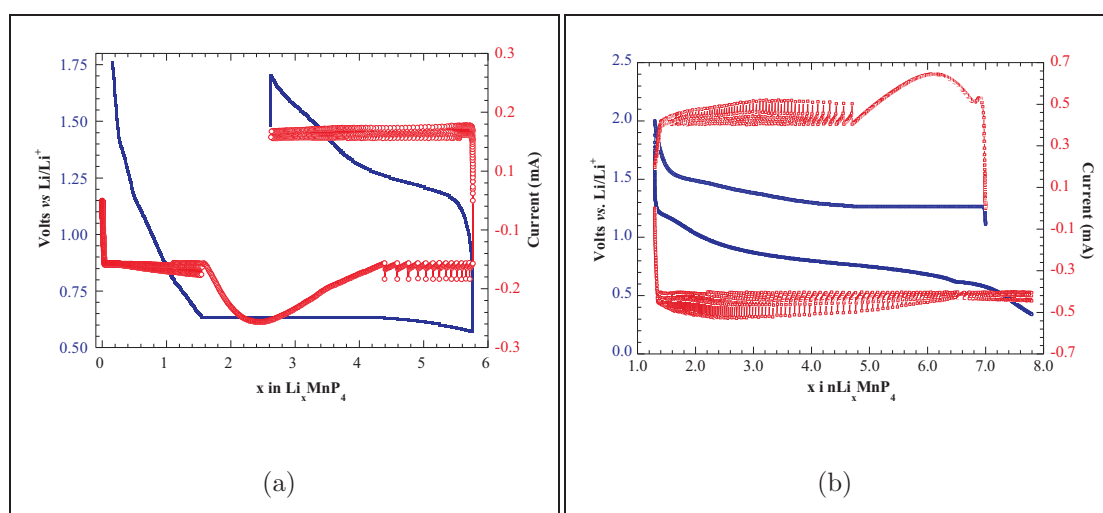


Figure 4.9: Chronoamperometric curves of (a) 8-MnP_4 and (b) $\text{Li}_7\text{MnP}_4\text{A}$.

Electrode Cycleability

Although full capacity can be achieved in the first cycle for both lithiated and non-lithiated forms of manganese phosphides, the electrodes exhibited poor cycling performance even at low galvanic rates (Figure 4.10). For MnP_4 , Figure 4.10(a), the already small initial capacity was totally lost after 3 cycles at C/5. At C/10 the reversible capacity started at 720 mAh/g, equivalent to almost 70 % reversibility; it diminished to 350 mAh/g after 5 cycles and stayed at this level for up to 40 cycles. Although not extremely high, this reversible capacity is better than that observed for commercial carbon anodes and alternative materials such as alloys and oxides.¹²

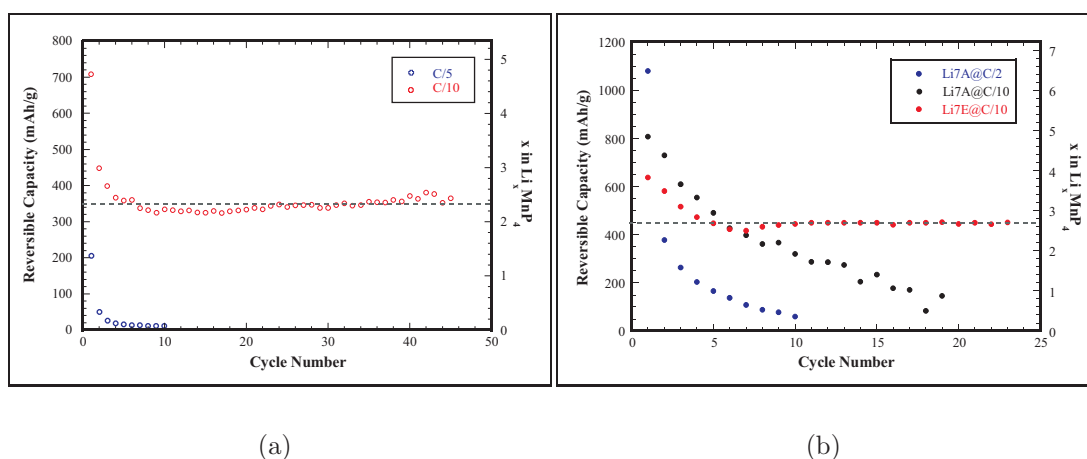


Figure 4.10: Cycling performance of $\delta\text{-MnP}_4$ and Li_7MnP_4 (samples **A** and **E**) electrodes at different rates.

The rate dependence of cycling performance was also observed when starting with Li_7MnP_4 . The material showed some capacity at the C/2 fast rate and about the same initial capacity as the non lithiated sample at C/10. Nevertheless, an even more

dramatic capacity fading is observed at C/10 rate, as depicted in Figure 4.10(b). In an attempt to improve the electrochemical performance, samples of Li_7MnP_4 were ball-milled under different conditions (see page 108). Figure 4.11 shows that the reduction of particle size and introduction of defects in the structure causes a significant reduction in the length of the intercalation plateau. Although not direct correlation can be made between the estimated particle sizes and the electrochemical behaviour, it is clear that smaller particle sizes leads to an increase in the amount of lithium extracted and uptaken on the first cycle, especially for sample **Li7D** (Figure 4.11(c)), due to the reduction in the diffusion path length, which in turn facilitates the phase transformation process. Moreover, **Li7E** exhibited very good cycling performance maintaining 70 % of its initial reversible capacity after 23 cycles (Figure 4.10(b)).

4.3.3 *Ex-situ* Analysis of Cycled MnP_4 and Li_7MnP_4

X-Ray Diffraction

Figure 4.12(top) shows the *ex-situ* XRD patterns of the samples obtained at different stages of cycling. For the cells assembled with the non-lithiated phase the patterns reveal the formation of Li_7MnP_4 at the end of discharge and total disappearance of the lines relative to the MnP_4 phase. On the other hand, MnP_4 is totally recovered after recharging to 1.7 V and no Li_7MnP_4 is detected at this point. The same results

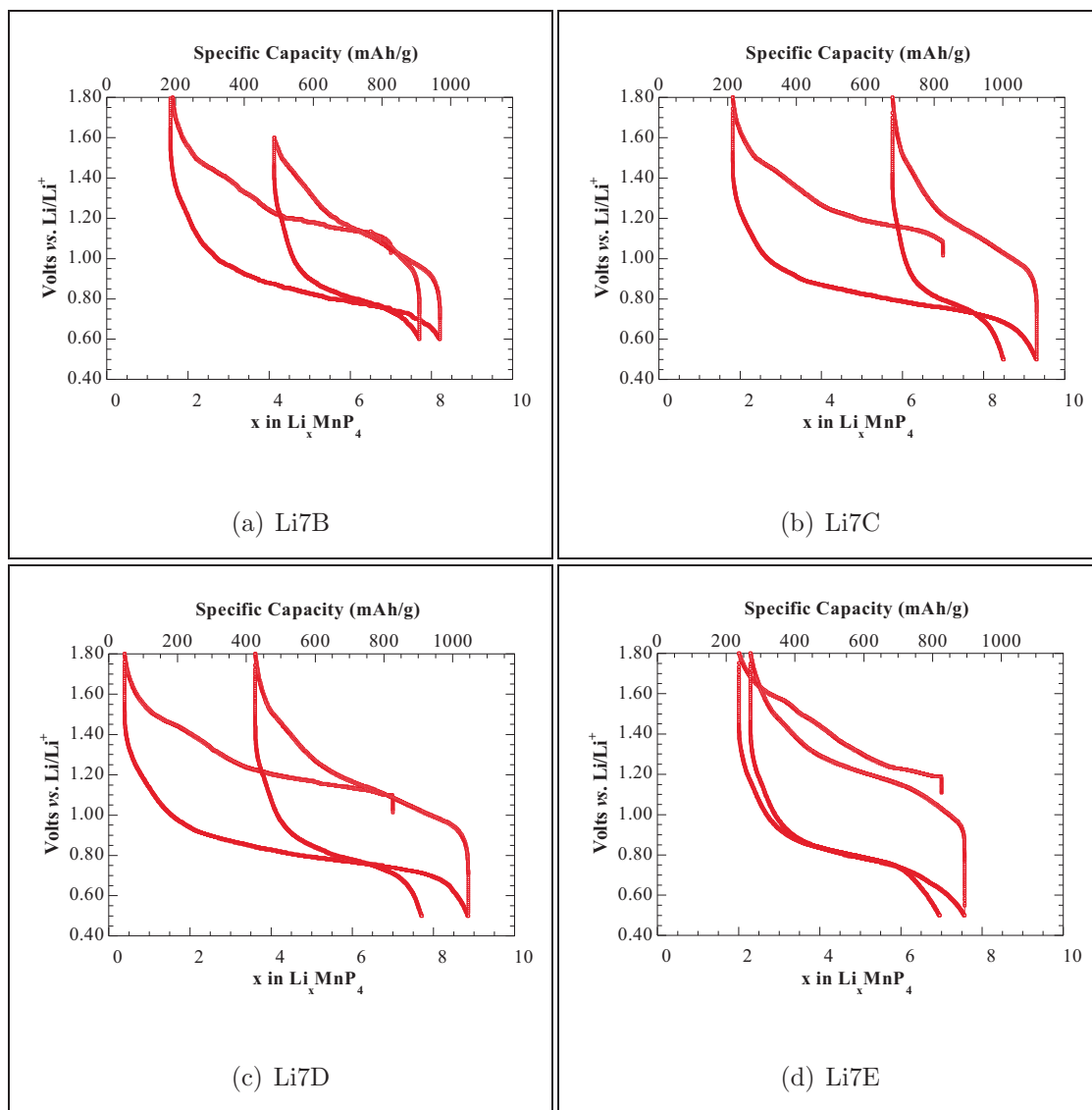


Figure 4.11: Cycling performance of Li_7MnP_4 samples at C/10.

are obtained after 5 and 10 cycles even though there is no evidence of a biphasic process in the chronoamperometric diagram.

The XRD pattern of charged Li_7MnP_4 electrodes displays significant loss of crystallinity (Figure 4.12(bottom)). The features that appear at $2\theta = 22.5, 24.0$ and 26.5° could not be indexed to lines belonging to any binary or ternary phase of the Li-Mn-P diagram. We suspect that they are related to some electrolyte decomposition material. More importantly, the lines relative to Li_7MnP_4 re-appear in the pattern of the discharged material, indicating reconstruction of the antiferroite phase. This type of reconstruction has been reported for the $\text{Li}_2\text{CuP}^{13}$ and Li_xMP_4 (M=Ti, V)^{14,15} systems. For Li_2CuP , the structure disorder upon oxidation was credited to the effect of electron density extraction from the uppermost band (which includes Cu and P bonding states) on the hexagonal Cu-P framework. In the titanium and vanadium system, the entropy gain associated with the formation of a Li- and P-disordered phase was put as the driving force for the reconstruction process. Based on theoretical calculations, Gillot *et.al.*⁷ suggested that the electrochemical extraction of lithium from Li_7MnP_4 yields a cubic phase of stoichiometry Li_5MnP_4 with smaller lattice parameter ($a_{\text{Li}_5}^{\text{calc}} = 5.778 \text{ \AA}$ vs. $a_{\text{Li}_7}^{\text{exp}} = 5.874 \text{ \AA}$). Contrary to their results, we did not detect lines relative to Li_3P ($2\theta = 31.0^\circ$ and 51.0°) in the XRD patterns obtained at any stage of cycling. Their results, however, were obtained at a deeper discharge stage ($V_{\text{window}} = 0.01 - 2 \text{ V}$); at this level of discharge, they suggested, the decomposition of the material into inactive Li_3P and Mn^0 disfavours reversibility.

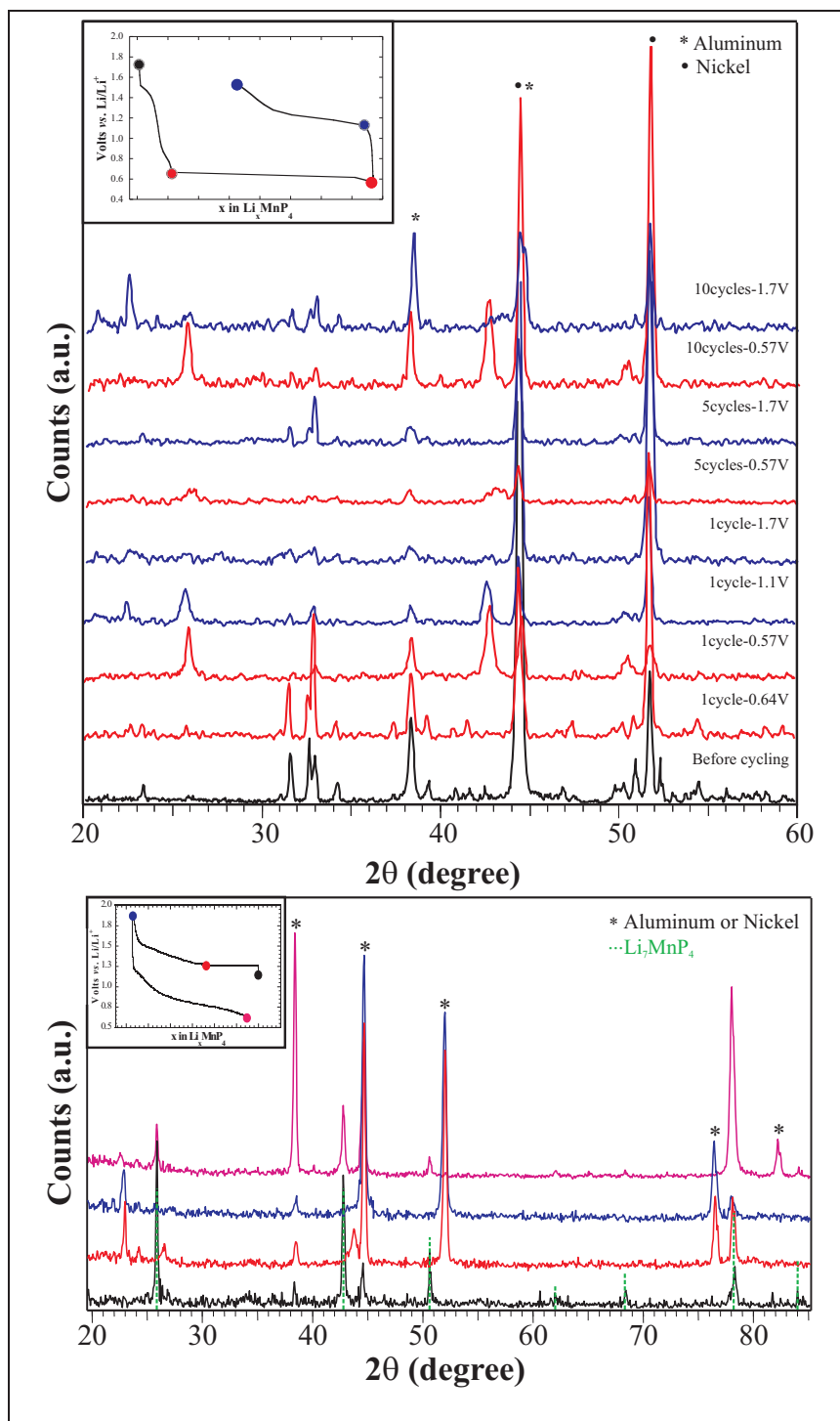


Figure 4.12: *Ex-situ* XRD patterns of (top) MnP_4 and (bottom) Li_7MnP_4 electrodes at different cycling stages.

Microscopy

The SEM micrographs of electrodes before and after cycling (Figure 4.13) confirm the pulverization of the particles upon lithium uptake and extraction. This can be attributed to the successive expansion and contraction of the unit cells of lithiated ($V_{Li_7MnP_4} = 213.5 \text{ \AA}$) and non-lithiated ($V_{s-MnP_4} = 1163.8 \text{ \AA}$) phases, which provokes the formation of cracks in the particles.¹⁶ Although the material is still available for phase transformation, the loss of physical contact between particles hinders the electron transport required for the redox process. Hence, part of the material becomes dormant and the obtained capacity is averaged over the total mass initially loaded in the cell. The global effect is a progressive decrease of the cell overall reversible capacity.

When the lithiated phase is initially loaded in the cell, the XRD pattern of the cycled electrodes becomes completely featureless upon charge (Figure 4.12), indicating amorphization of the phase. On subsequent discharge, the ternary phase re-crystallizes. Contrary to the electrochemical data, these results suggest that the mechanism for lithium uptake and/or extraction depends on the structure of the starting material. The magnitude of X-ray diffraction depends on long-range ordering of the atoms and the particle size limit is in the order of 100 nm.¹⁷ A comparison of the starting materials particle size reveals that the lithiated phase, even non-ball-milled, has smaller particles than the binary counterpart, in agreement with the duration

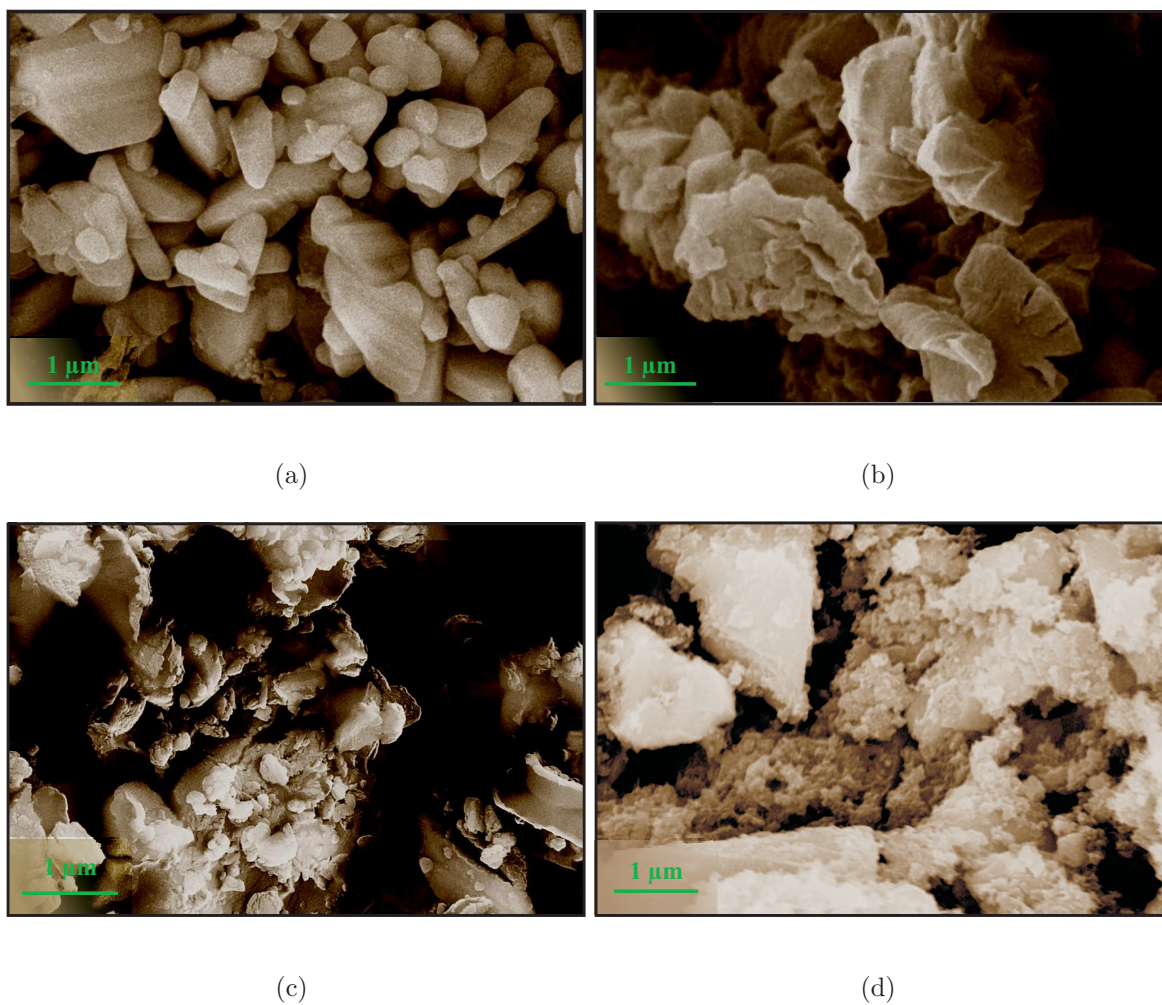
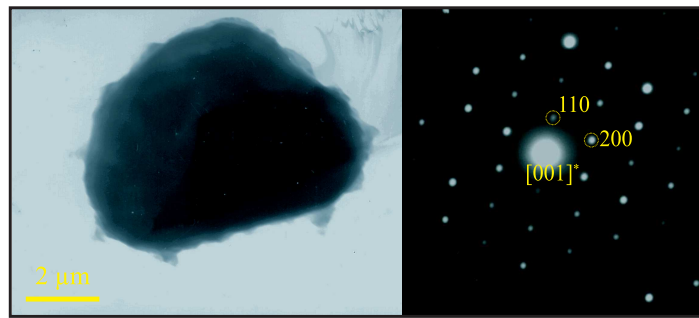


Figure 4.13: *Ex-situ* SEM microographies of (a) pristine and (b) cycled MnP_4 and of (c) pristine and (d) cycled Li_7MnP_4 electrodes.

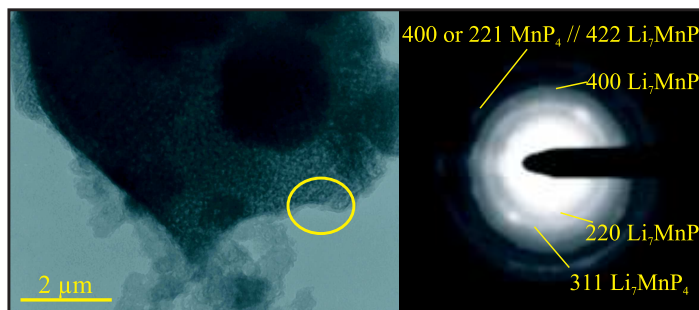
of heating, much shorter for the Li_7MnP_4 sample; crystal size of samples obtained by crystallization from the melt is directly proportional to the reaction duration.^{18,19} Additionally, manganese is randomly distributed in the antiferroite but not in the monoclinic structure; it is reasonable to expect that long-range order re-arrangement upon cycling is more feasible when starting with the non-lithiated phase. This is substantiated by TEM microscopy and SAED of the cycled electrodes (Figure 4.14) which reveal the formation of nano-crystallites upon cycling, even though the particles retain their global shape. A survey of the samples discharged to different stages displayed the presence of neither Mn^0 nor lithium phosphides (LiP or Li_3P). The SAED of the electrode material discharged up to 4Li^+ (Figure 4.14(b)) shows that the $[400]$ planes of $\delta\text{-MnP}_4$ have the same d -spacing as the $[422]$ planes in Li_7MnP_4 , suggesting that a phase transformation process may take place along these planes (see planes indicated by dotted lines in Figures 4.15(b) and 4.15(c)).

4.3.4 Proposed Mechanism for Phase Transformation

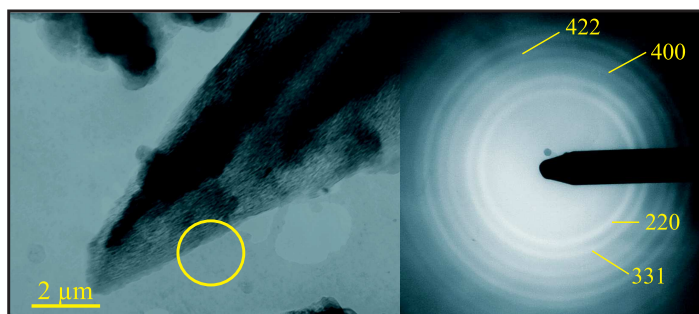
Based on the results discussed in the previous sections, a mechanism is proposed for this transformation which involves the breakage and reformation of P–P and Mn–P bonds (Figure 4.15).¹ Comparing the two structures, one can see that the Mn atom is regularly distributed in the MnP_4 structure, whereas in Li_7MnP_4 it statistically shares the tetrahedral sites with Li. Upon lithium uptake, in addition to P–P and Mn–P bonds being broken, manganese atoms must randomly shift from octahedral



(a)



(b)



(c)

Figure 4.14: *Ex-situ* TEM images and respective SAED δ - MnP_4 electrodes at different cycling stages: (a) pristine, (b) reduced to Li_4MnP_4 , and (c) fully discharged.

to tetrahedral sites. On oxidation, lithium is removed from the structure and the octahedral sites are re-occupied by manganese; however, a certain degree of site disorder is now introduced in the MnP_4 structure. This accounts for the increasing broadening of the XRD lines upon cycling observed for MnP_4 and explains the loss of capacity due to particle crumbling caused by the structural breakdown.

The proposed mechanism also provides an explanation for the disappearance of the features in the XRD patterns of lithiated samples upon oxidation. Given the random character of site occupancy in the antiferroite structure, it is reasonable to think that the formation of MnP_4 during the first oxidation of Li_7MnP_4 is a more difficult process compared to the reverse one, required for lithium uptake by MnP_4 . In the first case, the Li/Mn site ordering in the starting material is completely randomized and delithiation leads to the proper stoichiometric ratio of manganese and phosphorus but no long range ordering of the MnP_6 octahedra. This lack of periodicity does not favour the formation MnP_4 seeds necessary for the growth of the binary phase, so the resulting material is essentially amorphous. Subsequent reduction of the charged material reforms the antiferroite structure in which occupation of tetrahedral sites is disordered.

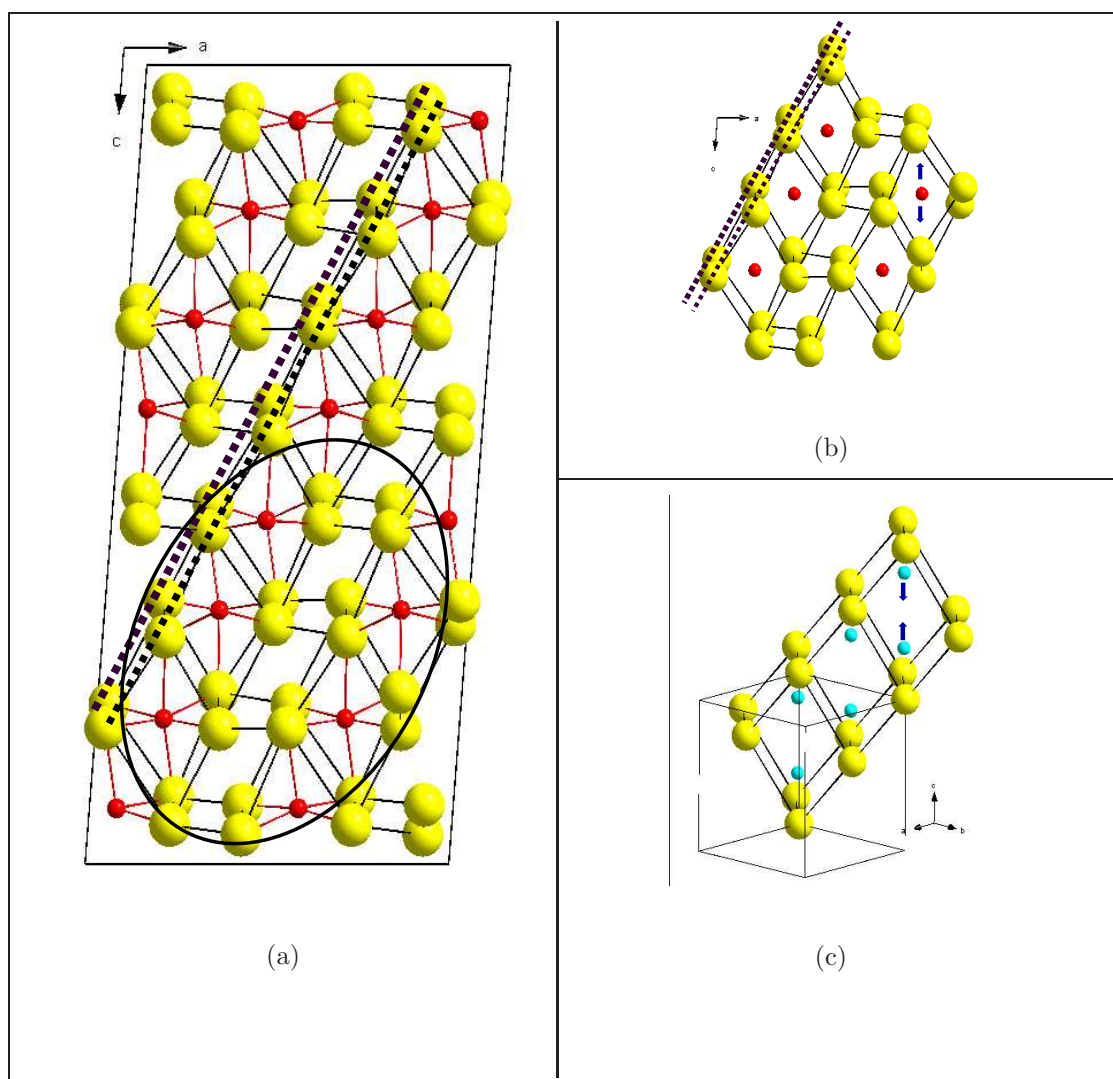


Figure 4.15: Schematic of the mechanism for phase transformation between MnP_4 and Li_7MnP_4 during electrochemical cycling: (a) structure of δ - MnP_4 , (b) zoom of portion indicated by the dotted circle in a, and (c) structure of Li_7MnP_4 . Yellow, red, and blue spheres correspond to P, Mn, and Mn/Li atoms, respectively.

4.4 Conclusions

This study shows that MnP_4 and Li_7MnP_4 have a similar behaviour toward electrochemical reaction with lithium. Whether starting with the lithiated or the non-lithiated phase, up to 3 Li^+ are reversibly uptaken/extracted yielding a specific capacity of 350 mAh/g during 40 charge/discharge cycles.

Despite the differences in the XRD patterns of the cycled electrodes prepared with lithiated and non-lithiated phases, the similar reaction potentials, voltage variation with compositional change, and current response to the application of potential steps in first sweep are evidence that the electrochemical reactions involve the same binary phase interconversion process mechanism.

The electrochemical data indicate that high intercalation rates contribute to the kinetics of the phase transformation. Furthermore, ball milling of the lithiated phase prior to preparation of the battery composite markedly improves the reversibility (Figure 4.11(d)) due to reduction of the path-length for diffusion of lithium ions.

4.4.1 Comparison of Results

Part of the results described here were published in *Science Magazine*.¹ It constituted the first report on the study of transition metal phosphides as anode material for Li-ion batteries. Since then, our research group and others have investigated different transition metal phosphides. Among these, Gillot and co-workers reported their

results on manganese phosphide systems.^{7,20} Their electrochemical data are very similar to ours, although their interpretation of the results differs sometimes:

- The *in-situ* XRD of the material discharged to 0.01 V revealed the presence of lines assigned to Li_3P , whereas metallic manganese nano-particles were detected by HRTEM, although the micrographs display strong contamination by the laser beam. These results imply that Li_7MnP_4 decomposes into Li_3P and Mn^0 at low potential. By avoiding this decomposition reaction (upon proper selection of the voltage window), however, better cycling performance was obtained. Nevertheless, the authors indicated that the redox mechanism for the remaining steps does not depend on this decomposition reaction but, although not showing any experimental data (XRD or TEM for example) after the first cycle, they claimed that “the ternary phase is not reformed from Li_3P and Mn^0 electrodes”.
- In agreement with our data and proposed mechanism, Gillot *et al.* identified the reversible reaction between Li_7MnP_4 and MnP_4 . Nonetheless, based on first-principles electronic structure calculations, the authors suggested that lithium removal occurs *via* a two-step reaction between Li_7MnP_4 and Li_5MnP_4 . The XRD results, however, gives no clear evidence of the formation of the Li_5MnP_4 phase other than an extremely slight shift of the Bragg angles of some lines.
- Based solely on values of incremental capacity at relatively high galvanic rates (1 Li/15 h), the authors suggested that “discharge and charge reactions involve

different mechanisms". The authors neglected, however, to determine the equilibrium values of voltage for the referred processes, which is shown here to be approximately the same whether starting the electrochemical process on charge or discharge (see Figure 4.7 on page 112, and Figure 4.8(b) on page 113).

Despite of some differences in interpretation, using molecular electronic structure calculations based on the extended Hückel tight-binding method (EHTB) Gillot and co-workers showed that, similar to other phosphides,^{13,21,22} the redox center involved in the $MnP_4 + 7Li$ reaction is primarily the phosphorus atoms.

References

- [1] Souza, D.; Pralong, V.; Jacobson, A.; Nazar, L. *Science* **2002**, *296*, 2012.
- [2] Massalski, T.; Okamoto, H.; Subramanian, P.; Kacprazak, L., Eds.; *Binary Alloy Phase Diagrams*; volume 1-3 Plenum Press: New York, 2nd ed.; 1990.
- [3] Jeitschko, W.; Donohue, P. *Acta Cryst.* **1975**, *B31*, 574-580.
- [4] Juza, R.; Bohmann, T. *Z. Anorg. Allg. Chem.* **1961**, *308*, 159-178.
- [5] Jeitschko, W.; Rühl, R.; Krieger, U.; Heiden, C. *Mater. Res. Bull.* **1980**, *15*, 1755-1762.
- [6] Rühl, R.; Jeitschko, W. *Acta Cryst.* **1981**, *B37*, 39-44.
- [7] Gillot, F.; Monconduit, L.; Doublet, M.-L. *Chem. Mat.* **2005**, *17*, 5817.
- [8] Weppner, W.; Huggins, R. *J. Electrochem. Soc.* **1977**, *124*, 1569.
- [9] Weppner, W.; Huggins, R. *J. Electrochem. Soc.* **1978**, *125*, 7.
- [10] Ho, C.; Raistrick, I.; Huggins, R. *J. Electrochem. Soc.* **1980**, *127*, 343.

- [11] Huggins, R. Mat. Res. Soc. Symp. Proc.. In *Solid States Ionics IV*, Vol. 369; MRS: Boston, 1995; Chapter Pulse Applications of Electrochemical Cells Containing Insertion Reacton Electrodes, page 3.
- [12] Tirado, J. L. *Mater. Sci. Eng. R: Reports* **2003**, *40*, 103-136.
- [13] Crosnier, O.; Mounsey, C.; Herle, P. S.; Taylor, N.; Nazar, L. F. *Chem. Mat.* **2003**, *15*, 4890.
- [14] Doublet, M.-L.; Lemoigno, F.; Gillot, F.; Monconduit, L. *Chem. Mat.* **2002**, *14*, 4126.
- [15] Bichatt, M.-P.; Politova, T.; Pfeiffer, H.; Tancret, F.; Monconduit, L.; Pascal, J.; Brousse, T.; Favier, F. *J. Power Sources* **2004**, *136*, 80.
- [16] Winter, M.; Besenhard, J. O.; Spahr, M.; Novak, P. *Adv. Mater.* **1998**, *10*, 725.
- [17] Klug, H.; Alexander, L. "X-Ray Diffraction Procedures for Polycrystalline and Amorphous Materials; John Wiley & Sons: New York, 2nd ed.; 1974.
- [18] Schäfer, H. *Chemical Transport Reactions*; Academic Press: New York, 1964 transl. by H. Frankfort.
- [19] Hagemuller, P., Ed.; *Preparative Methods in Solid State Chemistry*; Academic Press: New York, 1972.

- [20] Gillot, F.; Monconduit, L.; Morcrette, M.; Doublet, M.-L.; Dupont, L.; Tarrascon, J.-M. *Chem. Mat.* **2005**, *17*, 3627.
- [21] Pralong, V.; Souza, D.; Leung, K.; Nazar, L. F. *Electrochem. Comm.* **2002**, *4*, 516.
- [22] Crosnier, O.; Souza, D. C. S.; Greedan, J. E.; Nazar, L. F. Reversible Lithium Uptake by FeP₂. In *Material Research Society Symposium*; MRS: Boston, 2002.

Chapter 5

Iron Phosphide System

5.1 Introduction

Continuing the study of the electrochemical properties of transition metal phosphides in lithium-ion batteries, other 4th row elements were contemplated. Once again, the strategy adopted was to look for binary phosphides with somewhat open structures, but this time with focus on systems in which tertiary highly lithiated phases were unknown. Vanadium and chromium form phosphides with structures similar to that of manganese; the high phosphorus content binary phases exhibit the same stacking faulted structures and the ternary lithiated compounds tend to crystallize with the antiferite-type structure or in the tetragonal system.¹⁻³ Thus they were expected to present equivalent electrochemical properties. Indeed, VP_4 and Li_7VP_4

were extensively studied following our initial report on the manganese system and they show comparable electrochemical behaviour.^{4,5} Chromium phosphides are high pressure phases and even though the lithiated form can be easily prepared, assembly of a battery using charged material in the anode terminal is time consuming and detrimental for the shelf-life of the system, and therefore of little practical application.

The initial evaluation mapping was thus directed towards the opposite side of the periodic table. Nickel, copper and zinc are inert towards reaction with lithium and indeed, these metals are usually used as anode current collectors in lithium batteries. Based on the inertness criterion of the transition metal in the case of structure decomposition upon lithiation, phosphides of these metals would be excellent candidates. Indeed, CuP_2 ,⁶ Cu_3P ,^{7,8} Li_2CuP ,⁹ NiP_2 ,¹⁰ and Zn_3P_2 ,¹¹ have been recently investigated. Additionally, ternary zinc and nickel phosphides have been studied as anode or cathode materials, depending on the composition of the ternary phase, in both lithium-ion batteries and fuel cells.¹²⁻¹⁵

The immediate candidates, iron and cobalt phosphides, form open structures with two and three dimensional channels respectively.^{16,17} Lithiated ternary phosphide phases of cobalt are unknown and although LiFeP has already been synthesized, it is lithium poor, which does not seem to favour a phase transformation reaction like that observed in the manganese phosphide system.¹⁸ Furthermore, the metal-phosphorus bonds in the binary compounds exhibit a higher degree of covalency than the metal-oxygen linkage in the respective oxides. These facts allude to the possibility of lithium

uptake without much perturbation of the structure, perhaps *via* formation of a solid solution rather than through a binary phase transformation process.

Iron diphosphide crystallizes with a marcasite-type structure in the orthorhombic system, space group $Pmnn$ (Figure 5.1).^{19,20} Each Fe atom is surrounded by 6 phosphorus, forming corner-sharing octahedra. The atoms' arrangement allows for the formation of two dimensional channels along the c direction. A study of the electrochemical properties of FeP_2 as anode material for lithium-ion batteries and of the mechanism involved in the process is presented herein. The results on the synthesis, electrochemical performance, and structural changes are reported.

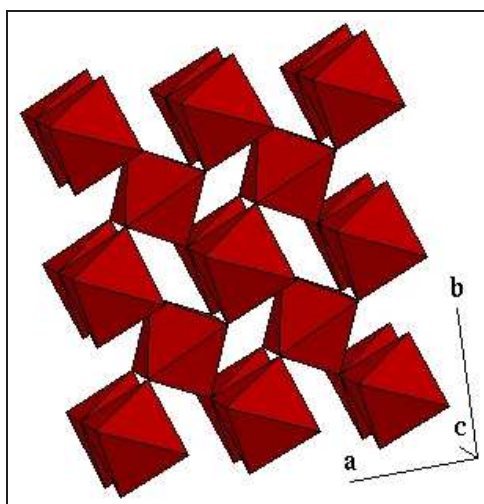


Figure 5.1: Polyhedral representation of the FeP_2 structure.

5.2 Experimental

5.2.1 Synthesis of FeP_2 Using a Flux of Tin

Iron, red phosphorus, and tin, in molar ratio of 1:10:40, were mixed inside an argon filled glove-box with the aid of a mortar and pestle and transferred to a quartz tube (18 mm OD x 16 mm D). The tube was evacuated, sealed (final length 200 mm), and then heated in a tube furnace at 700°C for one week. The reaction was quenched to room temperature and the resulting solid material was treated with at least three portions of 1:1 aqueous solution of hydrochloric acid. The black powder was manually crushed with the aid of mortar and pestle and sieved through a 400 mesh nylon grid.

5.2.2 Synthesis of FeP_2 Using Iodine Vapour Transport

Stoichiometric amounts of iron and red phosphorus were mixed with iodine with the aid of mortar and pestle inside an argon filled glove-box and transferred to a quartz tube (18 mm OD x 16 mm ID). The tube was evacuated, sealed (final length 200 mm), and heated at variable temperature and time; the reaction parameters are summarized in Table 5.1. At the end of the heating time, the tubes were quenched to room temperature and cut open. After thoroughly washing the product with acetone the resulting dark grey powder was manually ground with the aid of a mortar and pestle and sieved through a 400 mesh nylon grid. The purity of the final products

was estimated by XRD analysis.

Table 5.1: Reaction parameters for the preparation of FeP₂ by I₂ vapor transport.

Run	Amount of I ₂ (wt/wt%)	Temperature (°C)	Reaction Duration (h)
1	3	400	72
2	15	700	24
3	3	700	72
4	10	700	24
5	10	800	24

5.3 Characterization and Properties of FeP₂

5.3.1 Structure and Composition of the Materials

The slow diffusion of phosphorus inside the iron particles leads to a concentration gradient between the bulk and the surface. Consequently, direct synthesis of homogeneous FeP₂ from the pure elements demands a long reaction time and high temperatures. Based on the results with the manganese phosphide system, a flux of tin was used to obtain crystalline FeP₂ at lower temperature and shorter reaction times than previously reported.²⁰ The dark grey product was stable in air and its X-ray diffraction pattern is consistent with that expected for FeP₂. Accordingly, a molar

ratio P:Fe of 1.9, very close to the theoretical stoichiometric value 2.0, was obtained by chemical analysis of the material by ICP (Inductively Coupled Plasma). The XRD pattern (5.2) also shows no lines relative to metallic iron or other phosphides but the line at $2\theta = 31.5^\circ$ indicates the presence of Sn; elemental analysis revealed less than 0.5 % of the contaminant. Efforts to remove the residual tin by acid wash were unsuccessful, suggesting that it may be incorporated in the FeP_2 matrix.

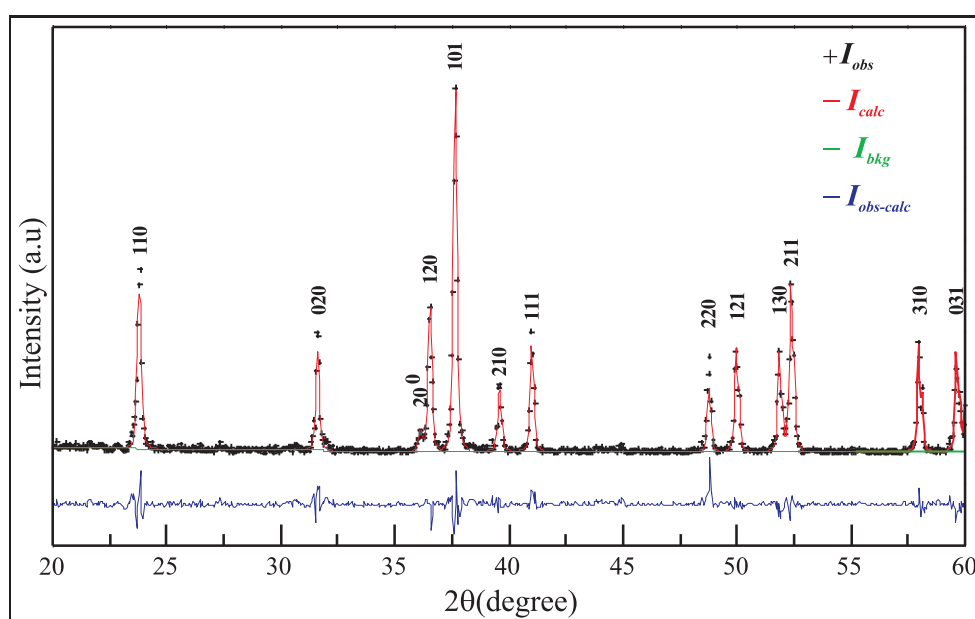


Figure 5.2: LeBail refinement of XRD pattern of FeP_2/Sn .

Although the desired iron phosphide phase was obtained using the tin flux technique, the method presented major drawbacks: (i) long time for reaction completion (at least 1 week), (ii) large amounts of tin required, (iii) difficulty to remove all the tin after the reaction, (iv) only small amounts of FeP_2 obtained. Vapour phase transport, on the other hand, proved to be a more efficient procedure.

The reaction mechanism²¹ proceeds by iron first reacting with iodine to produce a very volatile compound (FeI_3). The latter then reacts with phosphorus to form the iron phosphide. Compared to the tin flux process, in which the system is in the liquid state at the reaction temperature, here the reaction is carried out in the vapour phase, favoring its kinetics. Furthermore, the required amount of iodine is only 10 wt% of the total mass of FeP_2 , allowing the preparation of larger amounts of the desired product. The diffractograms of the products (Figure 5.3) reveal that pure FeP_2 is obtained under the conditions of Run 5 (Table 5.1); small amounts of two contaminants, namely FeP and FeP_4 , were present in the other samples. Hereafter, the two phases are labelled FeP_2/Sn and FeP_2/I_2 to denote the respective methods of preparation.

XRD data collected between $20^\circ < 2\theta < 60^\circ$, in steps of 0.01° during 10 s for FeP_2/I_2 and 0.05° for 10 s for FeP_2/Sn , were refined with GSAS^{22,23} in the tetragonal space group $Pmnn$ using the Rietveld method.²⁴ The refined variables were the scale factor, background polynomial coefficients, unit cell parameters, atomic positions, and pseudo-Voigt peak shape (using the type 2 profile function for constant wavelength diffraction data).²⁵ Figures 5.2 and 5.4 show the obtained full pattern match of the pure FeP_2 phases and the refined and calculated parameters for both samples along with the single crystal reference data are summarized in Table 5.2.

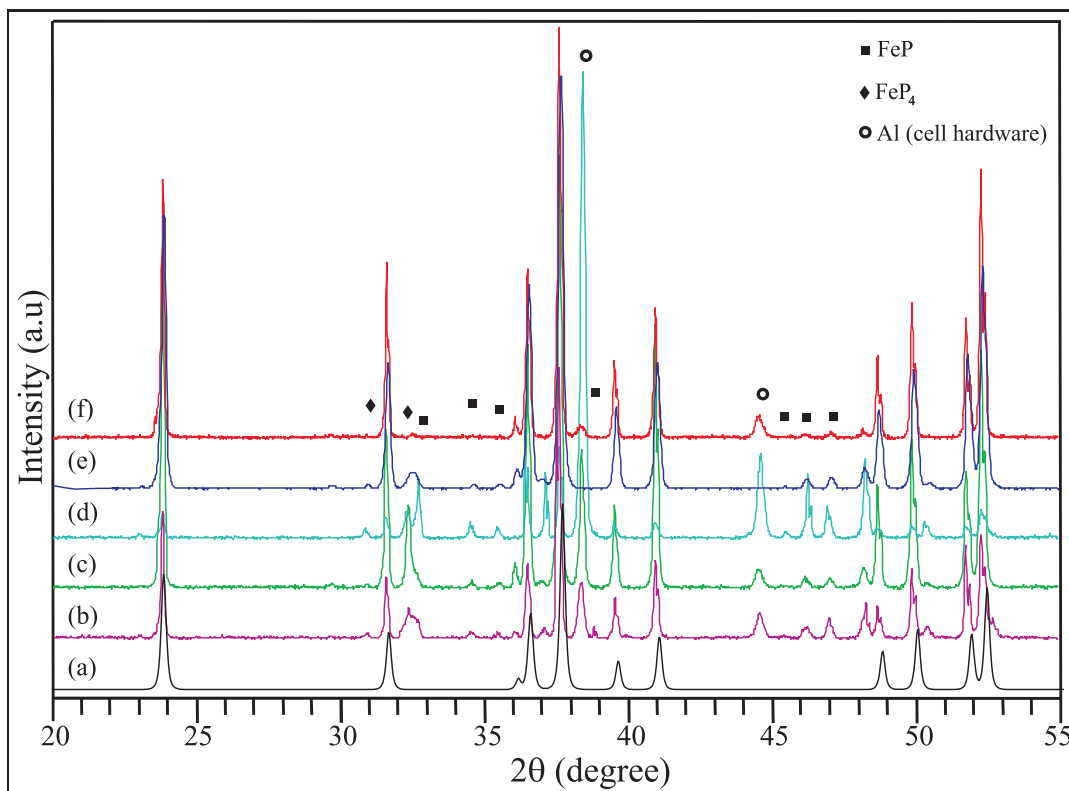


Figure 5.3: *Ex-situ* XRD patterns of FeP₂/I₂ samples obtained different reaction conditions: (a) Calculated theoretical pattern; (b) Run 1; (c) Run 2; (d) Run 3; (e) Run 4; (f) Run 5.

Table 5.2: Results of the LeBail fit for FeP₂ XRD data in the space group *Pmnn*.

Sample		FeP ₂ /Sn	FeP ₂ /I ₂	FeP ₂ ²⁰
Unit Cell Dimensions (Å)	a	4.9693±0.0030	4.9703±0.0005	4.9729±0.0007
	b	5.6532±0.0034	5.6538±0.0006	5.6568±0.0008
	c	2.7220±0.0016	2.7220±0.0003	2.7230±0.0004
Cell Volume (Å ³)		77.23	76.49	n.r. ^a .
Formula Weight		235.59	242.34	n.r.
Density (g/cm ³)		5.12	5.26	n.r.
R _p ^b (%)		18.81	8.29	n.r.
R _{wp} ^c (%)		27.00	11.54	n.a.
χ ²		1.45	2.71	n.r.
Number of Refined Variables		16	16	n.r.

^a n.r.= not reported

$$^b R_p = \frac{\sum ||I_{exp} - I_{calc}||}{\sum F_{exp}}$$

^c $R_{wp} = \sqrt{\frac{M_p}{\sum wI_{calc}^2}}$, where $M_p = \sum w(I_{obs} - I_{calc})^2$ is the powder data contribution for the general least squares minimization function.

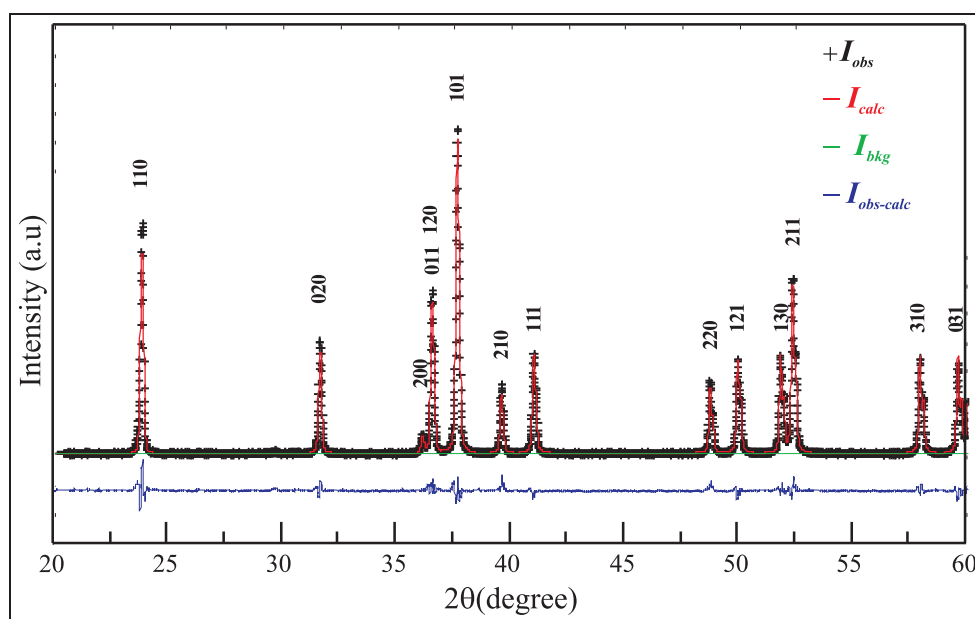


Figure 5.4: XRD profiles from full pattern matching of FeP_2/I_2 .

5.3.2 Electrochemical Studies of FeP_2

Figure 5.5 shows the potentiodynamic cycling performance of FeP_2 at a galvanic rate of $C/4$. The flat intercalation plateau at 0.25 V corresponding to the uptake of 6 Li^+ is associated with a bell-shaped current response, characteristic of a two-phase transition. Up to 5.5 Li^+ can be extracted from the structure corresponding to a reversible capacity of 1250 mAh/g (or 6350 mAh/cm³), more than three times that of the commercially used carbon. Hence, with an irreversible gravimetric capacity in the first cycle of only 8%, FeP_2 may constitute an excellent candidate for industrial applications. By comparison, the first cycle performance of CoO, which reacts with lithium to form Li_2O and Co, exhibits an irreversible component of up to 25%.²⁶ In

the same way, intermetallic compounds exemplified by FeSn_2 uptake lithium with the dissociation of the starting material into metallic Fe and Li/Sn alloys; partial reformation of FeSn_2 occurs on charge, leading to a specific capacity of 800 mAh/g and 20% irreversibility during the first cycle.²⁷

Long-term cycling of FeP_2 , however, causes a gradual loss of reversible capacity (Figure 5.5, **inset**). This may be caused by side reactions with the electrolyte at the low potentials employed, and/or structural changes within the material. Indeed, while the capacity of a cell is related to the structural or electronic behaviour of its electrodes, poor cell lifetimes are rooted mainly in side reactions occurring at the electrode-electrolyte interface and in the structural stability of the electrode materials.²⁸ Despite many years of research devoted to the mechanism by which the SEI forms on Li or carbonaceous materials, its composition and nature are still the subject of much controversy. The situation is even worse in the case of phosphide materials, since very few data are available. Preliminary tests with FeP_2 indicated that the electrochemical performance depends on the electrolyte composition and rate used. Therefore, investigation was needed about the effect of different electrolyte salts and solvents, and of the intercalation rate on the capacity loss, along with the mechanism for lithium uptake by the phosphide.

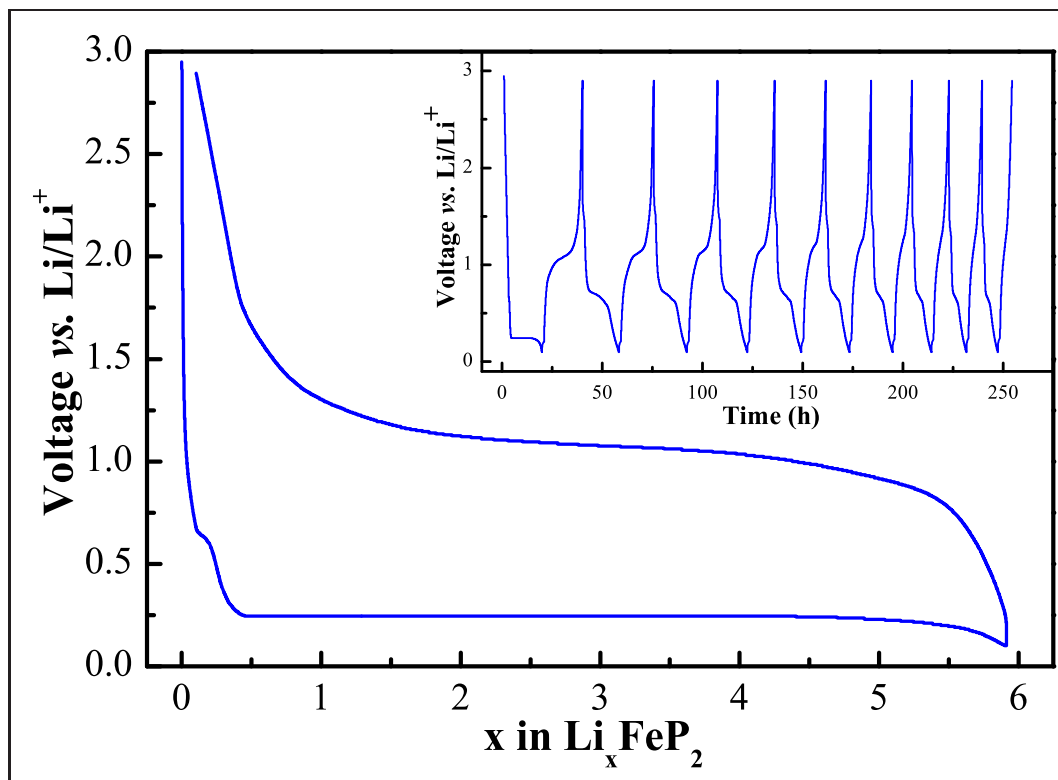


Figure 5.5: Voltage *vs* composition profile for first potentiodynamic cycle of FeP₂ at equivalent galvanic rate of C/4. **Inset** shows the efficiency performance for first 10 cycles.

Influence of the Electrolyte Composition and Cycling Rate

A two-levels/three-factors full factorial design of experiments (2^3 DOE) with one replicate per run was used to assess the effect of the electrolyte composition and cycling rate on the electrochemical performance of FeP_2 .^{29,30} The electrolytes used were 1 M solutions of the lithium salt, LiPF_6 (Hashimoto, 99.995 %) or LiBF_4 (Tommyama, 99.999 %), in a 1:1 mixture of battery grade (SelectipurTM, Merck) ethylene carbonate (EC) with either dimethylcarbonate (DMC) or diethylcarbonate (DEC). The applied galvanic rates were C/10 and 2C. Table 5.3 shows the runs of the experimental matrix (the variables with their normalized levels are presented in the bottom part). The properties (responses) selected from the electrochemical data were the amount of lithium uptaken in the first discharge (D1) and the reversible capacity of the first cycle (RC1).

The summary of the responses obtained for each run is presented in Table 5.4. Using standard least-squares parameter estimation procedures and statistical analysis, empirical models were built and parameter values and covariances were computed. All parameters were calculated based on a 95 % confidence level. The empirical models were developed sequentially starting with the main sources of variations, including the interaction factors when necessary, and only retaining the significant effects. The

Table 5.3: Matrix for the Factorial Design of Experiments.

Run	Salt	Solvent	Rate
1	-1	-1	-1
2	1	-1	-1
3	-1	1	-1
4	1	1	-1
5	-1	-1	1
6	1	-1	1
7	-1	1	1
8	1	1	1

Factor	Level	
Normalized Level	-1	+1
Salt (Sa)	LiPF ₆	LiBF ₄
Solvent (So)	EC:DMC	EC:DEC
Rate (R)	C/10	2C

models may be generically described by the equation:

$$\begin{aligned}
 P = & (A_1 \pm 2s_{A_1}) + (A_2 \pm 2s_{A_2})Sa + (A_3 \pm 2s_{A_3})So + (A_4 \pm 2s_{A_4})R \\
 & + (A_5 \pm 2s_{A_5})Sa * So + (A_6 \pm 2s_{A_6})Sa * R + (A_7 \pm 2s_{A_7})So * R
 \end{aligned}
 \tag{5.1}$$

where P = measured property, A = parameter that correlates a property with a variable or interaction between two variables and s_{A_n} = standard deviation of parameter A_n . Experimental and predicted data were compared through the F test and by analysis of the residuals.²⁹ The normal probability plots of the residuals as well as the plots of observed *vs* predicted values (Figure 5.6) confirm that the models provide an adequate description of the main sources of variation of the measured properties.

Table 5.4: Responses of the DOE for electrochemical performance of FeP₂.

Run	D1		RC1	
1	4.6	5.6	796	705
2	6.0	6.5	842	910
3	5.2	5.1	569	455
4	5.4	6.0	1001	1047
5	5.6	5.9	523	501
6	4.5	4.5	410	410
7	4.6	4.5	182	114
8	4.4	3.7	592	660

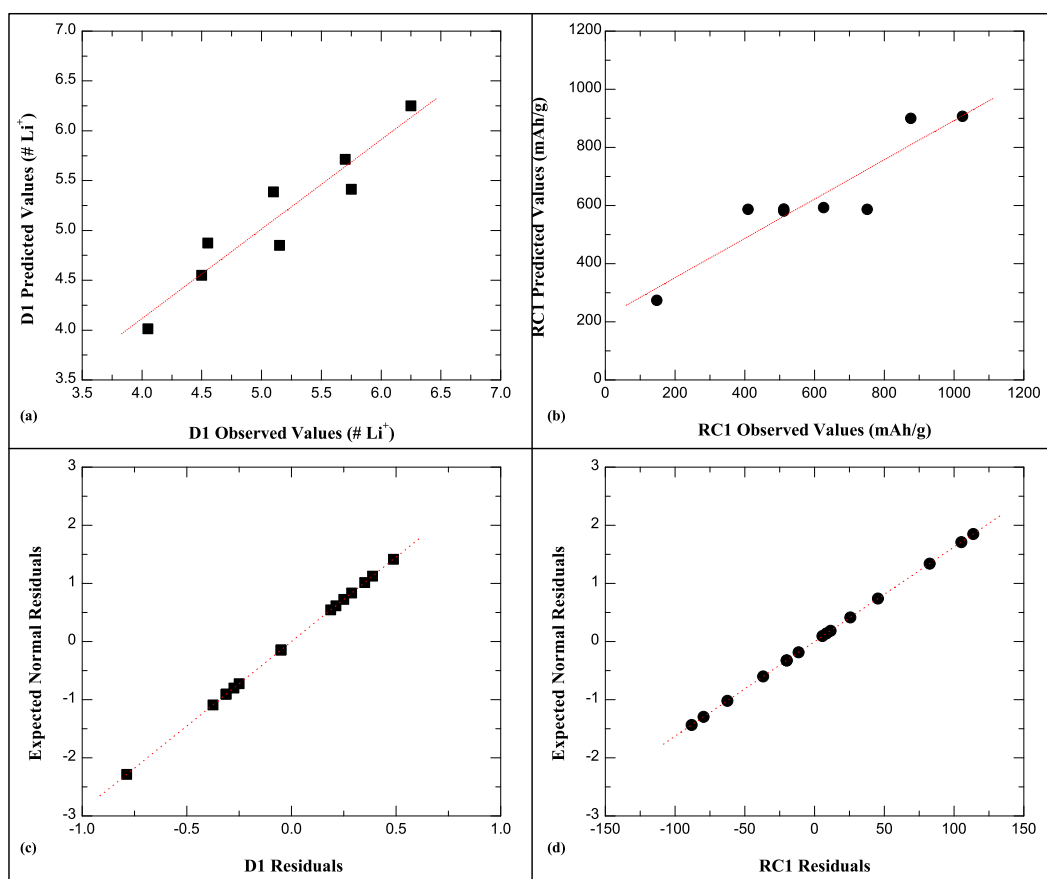


Figure 5.6: Adequacy of models obtained for the electrochemical performance of FeP₂ during the first cycle: (a-b) observed *vs.* predicted values and (c-d) normal probability distribution of the residuals.

Table 5.5 presents the models obtained for D1 and RC1 and the results of analysis of variance. The models account for 73 % and 93 % of the variability in the results of D1 and RC1, respectively. The analysis of variance shows that solvent, rate, and the interaction between salt and rate have significant effects on the amount of lithium uptake in the first discharge. According to the models, the combination of LiBF₄ in EC:DMC and lower galvanic rates favour both lithium uptake and reversible capacity during the first cycle.

5.3.3 *Ex-situ* Analysis of Cycled FeP₂

X-Ray Diffraction

Ex-situ XRD analysis of the cycled material revealed substantial loss of crystallinity after the two-phase transition. Compared to the crystalline pattern of FeP₂ (Figure 5.7a), only two very broad features appear in the XRD pattern of the discharged material (Figure 5.7b), along with small peaks ascribed to traces (< 5%) of residual FeP₂ that did not fully react.

Considering that the only ternary phase existent in the Li-Fe-P phase diagram is the lithium-poor LiFeP, a lithium intercalation reaction like that exhibited by MnP₄¹⁸ (which possesses many thermodynamically stable lithium rich ternary phases, including Li₇MnP₄) was not expected. In fact, not only does the amount of lithium electrochemically uptaken by FeP₂ not correspond to the stoichiometric ratio of

Table 5.5: Multiple regression and analysis of variance results for D1 and RC1.

$D1 = (5.13 \pm 0.10) - (0.37 \pm 0.10)S_o - (0.42 \pm 0.10)R - (0.43 \pm 0.10)S_a.R$ $r^2 = 0.7852$ Adjusted $r^2 = 0.7315$			
Analysis of Variance			
Source	Variance	F_o	F_c
<i>Model</i>	2.31	14.42	3.49
<i>So</i>	1.16	7.31	4.75
<i>R</i>	2.81	17.74	4.75
<i>Sa * R</i>	2.98	18.82	4.75
<i>Residuals</i>	0.1	-	-
$RC1 = (607 \pm 17) + (127 \pm 17)S_a - (183 \pm 17)R - (121 \pm 17)S_a.S_o$ $r^2 = 0.9445$ Adjusted $r^2 = 0.9306$			
Analysis of Variance			
Source	Variance	F_o	F_c
<i>Model</i>	342841	68	3.49
<i>Sa</i>	256298	51	4.75
<i>R</i>	538448	107	4.75
<i>Sa * So</i>	233777	46	4.75
<i>Residuals</i>	5037	-	-

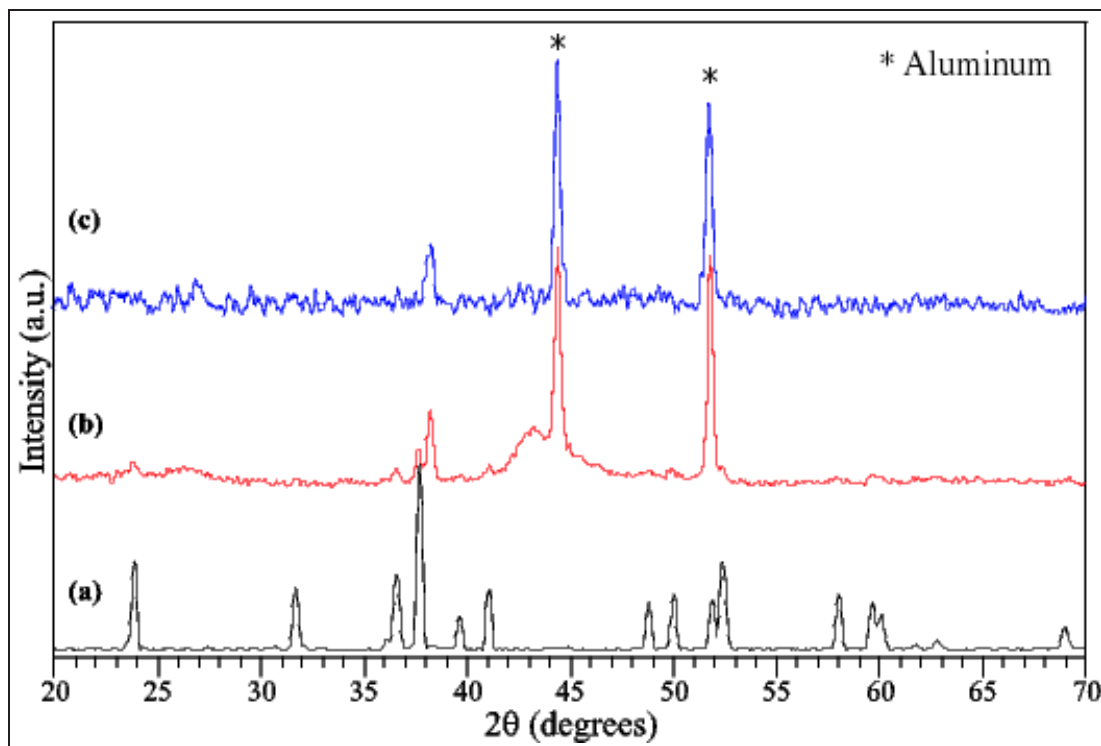


Figure 5.7: *Ex-situ* XRD patterns of FeP_2 electrodes at different cycling stages: (a) pristine material, (b) at 0.2 V on first discharge, and (c) at 1.1 V and on first charge.

the elements in LiFeP, but also the broad features present in XRD patterns of the discharged material do not match the d -spacing for the lines of the ternary phase. The positions of the reflections are closer to those exhibited by Li₃P and LiP,³¹ but the correspondence is poor, as many characteristic intense peaks of these phases are also missing. Additionally, no features relative to metallic iron are observed in the diffraction pattern, suggesting that simple decomposition of FeP₂ into Li₃P and bulk Fe particles does not explain the discharge process. The XRD pattern becomes completely featureless upon oxidation (Figure 5.7c) on subsequent cycling. Since XRD depends on the long range ordering of atoms, it does not constitute a useful tool for the study of the transformations occurring upon lithium uptake/extraction in the iron phosphide matrix. To further characterize this complex Li uptake process, XAS and Magnetic measurements were employed.

X-Ray Absorption Spectroscopy

The XANES spectra of the material before and after cycling are presented in Figure 5.8. Consistent with the loss of crystallinity observed in the XRD pattern, the intensity of the oscillations in the XAS spectra of the cycled materials were significantly reduced compared to those of FeP₂. The XANES portion of the spectra shows that the band edge of the FeP₂ (7118.2 eV) shifts by only 0.5–1 eV to lower energy after Li uptake. The edge energy is conversely raised on oxidation by only 0.2 eV. These are small changes compared to shifts higher than 4 eV observed in

the reduction of MoO_3 and other oxides upon Li uptake.^{32,33} Since the position of the absorption edge is correlated to the oxidation state of the element,^{34,35} it can be inferred that the “formal” oxidation state of iron in FeP_2 does not change appreciably on cycling. The general shape of the absorption edges in the spectra of the cycled FeP_2 samples, especially the discharged material, also differs strongly from that of bulk metallic iron, ruling out its formation upon lithiation.

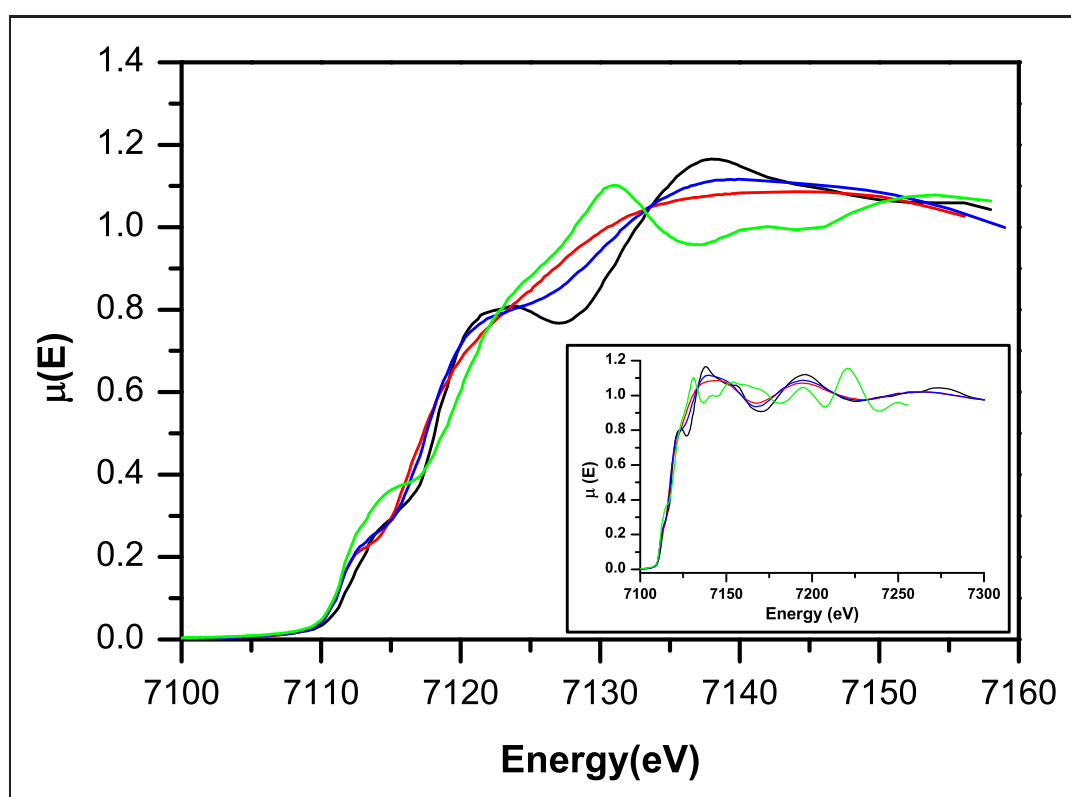


Figure 5.8: *Ex-situ* Fe K-edge XANES and **inset** EXAFS regions of the XAS spectra of FeP_2 samples: pristine (—), fully discharged (—), and fully charged (—); metallic Fe was used as reference (—).

The EXAFS area of the XAS experiment (Figure 5.8, **inset**) provides information

on the changes in the local coordination environment. The pseudo-radial distribution functions obtained from Fourier transformation of the EXAFS signals are shown in Figure 5.9. The RDFs of pristine and cycled FeP_2 show interesting differences. In pure FeP_2 , the fittings of the EXAFS spectra for the 1st and 2nd coordination shells of iron yield 6 P atoms at 2.25 Å and 1.6 Fe at 2.71 Å (Table 5.6). These values fully agree with the average values of the distances Fe-P (2.26 Å) and Fe-Fe (2.72 Å) obtained from crystallography data. After the uptake of 6 Li, the intensity of these Fe-P interactions suffers significant reduction but does not disappear completely. The number of phosphorus neighbours (4.6) is maintained in the first Fe-P shell at about the same distance (2.29 Å) relative to the starting material. The rather low coordination number for an expected octahedral environment is probably due to a significant distribution in the Fe-P distances. Long range order, however, is destroyed by Li uptake. The lack of features at higher distances also proves that the existing Fe-P interactions cannot result from traces of residual unreacted FeP_2 , for in that case the intensity of the entire RDF would be attenuated. In addition, the first or second shells cannot be fit with Fe-Fe interactions, which indicates once again that bulk metallic iron is not formed.

The pseudo-RDF of the charged material shows that changes occur in the local environment vis-a-vis the reduced sample. It shows a modest increase in the number of Fe-P nearest neighbours, although the inaccuracy of the EXAFS method in determining coordination numbers in disordered materials makes it difficult to

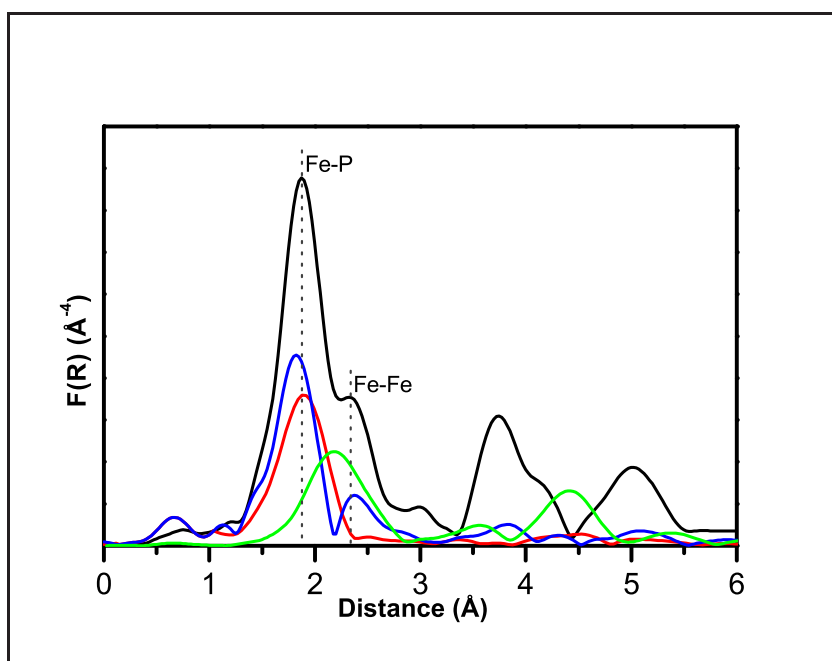


Figure 5.9: Pseudo-radial distribution functions derived from the *ex-situ* EXAFS signals) of FeP_2 samples: pristine (—), fully discharged (—), and fully charged (—); metallic Fe was used as reference (—).

precisely quantify the changes. More importantly, some of the long-range features that occur at distances $>4 \text{ \AA}$ in FeP_2 reappears in the spectrum of the charged material. An increase in both the Fe-Fe and the long-range interactions at 4.5 \AA and 6.1 \AA shows that a more ordered environment is reassembled, despite the overall long-range amorphous character of the structure.

Table 5.6: Summary of EXAFS data at the Fe K-edge for the first shell of FeP_2 .

Material	Neighbour	N^a	$R(\text{\AA})^a$	$\sigma^2(\text{\AA}^2)^a$	$\Delta E_o(\text{eV})^a$	$R_e(\%)^b$
FeP_2 Crystal	P	6	2.26	-	-	-
	Fe	2	2.72	-	-	-
FeP_2 Pristine	P	6.0	2.25	0.0032	1.34	7.00
	Fe	1.6	2.71	0.0023	-	-
FeP_2 Discharged	P	4.6	2.29	0.0080	2.13	16.44
	Fe	0	-	-	-	-
FeP_2 Charged	P	4.7	2.25	0.0064	0.41	12.73
	Fe	2.0	2.68	0.01	-	-

^a N , R , σ^2 , and ΔE_o are the fitted values of the number of surrounding atoms, their distance from absorbing Fe, the Debye-Waller factor and the energy shift, respectively.

$$^b R_e = \frac{\sum_{i=1}^N |y_{exp}(i) - y_{theo}(i)|}{\sum_{i=1}^N |y_{exp}(i)|}$$

Magnetic Measurements

Magnetization

The magnetic properties of the newly formed particles were investigated to provide some insight on the nature and structure of the phases formed by the electrochemical lithiation/delithiation processes. The data sets obtained for pristine and cycled materials were analyzed using Curie-Weiss (χ vs. T) and Langevin (M vs. M) type functions,³⁶ corrected for temperature-independent magnetic susceptibility and paramagnetic contributions respectively:

Curie-Weiss Equation for Magnetic Susceptibility

$$\chi_{\text{exp}} = \frac{C}{T - \theta} + \chi_{\text{T}} \quad (5.2)$$

where χ_{exp} is the experimental mass magnetic susceptibility ($=M/H$), C and θ are the Curie and Weiss constants respectively, χ_{T} is the temperature independent susceptibility ($=\chi_{\text{Diamagnetic}} + \chi_{\text{Pauli}}$), and T is the absolute temperature.

Langevin Equation for Magnetization

$$M = M_s \left(\coth \frac{\mu H}{kT} + \frac{kT}{\mu H} \right) + \chi_P H \quad (5.3)$$

where M is the experimental mass magnetization, M_s the saturation magnetization, μ the magnetic moment, k the Boltzmann constant, T the absolute temperature, χ_P the mass paramagnetic susceptibility, and H the applied field.

Pristine FeP₂ exhibited mostly diamagnetic behaviour with a small, weakly

temperature-dependent paramagnetic contribution (Figure 5.10), in agreement with previous reports.³⁷ The Curie-Weiss law of paramagnetism accounts for the

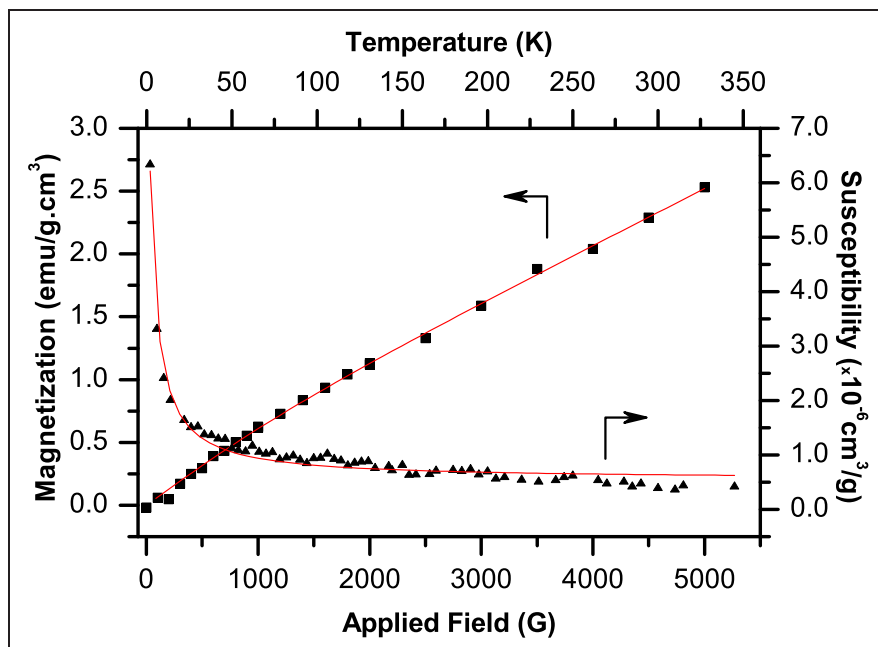


Figure 5.10: Field-dependent magnetization and temperature-dependent susceptibility curves for pristine FeP₂.

interaction between the elementary magnetic moments within a sample. The constant θ is a measure of the strength of interaction among the individual carriers of magnetic moment and is given by the relation $\theta = \gamma\rho C$, where γ is the atomic (or molecular) field constant and ρ is the density of the material. The Weiss constant (or Curie point) obtained for the pristine FeP₂, $\theta = -2.69 \pm 0.32$ (Table 5.7), reveals the presence of only extremely small anti-ferromagnetic interactions. Furthermore, the Curie constant determined from mass susceptibility results is related to the effective magnetic moment of the material, μ_{eff} , which in turn depends on the saturation

magnetization and the total angular momentum related to the quantum number $J = L + S$. In the case of crystalline materials, there is no significant contribution of the orbital momentum (L); therefore, only the spin contributes to the resulting magnetic moment of the specimen, and $J = S = 1/2$.³⁶ The Curie constant is given by:

$$C = \frac{N_A \mu_{eff}^2}{3M_w k} \quad (5.4)$$

$$= \frac{\mu_H M_s (S + 1)}{3kS} \quad (5.4')$$

$$= \frac{N_A g^2 S(S + 1) \mu_B^2}{3M_w k} \quad (5.4'')$$

with N_A the Avogadro number, M_w the molecular (or formula) weight, μ_B the Bohr magneton, k the Boltzman constant, and g the spectroscopic splitting factor which has a value of 1 for orbital and 2 for each spin motion. The Curie constant calculated for each spin is then $C_{spin} = 0.375 \text{ cm}^3 \text{ K/mol}$. Considering the experimental value of C_{exp} obtained for the starting material, the total number of spins present can be determined as $C_{exp}/C_{spin} = 0.9\%$ per unit formula of FeP_2 . This result, together with the small value of θ , attests for the quality of synthesis of polycrystalline sample of FeP_2 since the Curie-Weiss paramagnetic component is essentially negligible.

The ZFC-FC magnetization profiles for pristine and cycled materials (Figure 5.11) show a significant increase in magnetization upon lithiation. After Li uptake, the magnetic susceptibility increases by a factor of $\approx 10^2$ over the temperature range of 2 K to 350 K and a strong temperature dependence develops (Figure 5.12).

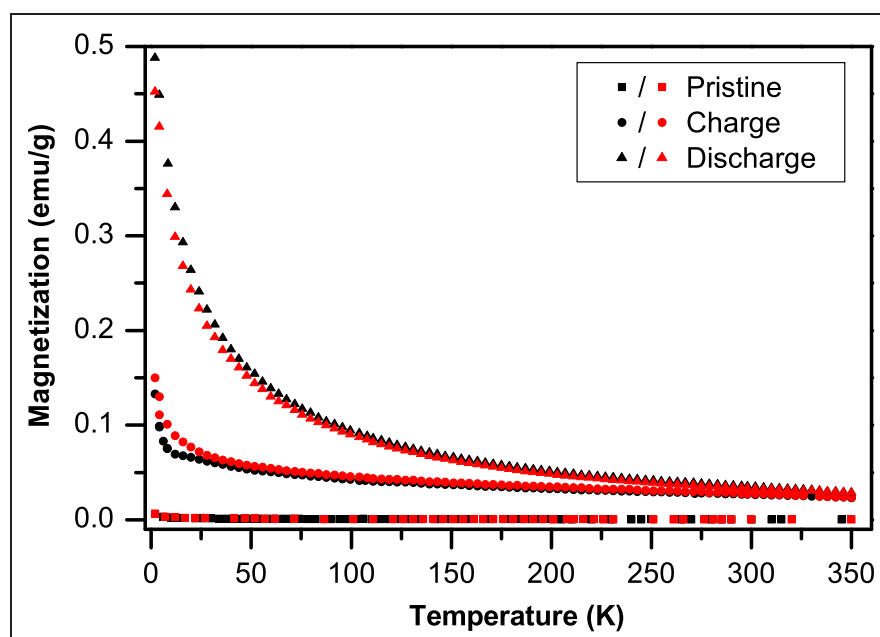


Figure 5.11: Temperature dependence of magnetization in the ZFC and FC modes (black and red symbols respectively) of FeP_2 before and after cycling.

This behaviour is consistent with magnetism due to the presence of very small ferromagnetic particles, *i.e.* super-paramagnetism.³⁸ If a material composed of very small crystallites (1 - 10 nm) is at temperatures below the Curie temperature, although the thermal energy is not sufficient to overcome the coupling forces between neighbouring atoms, it can change the direction of magnetization of the entire crystallite. The resulting fluctuations in the direction of magnetization cause the magnetic field to average to zero. The material thus behaves similarly to a paramagnet, except that instead of each individual atom being independently influenced by an external magnetic field, the magnetic moment of the entire crystallite tends to align with the magnetic field.

No obvious blocking temperature was detected over the range of temperature studied, which suggests that the lithiated material may have a high blocking temperature and/or that there is a wide size distribution of magnetic domains.^{39,40} Nevertheless, treatment of the M vs. H data with a Langevin-type function (valid for super-paramagnetic particles when the magnetic assembly is formed by small particles of the same size and with no anisotropy)³⁹ leads to excellent correlation coefficient (Table 5.7). Hence, the material formed upon lithiation must have a blocking temperature above 350 K.

On charge, the super-paramagnetic component of the magnetization curve is strongly reduced. Since the electrochemical lithium uptake process is not completely reversible, the remaining paramagnetic signal is most likely due to a small inactive fraction of the material that has irreversibly reacted during lithium insertion. The magnetization *vs.* field data presented in Figure 5.13 shows that data collected at 350 K and 100 K is still typical of super-paramagnetic behaviour with no hysteresis; a very weak remanent moment (7.9×10^{-3} emu/g) appears at 2 K. For both discharged and charged states it is impossible, however, to distinguish between the formation of nanoscopic Fe, or Fe_xP ($x= 1, 2, 3$) as these are all magnetic materials that would exhibit properties different from their bulk behaviour.⁴¹

The magnetic moment is related to the size of the magnetic domains by the

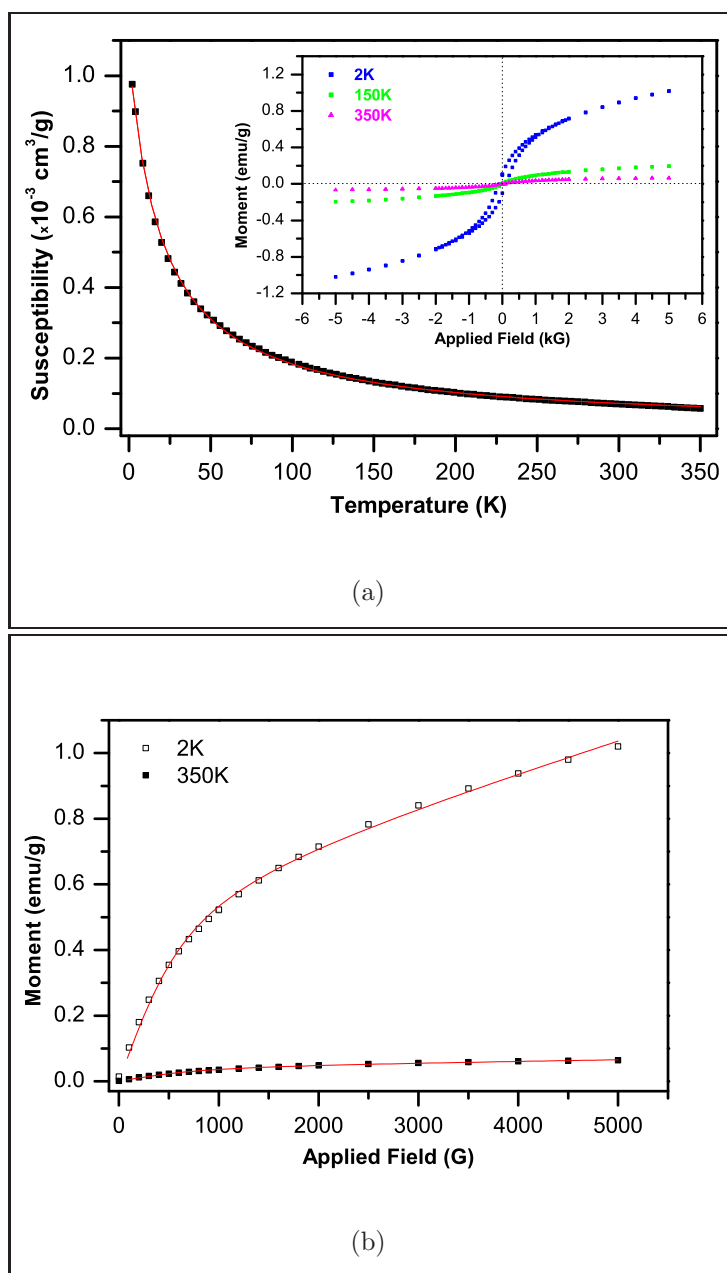


Figure 5.12: Magnetization curves of discharged FeP_2 : (a) temperature dependence of mass susceptibility at $H= 500$ G (**inset:** hysteresis loops at 2 K, 100 K, and 350 K) and (b) Langevin fit of M vs. H curves at 2 and 350 K.

Table 5.7: Results of Curie-Weiss and Langevin fitting of FeP₂ magnetization data.

Function	Parameters	Pristine	Discharge	Charge	
Curie-Weiss	H _a , G	1000	500	500	
	C, cm ³ K/g	(3.02±0.16)×10 ⁻⁵	(2.14±0.01)×10 ⁻²	(3.24±0.38)×10 ⁻³	
	θ, K	-2.69±0.32	-20.25±0.19	-19.19±1.68	
	χ _T , cm ³ /g	(5.50±0.25)×10 ⁻⁷	(4.98±0.95)×10 ⁻⁶	(5.00±0.25)×10 ⁻⁵	
	R ²	0.9752	0.9995	0.9646	
Langevin	T= 2K	M _s , emu/g	(3.30±0.83)×10 ⁻³	(6.01±0.16)×10 ⁻¹	(1.22±0.03)×10 ⁻¹
		μ, emu/g cm ³	(4.89±1.19)×10 ⁻¹⁹	(1.02±0.05)×10 ⁻¹⁸	(4.42±0.12)×10 ⁻¹⁹
		χ _P , cm ³ /g	(4.45±0.16)×10 ⁻⁶	(9.36±0.38)×10 ⁻⁵	(3.00±0.06)×10 ⁻⁵
		R ²	0.9989	0.9984	0.9998
	T= 350K	M _s , emu/g	-	(4.69±0.16)×10 ⁻²	(2.32±0.03)×10 ⁻²
		μ, emu/g cm ³	-	(1.49±0.07)×10 ⁻¹⁶	(8.68±0.19)×10 ⁻¹⁹
		χ _P , cm ³ /g	-	(4.38±0.36)×10 ⁻⁶	(1.97±0.07)×10 ⁻⁶
		R ²	-	0.9975	0.9995

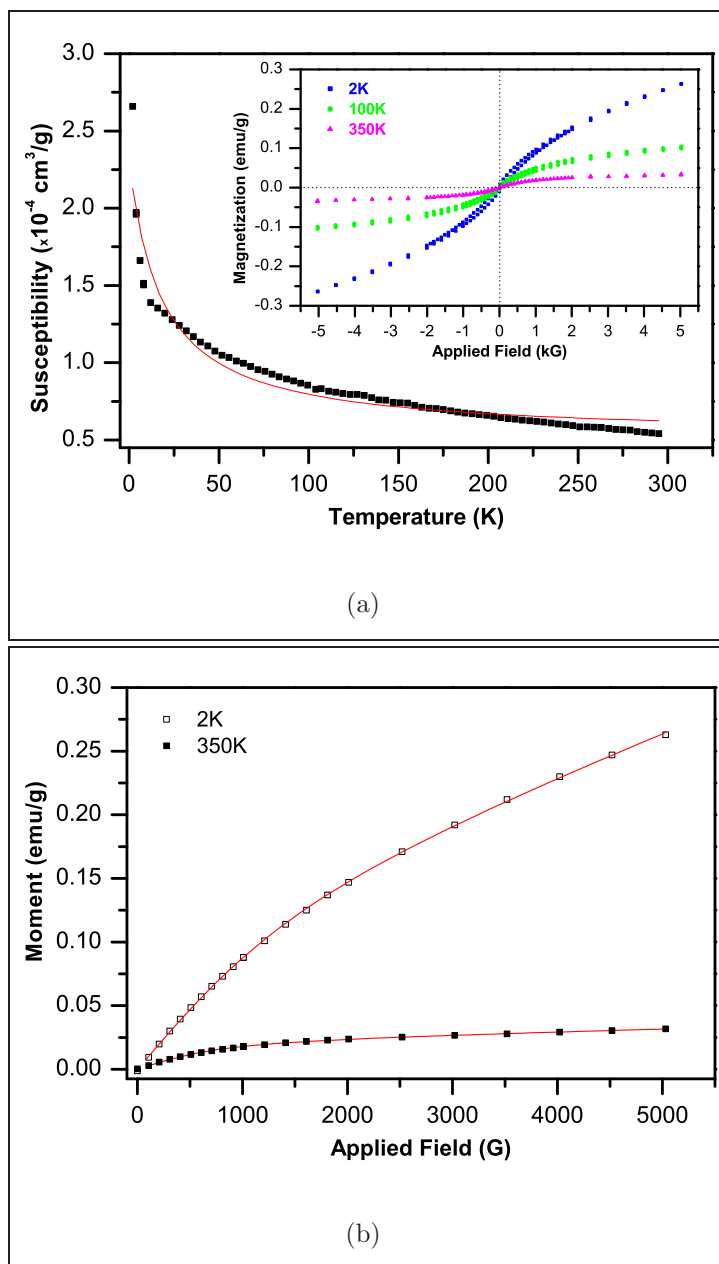


Figure 5.13: Magnetization curves of charged FeP₂: (a) temperature dependence of mass susceptibility at H= 500 G (**inset:** hysteresis loops at 2 K, 100 K, and 350 K) and (b) Langevin fit of M vs. H curves at 2 and 350 K.

equation:

$$\mu = \frac{\pi M_s D_p^3}{6} \quad (5.5)$$

where D_p is the diameter of the magnetic domain.^{38,42} The size of the magnetic domains calculated for pristine, discharged, and charged FeP₂ are given in Table 5.8.

At 2 K the thermal effects which tend to randomize the direction of magnetic moment

Table 5.8: Magnetic particle diameter calculated for FeP₂ samples.

Sample		Pristine	Discharge	Charge
Particle	T=2 K	66	15	19
Diameter, nm	T=350 K	-	182	232

vectors, and consequently interactions among the domains, are minimized. The calculated domain sizes for the cycled materials are therefore very close to the particle sizes of the newly formed phases.⁴³ Upon lithiation, a four-fold decrease in particle size is observed, consistent with the strong amorphization effect observed in the XRD patterns. The small increase in the magnetic domain size after lithium removal is probably due to the short-range reorganization of the FeP₂ structure that has been observed in the EXAFS study.

Mössbauer Spectroscopy

The spectrum of pure FeP₂ (Figure 5.14) displays a doublet with signals positioned at -0.905 and 1.081 mm/s. After lithiation, the contribution of this doublet is reduced

to less than 10 % of the total area under the curve; yet, two other signals appear at -0.016 and 0.657 mm/s. On charge, the two external peaks vanish completely and the internal peaks are slightly shifted to -0.014 and 0.626 mm/s.

To determine the exact parameters of the peaks present in the spectra, the experimental data sets were analyzed by least-squares fitting to the Lorentzian-Parabola⁴⁴ type function:

$$Y = \sum_{i=1}^n \frac{A_i}{1 + \frac{(x-p_i)^2}{B_i}} + [E + Fx + Gx^2] \quad (5.6)$$

where the first bracketed term is the sum of the n Lorentzians and the second term is the parabola. In the equation, A_i , p_i , and B_i are the amplitude, position, and half-width of the i^{th} peak (Lorentzian) and E , F , and G , are the conventional parameters of the parabola.

From the values obtained in the curve fitting for each n pair of peaks, the chemical shift (δ_n) and quadrupole splitting (Δ_n) parameters were determined using Equations 5.7 and 5.8. Table 5.9 present the summary of the results.

$$\delta_n = \frac{(p_{n_1} + p_{n_2})}{2} \quad (5.7)$$

$$\Delta_n = p_{n_2} - p_{n_1} \quad (5.8)$$

The isomer shift and quadrupole splitting obtained for FeP₂ agree nicely with the literature values ($\delta = 0.09 \pm 0.03$ mm/s and $\Delta = 2.08 \pm 0.02$ mm/s),⁴⁵ and are consistent with iron in pure $3d^4$ configuration. This result attests to the purity of the starting material. In accordance with EXAFS analysis, the Mössbauer spectroscopy

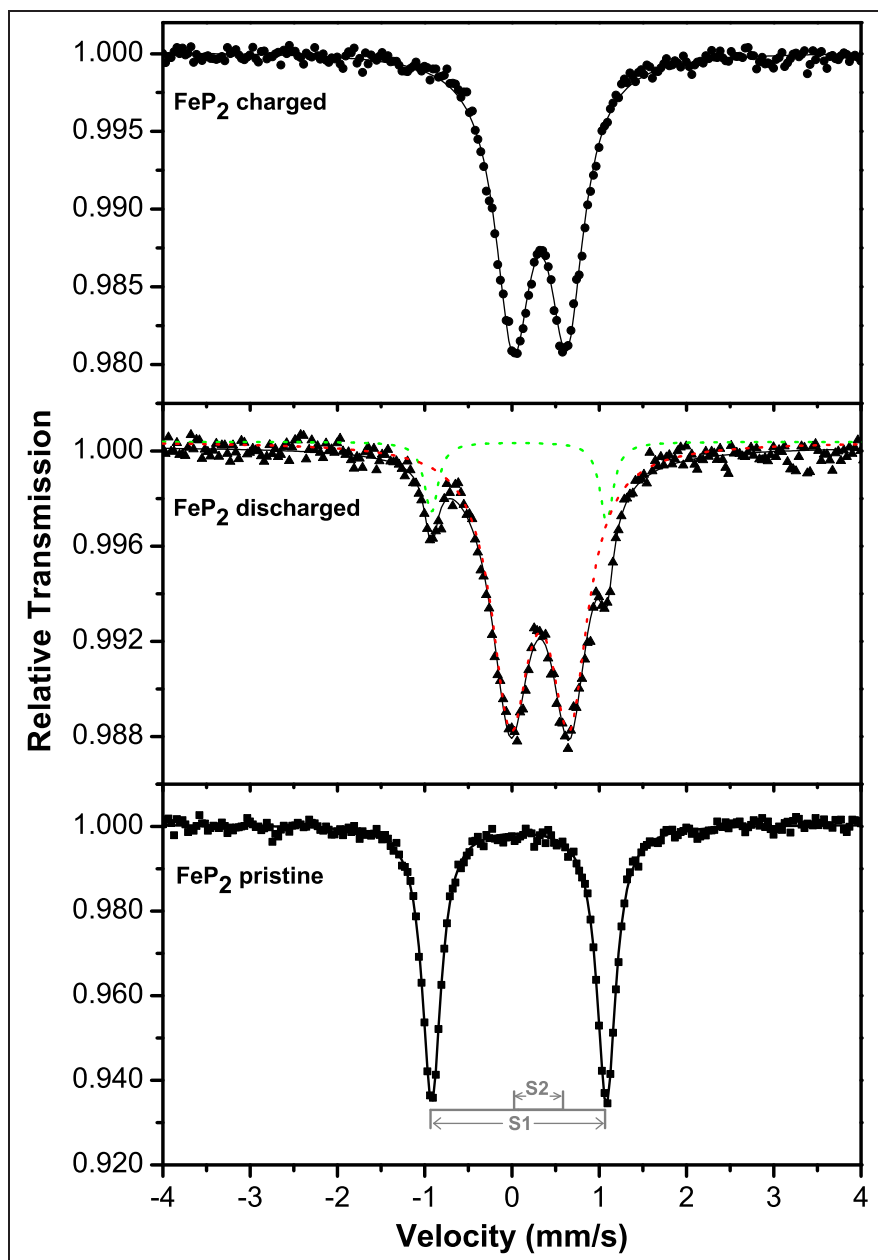


Figure 5.14: Mössbauer spectra for FeP₂ samples obtained at room temperature and referenced to α -Fe. The dotted lines depict the deconvoluted signals.

Table 5.9: Mössbauer parameters calculated for FeP₂ samples.

Sample	Signal	δ <i>mm/s</i>	Error δ <i>mm/s</i>	Δ <i>mm/s</i>	Error Δ <i>mm/s</i>	Contribution %
Pristine	S1	0.080	0.001	2.002	0.002	100.0
Discharge	S1	0.080	0.007	2.008	0.015	9.7
	S2	0.320	0.005	0.674	0.009	90.3

data on the cycled material suggest that Fe stays in a coordination environment depicting close contact with phosphorus. Upon discharge, there is a significant reduction of the FeP₂ signal (S1), indicating incomplete reduction of the composite anode, which completely disappears after charge. Additionally, a new doublet (S2) appears in the spectrum upon discharge. The increase in isomer shift upon cycling indicates stronger interaction between the Fe-3*d* and filled P-3*p* orbitals;⁴⁶ according to the model proposed by Danon,⁴⁷ it corresponds to iron in 3*d*⁵4*s*^{0.32}. The values of isomer and quadrupole shift for S2 are comparable to that of Fe in FeP ($\delta = 0.375$ and $\Delta = 0.750$)⁴⁵ suggesting that Fe is in close contact with phosphorus atoms in the electrochemically formed phase “Li₆FeP₂”. Moreover, no magnetic splitting was observed even at 4 K, which rules out the formation of Fe⁰, Fe₃P, or iron carbides by the absence of hyperfine interactions.^{48–50} Unfortunately, the sample obtained at the end of charge was contaminated during its transport to France, compromising the Mössbauer data obtained for it.

5.4 Conclusions

The behaviour in the FeP_2 system upon electrochemical lithium uptake can be nicely contrasted to MnP_4 , where the existence of a crystalline ternary phase (Li_7MnP_4), allows for reversible structural crystalline transformation between the two phases on electrochemical Li uptake and extraction. A phase transition of this nature is not possible for FeP_2 due to the lack of thermodynamic stability of the Li-Fe-P phase of the corresponding stoichiometry. From a thermodynamic point of view, only two events can occur on Li uptake at room temperature: either phase separation into $\text{Li}_3\text{P} + \text{Fe}$ or the formation of a metastable ternary phase. Our results show that the latter takes place. The sum of the XAS, magnetization and Mössbauer data unequivocally demonstrate formation of a metastable Li-Fe-P phase which displays a high level of disorder. This nanostructured material contains Fe_xP -rich magnetic domains and Li-P rich regions in which the iron atoms retain coordination to P:



The formation of a metastable disordered ternary phase can be ascribed to the similarity of the phosphorus atom arrangement in FeP_2 and Li_3P , as depicted by the scheme in Figure 5.15. In the figure, both structures are oriented perpendicularly to two close-packed (*cp*) phosphorus layers. In Li_3P the phosphorus atoms form an hexagonal close-packed arrangement, whereas the structure of FeP_2 shows a small

distortion from ideal *cp*. To illustrate the topographical correspondence in the two structures, the three atoms that form the upper trigonal *cp* surface are highlighted in different colors (purple, green, and cyan), and the three atoms that span the lower trigonal plane are in black. The major differences between the two structures lie in: (a) The occupation of the additional cation sites in Li_3P and (b) An increase in the P–P distances from 2.7/3.1 Å in FeP_2 to 4.27 Å in Li_3P .

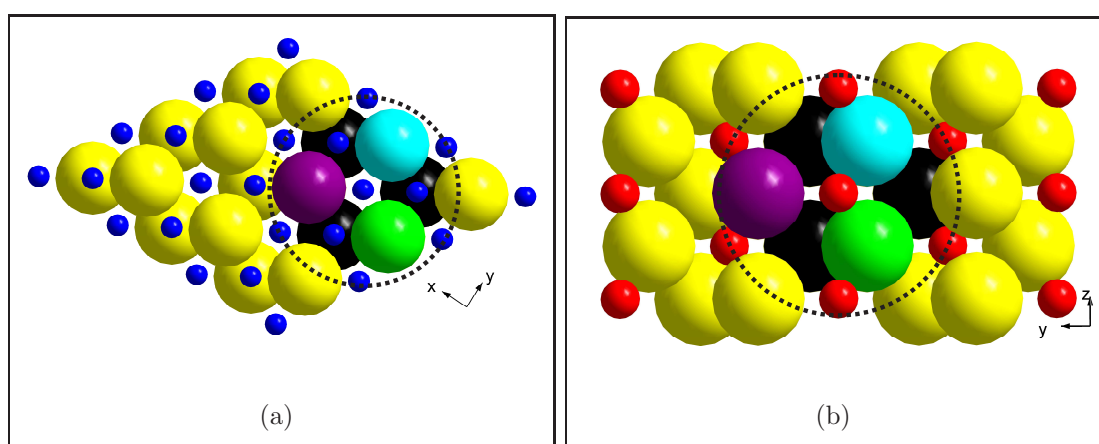


Figure 5.15: Comparison between the (a) Li_3P and (b) FeP_2 structures. P atoms: large spheres (yellow, black, purple, green, and cyan); Li atoms: small blue spheres; Fe atoms: medium red spheres.

The electrochemical formation of metastable ternary phases has been very recently suggested in the transformation of LiMnSb into Li_3Sb via a metastable solid solution $\text{Li}_{1+2x}\text{Mn}_{1-x}\text{Sb}$.⁵¹ In oxides, owing to the strong ionic character of the compounds, the reduction to the metallic state is driven by a large free energy of reaction. Comparatively, in phosphides the high degree of covalent bonding and low valence of the metal induces a transformation more akin to “intercalation” — either a structural

rearrangement ($\text{MnP}_4\text{-Li}_7\text{MnP}_4$) or the transformation to a semi-disordered state observed here. This behaviour contrasts with that of the lower members of Group 15 elements (i.e. antimonides), as these materials are characterized by complete phase separation into the lithium antimonide and the metal, as occurs for FeSb_2 .⁵²

Considering the two structures and the results previously discussed, the following mechanism is proposed to explain Li uptake by FeP_2 :

1. First, expansion of the phosphorus lattice, and incorporation of the additional lithium to form a disordered, stuffed metastable “ $\text{Li}_3\text{Fe}_{0.5}\text{P}$ ” lattice that still maintains Fe within the structure. This process would disrupt the P–P bonding by the occupancy of antibonding P–P levels by the first extra electron — as observed in the Mössbauer data.
2. Second, the FeP_6 octahedra would be isolated from each other by an expansion of the P–P distance. Such a transformation would suppress Fe–Fe interactions but maintain Fe–P bonding—consistent with the observed EXAFS data.
3. Last, on charge, Li is extracted from the disordered phase to yield a material that, although amorphous, contains some of the local coordination between FeP_6 octahedra.

References

- [1] Monconduit, L.; "Tillard-Charbonnel", M.; Belin, C. *J. Solid State Chem.* **2001**, *156*, 37.
- [2] Jeitschko, W.; Donohue, P. *Acta Cryst.* **1972**, *B28*, 1893.
- [3] Jeitschko, W.; Donohue, P. *Acta Cryst.* **1973**, *B29*, 783.
- [4] Doublet, M.-L.; Lemoigno, F.; Gillot, F.; Monconduit, L. *Chem. Mat.* **2002**, *14*, 1983.
- [5] Kim, Y.-U.; Sohn, H. "Novel vanadium monophosphide (VP) insertion anode material for lithium secondary batteries". In *Proceedings of the 207 ECS Meeting*; Electrochemical Society: QC-Canada, 2005.
- [6] Wang, K.; Yang, J.; Xie, J.; Wang, B.; Wen, Z. *Electrochem. Comm.* **2003**, *5*, 480.
- [7] Crosnier, O.; Nazar, L. F. *Electrochem. Solid State Lett.* **2004**, *7*, A187.

- [8] Pfeiffer, H.; Tancrét, F.; Brousse, T. *Electrochim. Acta* **2004**, *50*, 4763.
- [9] Crosnier, O.; Mounsey, C.; Herle, P. S.; Taylor, N.; Nazar, L. F. *Chem. Mat.* **2003**, *15*, 4890.
- [10] Gillot, F.; Monconduit, L.; Morcrette, M.; Doublet, M.-L.; Dupont, L.; Tarrascon, J.-M. *Chem. Mat.* **2005**, *17*, 3627.
- [11] Bichatt, M.-P.; Pascal, J.; Gillot, F.; Favier, F. *Chem. Mat.* **2005**, *17*, 6761.
- [12] Schmidt, D. G. U.S. Pat. 2002037452, 2002.
- [13] Honbo, H.; Yamagata, T.; Muranaka, K. Jpn. Pat. 10199527, 1998.
- [14] Inagaki, H.; Takami, N. Eur. Pat. Appl. 1134824, 2001.
- [15] Thompson, A. H.; Whittingham, M. S. *Mater. Res. Bull.* **1977**, *12*, 741.
- [16] Klutz, H.; Schneider, G.; Kliche, G. *Phys. Chem. Min.* **1983**, *9*, 109.
- [17] Lefebvre-Devos, M. L.; X. Wallart, J. Olivier-Fourcade, L. M.; Jumas, J.-C. *Phys. Rev. B: Condens. Matter* **2001**, *63*, 125110.
- [18] Souza, D.; Pralong, V.; Jacobson, A.; Nazar, L. *Science* **2002**, *296*, 2012.
- [19] Meisel, V.-K. *Z. Anorg. Allg. Chem.* **1934**, *B218*, 360.
- [20] Dahl, E. *Acta Chem. Scand.* **1969**, *23*, 2677.
- [21] Flörke, V. U. *Z. Anorg. Allg. Chem.* **1983**, *502*, 218-224.

- [22] Larson, A.; Dreele, R. V. "General Structure Analysis System (GSAS)", Technical Report LAUR 86-748, Los Alamos National Laboratory, 2000.
- [23] Toby, B. *J. Appl. Crystall.* **2001**, *34*, 210.
- [24] Rietveld, A. *Acta Cryst.* **1967**, *22*, 151.
- [25] Howard, C. *J. Appl. Crystall.* **1982**, *15*, 615.
- [26] Poizot, P.; Baudrin, E.; Laruelle, S.; Dupont, L.; Touboul, M.; Tarascon, J.-M. *Solid State Ionics* **2000**, *138*, 31.
- [27] Mao, O.; Turner, R. L.; Courtney, I. A.; Fredericksen, B. D.; Buckett, M. I.; Krause, L. J.; Dahn, J. R. *Electrochem. Solid State Lett.* **1999**, *2*, 3.
- [28] Winter, M.; Besenhard, J. O.; Spahr, M.; Novak, P. *Adv. Mater.* **1998**, *10*, 725.
- [29] Box, G. *Statistic for Experimenters*; John-Wiley & Sons: New York, 1978.
- [30] Montgomery, D. *Design and Analysis of Experiments*; John-Wiley & Sons: New York, 1995.
- [31] Brauer, G.; Zintl, E. *Z. Phys. Chem. Ab. B* **1937**, *37*, 323.
- [32] Leroux, F.; Goward, G.; Power, W.; Nazar, L. *Electrochem. Solid State Lett.* **1998**, *1*, 255.
- [33] Rossignol, C.; Ouvrard, G. *J. Power Sources* **2001**, *97-8*, 491-493.

- [34] Mansour, A.; Yang, X.; Sun, X.; McBreen, J.; Croguennec, L.; Delmas, C. *J. Electrochem. Soc.* **2000**, *147*, 2104.
- [35] Giorgetti, M.; Passerini, S.; Smyrl, W.; Mukerjee, S.; Yang, X.; McBreen, J. *J. Electrochem. Soc.* **1999**, *146*, 2387.
- [36] Cullity, B. *Introduction to Magnetic Materials*; Addison-Wesley: Philipines, 1972.
- [37] Boda, G.; Stenstrddoto, B.; Sagredo, V.; Beckman, O.; Carlsson, B.; Rundqvist, S. *Physica Scripta* **1971**, *4*, 132.
- [38] Selwood, P. *Chemisorption ad Magnetization*; Academic Press Inc.: New York, 1975.
- [39] Morrish, A. H. *The Physical Principles of Magnetism*; John-Wiley & Sons: New York, 1965.
- [40] Zhang, S. J.; Tsuboi, A.; Nakata, H.; Ishikawa, T. *J. Power Sources* **2001**, *97-8*, 584.
- [41] Ibusuki, T.; Kojima, S.; Kitakami, O.; Shimada, Y. *IEEE Trans. Mag.* **2001**, *37*, 2223.
- [42] Kim, J.; Amine, K. *Electrochem. Comm.* **2001**, *3*, 52-55.

- [43] Jiles, D. *Introduction to Magnetism and Magnetic Materials*; Chapman & Hall: London, 1st ed.; 1991.
- [44] Rhodes, E.; Polinger, A.; Spijkerman, J.; Christ, B. *Trans. Met. Soc. AIME* **1968**, *242*, 1922.
- [45] Wäppling, R.; Häggström, L.; Rundqvist, S.; Karlsson, E. *J. Solid State Chem.* **1971**, *3*, 276.
- [46] Walker, L.; Wertheim, G.; Jaccarino, V. *Phys. Rev. Lett.* **1961**, *6*, 98.
- [47] Danon, J. *Tech. Rep. Ser., Int. At. Energy Ag.* **1966**, *50*, 89.
- [48] Petrov, Y.; Shafranovsky, E.; Krupyanskii, Y.; Essine, S. *J. Appl. Phys.* **2002**, *91*, 352.
- [49] Bailey, R.; Duncan, J. *Inorg. Chem.* **1967**, *6*, 1444.
- [50] Bi, X.-X.; Ganguly, B.; Huffman, G.; Huggins, F.; Endo, M.; Eklund, P. *J. Mater. Res.* **1993**, *8*, 1666.
- [51] Fransson, L. M. L.; Vaughey, J. T.; Edström, K.; Thackeray, M. M. *J. Electrochem. Soc.* **2003**, *150*, A86.
- [52] Crosnier, O.; Silva, D. C. C.; Ouvrard, G.; Danot, M.; Nazar, L. F. **in preparation**, .

Chapter 6

Cobalt Phosphide System

6.1 Introduction

Investigations of transition metal oxides as anode materials, first reported by Idota *et al.*, Nazar and co-workers, and Tarascon and co-workers,¹⁻⁴ developed new concepts concerning the mechanism of Li “insertion”. In bulk MoO₃, Li uptake drives the reduction of the metal to form a nanophase matrix of Li₂O, and metal sub-oxide particles; on charge, Mo-oxide is regenerated although a “crystalline” MoO₃ phase is not fully achieved. Similarly, reduction of nanophase CoO produces Co nano-particles in a matrix of Li₂O but in this case nano-CoO is regenerated on charge. Subsequently, Obrovac *et al.* showed that the latter reaction can be thought of as a displacement reaction of the Co²⁺ by Li⁺ ions within the oxide matrix on discharge, the reverse

occurring on charge.⁵ In these relatively “ionic” systems, reduction is driven by the difference in thermodynamic free energy between the oxidized and reduced states of the metal.

The quest for alternative anode materials for lithium ion batteries turned towards one more phosphide with an open structure, but this time with no known ternary lithiated phase. CoP_3 crystallizes in the skutterudite-type structure with 3D channels of average dimensions $5.38 \text{ \AA} \times 2.33 \text{ \AA}$.^{6,7} The structure, which resembles that of the marcasite-type FeP_2 (see Chapter 5), may be described as a cubic sub-lattice of cobalt atoms, with cell dimension $a/2$ in which six four-membered phosphorus rings are inserted in the cubes along the axial directions (Figure 6.1(a)).⁸ Alternatively, it may be viewed as consisting of corner-shared CoP_6 octahedra that are tilted to form P_4 rings (Figure 6.1(b)).

To the best of our knowledge, the electrochemical reactions of CoP_3 toward lithium had not been investigated before we started our studies. In 2002, however, Alcántara and co-workers⁹ published results on the cobalt phosphide system contemporaneous with our communication in the same year.¹⁰ In 2005, Zhang *et al.*¹¹ reported on electrochemical results of a CoP and CoP_3 mixture prepared by mechanical milling. A comparison between these and our results is presented here.

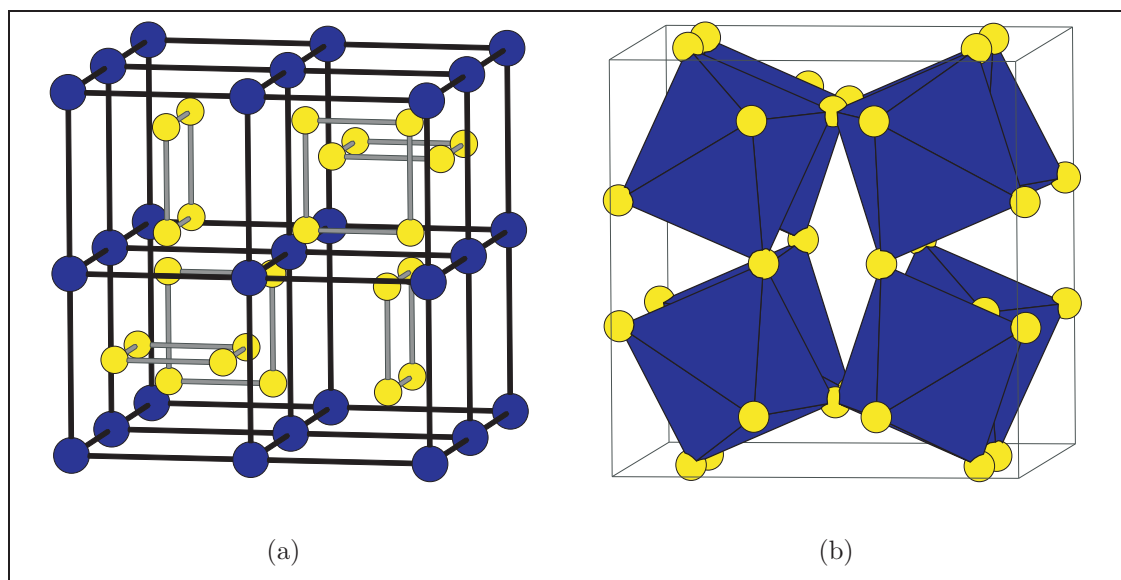


Figure 6.1: (a) Geometrical and (b) polyhedral representations of the CoP₃ structure.

6.2 Experimental

6.2.1 Synthesis of CoP₃

Stoichiometric amounts of cobalt and red phosphorus were mixed inside an argon filled glove-box with the aid of a mortar and pestle and transferred to a stainless-steel crucible (see description in Section 5.2.1) which was then arc-welded under an argon atmosphere. The reaction was carried out for 24 hours at 800 °C. After quenching the reactions in a cold water bath, the tubes were cut open and the obtained product ground manually with a mortar and pestle and sieved through a 400 mesh nylon grid.

6.2.2 Synthesis of LiP

Stoichiometric amounts of metallic lithium and red phosphorus were mixed inside an argon filled glove-box with the aid of a mortar and pestle and transferred to a stainless-steel crucible (see description in Section 5.2.1) which was then arc-welded under an argon atmosphere. The reaction was carried out for 24 hours at 600 °C then quenched in a cold water bath. The tubes were opened and the obtained materials were stored under argon atmosphere.

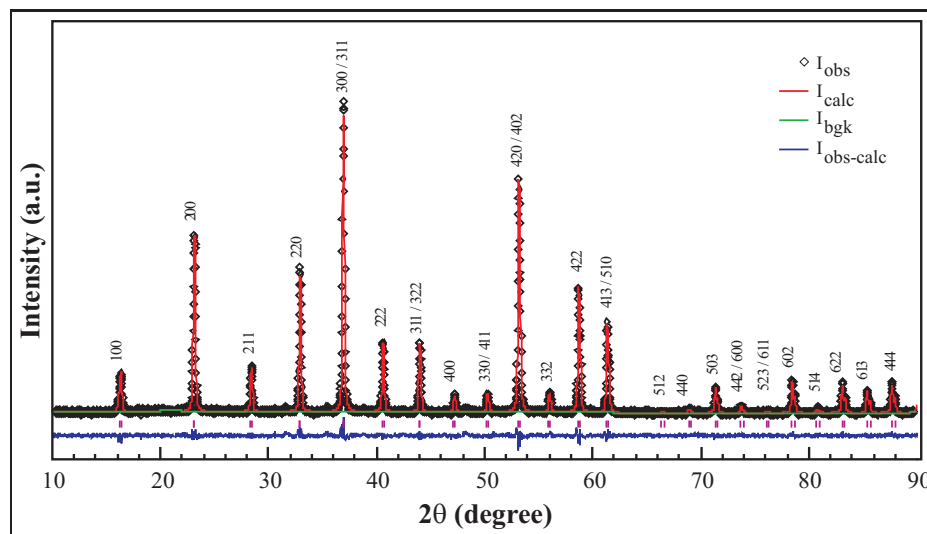
6.3 Characterization and Properties CoP_3

6.3.1 Structure and Composition of the Materials

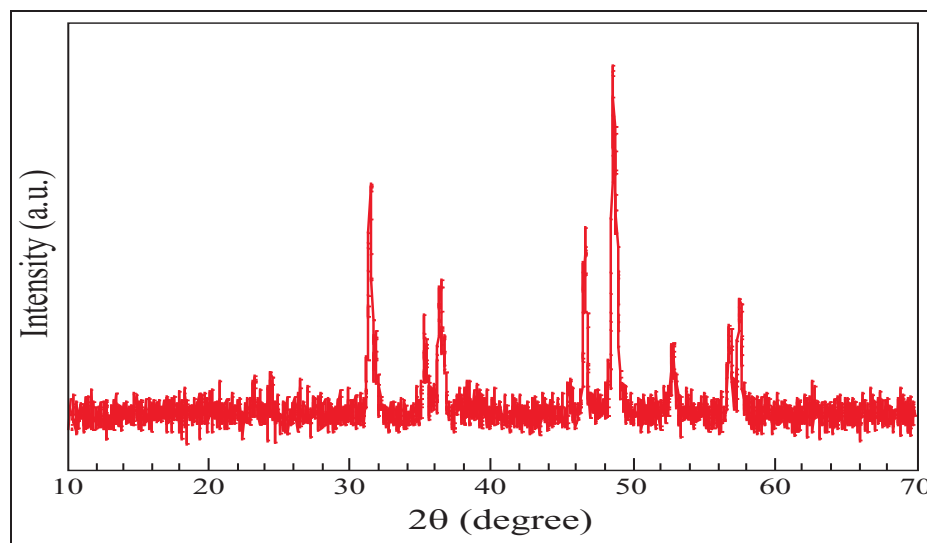
The synthetic methods described to obtain CoP_3 reported in the early literature use either stoichiometric amounts of the pure elements at high temperatures or the Jolibois flux technique (heating of an alloy of Co-Sn with excess phosphorus followed by dissolution of the tin phosphide matrix with HCl) at lower temperatures.^{6,7,12} The stoichiometric approach is done by heating the mixture in sealed silica tubes at temperatures between 950 – 1400 °C over several days followed by slow cooling to room temperature.⁷ These earlier reports suggest that medium pressures (at 1000 °C the vapour pressure of phosphorus over the reacting mixture is around 400 Torr and decreases rapidly at lower temperatures) and slow cooling are essential

for the formation of the desired phase – otherwise some phosphorus is left unreacted. Recently, niobium tubes were used as crucibles and the reaction was carried out for 1 week at 800 °C followed by quenching to room temperature.⁹ Additionally, high energy ball-milling of stoichiometric amounts of phosphorus and cobalt for less than 11 hours forms a mixture of CoP_3 and small amounts of CoP .¹¹

In this work, the methodology used to prepare CoP_3 was straightforward. Differing from the aforementioned reports, the reaction crucibles were made of stainless-steel tubes instead of quartz or niobium, and much shorter reaction times were employed. In addition, slow cooling of the reaction led to the formation of CoP instead of the desired triphosphide (see Figures 6.2(a) and 6.2(b)), which formed upon quenching. The products structure and purity were confirmed by XRD analysis. The data was collected between $20^\circ < 2\theta < 70^\circ$, in steps of 0.01° during 20 s and refined in the cubic space group $Im\bar{3}$ with GSAS,^{13,14} using the Rietveld method for full pattern match.¹⁵ The refined variables were the scale factor, background polynomial coefficients, unit cell parameters, atomic positions, and pseudo-Voigt peak shape (using of the type 2 profile function for constant wavelength diffraction data).¹⁶ As shown in Figure 6.2(a) and Table 6.1, the refinement of the XRD pattern yielded structure and atom parameters complying with those previously reported.¹⁷



(a)



(b)

Figure 6.2: Powder XRD patterns of $\text{Co} + 3\text{P}$ reaction products obtained after (a) quenching (CoP_3 , Rietveld refinement) and (b) slow cooling to room temperature (CoP).

Table 6.1: Results of the CoP₃ XRD pattern Rietveld refinement in the space group $Im\bar{3}$.

Sample	CoP ₃	Reference ¹⁷
Unit Cell Parameter (Å)	7.7073±0.0005	7.7027
Cell Volume (Å ³)	457.02±0.09	457.01
Formula Weight	1214.84	1214.84
Density (g/cm ³)	4.41	4.42
R _p ^a (%)	5.48	n.a.
R _{wp} ^b (%)	7.06	n.a.
χ ²	1.97	n.a.
Number of Refined Variables	12	n.a.

$$^a R_p = \frac{\sum ||I_{exp} - I_{calc}||}{\sum F_{exp}}$$

^b $R_{wp} = \sqrt{\frac{M_p}{\sum w_{calc}^2}}$, where $M_p = \sum w(I_{obs} - I_{calc})^2$ is the powder data contribution for the general least squares minimization function

6.3.2 Electrochemical Studies of CoP₃

Figure 6.3 shows the electrochemical behaviour of CoP₃ under galvanostatic conditions at C/10. The first discharge process (Figure 6.3(a)) is characterized by a flat plateau corresponding to the uptake of ≈ 9 Li (after correction for the carbon contribution). On charge, 6 lithium ions are extracted leading to a reversible capacity of 1000 mAh/g, which fades and stabilizes at 300 mAh/g after 10 cycles (Figure 6.3(b)). This result differs from the data presented by Alcántara who reported a maximum of 1090 mAh/g and 375 mAh/g in the first discharge and charge, respectively, at a rate of C/20 and smaller voltage window (1.2-0.45 V); reduction of the lower voltage limit to 0.1 V markedly diminished the reversible capacity without increasing the initial amount of lithium uptake.⁹ Considering the much longer reaction times employed in their synthetic procedure (1 week *vs.* 1 day), the CoP₃ phase they prepared probably had a larger particle size than ours. Hence, the lower capacity values observed by them was probably due to the increased path-length for lithium diffusion, which hinders the kinetics.

By means of potentiostatic intermittent titration technique, a bell shaped current response associated with a constant voltage during the first cycles (Figure 6.4) confirmed the occurrence of a two-phase decomposition process.¹⁸ The equilibrium voltage obtained for the first discharge (0.35 V) is much lower than the values for the subsequent sweeps ($V_{Eq_{1st\ charge}} = 0.385$ V and $V_{Eq_{2nd\ discharge}} = 0.99$ V). This difference

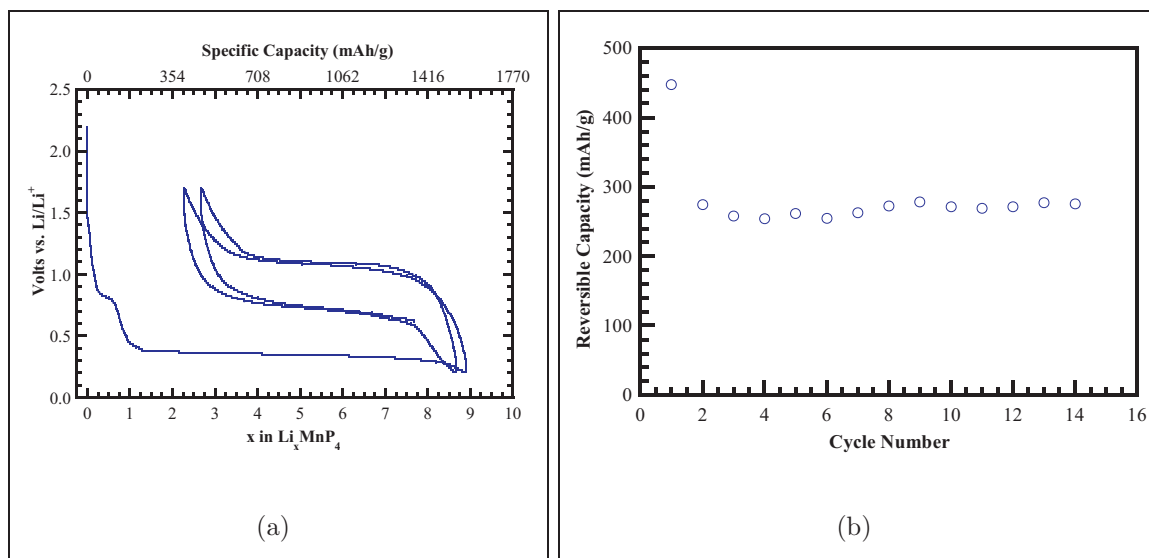


Figure 6.3: Galvanostatic voltage-composition profile of CoP₃ at C/10 rate.

indicates that the decomposition reaction in the first discharge is irreversible in nature and generates the active material for the two-phase reversible process in subsequent cycles. The difference in the potential of lithium in the structure of charged and discharged phases can account for the large difference in equilibrium voltage.

The possible reaction of CoP₃ with Li⁺ in the first discharge according to the equation



compares to the behaviour reported for CoSb₃ by Tirado *et al.* who proposed a transformation into (Li₃Sb + Co⁰) on Li uptake.¹⁹ In order to investigate the mechanism of electrochemical uptake of lithium by the analogous but more ionic phosphide, structural and chemical analysis were carried out on electrodes cycled to

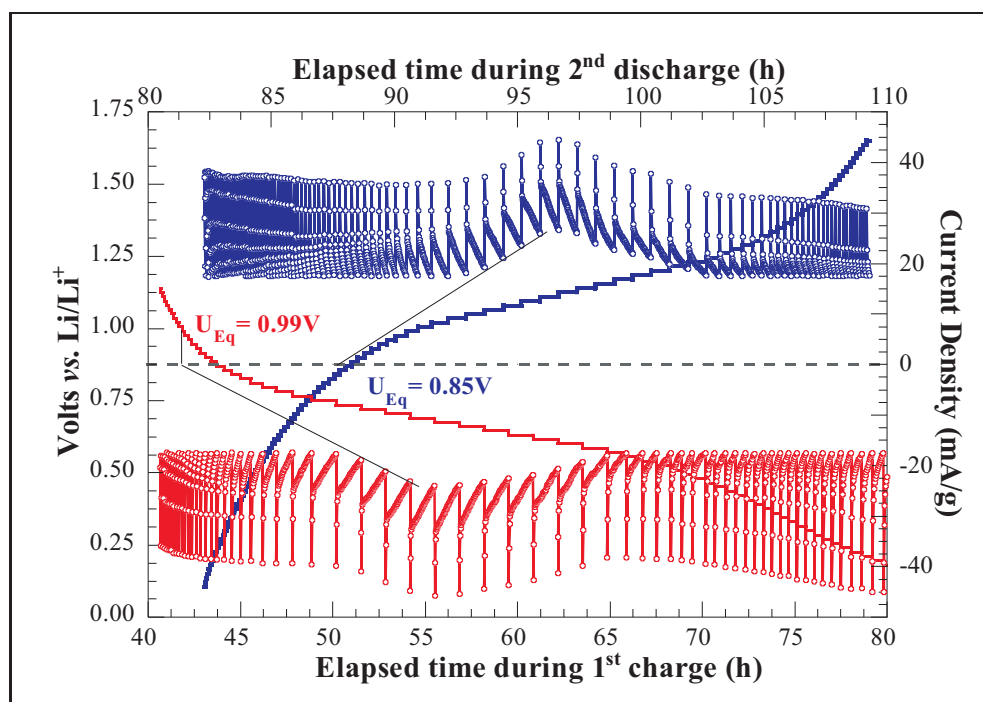


Figure 6.4: First cycle PITT profile of CoP_3 at C/5.

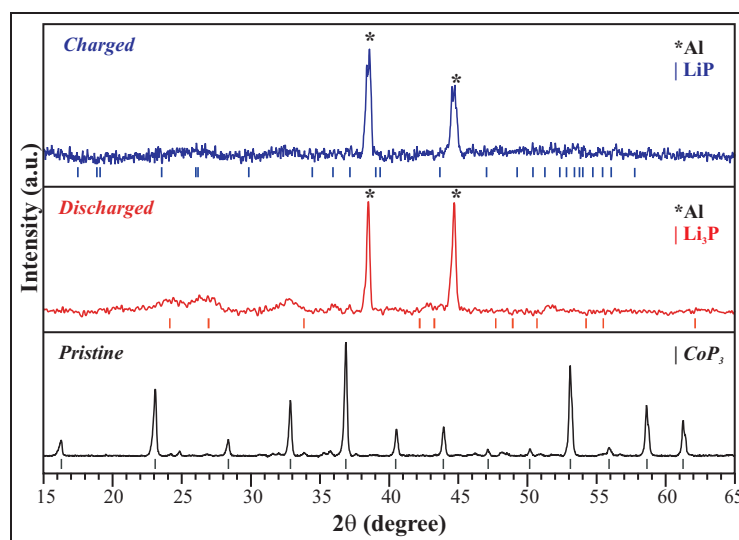
different redox states.

6.3.3 *Ex-situ* Analysis of Cycled CoP_3

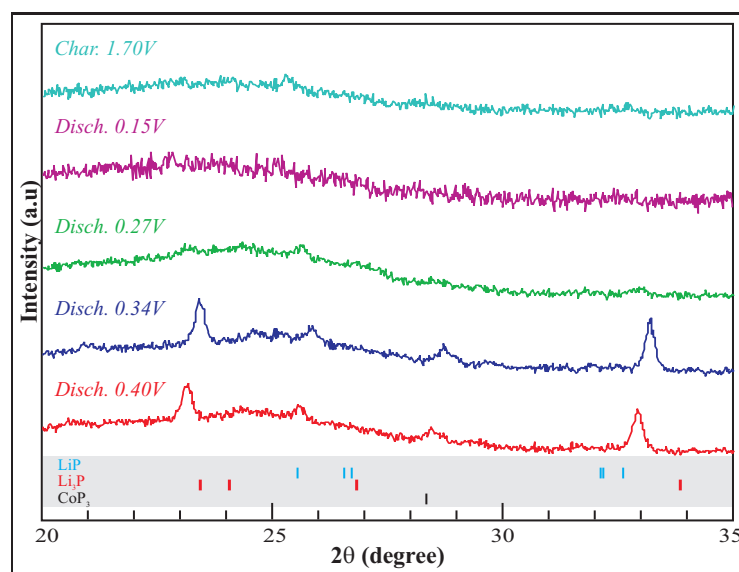
Ex-situ and *In-situ* XRD

The XRD pattern of the CoP_3 electrode at the end of the first discharge (Figure 6.5) clearly shows, along with partial amorphization of the electrode material, reflections of the Li_3P phase as well as lines assigned to unreacted CoP_3 ; the lines corresponding to metallic cobalt, however, are absent. Upon oxidation corresponding to the extraction of 6 Li, the material becomes completely amorphous.

The XRD data of the cycled material, both *ex-situ* and *in-situ*, suggest that in the phosphide system, cobalt is either extruded from the structure as nanoparticles and/or remains in a partially covalently bonded environment. Furthermore, it raises an important question: does oxidation result in re-formation of highly dispersed CoP_3 (as in the case of the oxide, CoO) or is the process more complex? In an attempt to investigate the lithium-driven structural and morphological changes, the CoP_3 electrode was examined at various stages of reduction and oxidation by means of transmission electron microscopy.



(a)



(b)

Figure 6.5: XRD patterns of cycled CoP_3 : (a) *Ex-situ* profiles before cycling and at the end of first discharge and charge (* Al from cell hardware); (b) *In-situ* profiles in a narrower 2θ range (LiP/Li₃P region) at various stages of the first cycle.

***Ex-situ* TEM**

The TEM micrograph of the starting material (Figure 6.6(a)) shows that it comprises particles with dimensions ranging from 200 to 100 nm. As expected, the SAED pattern taken down the $[1\bar{1}\bar{1}]^*$ zone axis (Figure 6.6(d)) is consistent with the presence of well-crystallized particles, in accord with the XRD results. The bright field image of the particles after full reduction, Figure 6.6(b), reveals significant changes in the material texture. Particles with dimensions of 10–20 Å are detected embedded in the crystallites which retain their initial shape. The reaction forms a partially amorphous material as confirmed by the broad, weak rings observed in the SAED pattern. Indexing of the pattern (Figure 6.6(e)) to the reflections of Li_3P gave excellent agreement, confirming the formation of lithium phosphide upon lithiation. Additionally, analysis of the broad ring pattern did not reveal any inter-planar spacings assigned to cobalt metal; even the 111 reflection, which should be particularly strong, is completely absent. As there is also no evidence for the presence of CoO nanoparticles, the cobalt must remain “partially coordinated” to the Li_3P matrix, giving rise to the extremely high degree of dispersion. These particles, of dimensions approaching that of metal clusters (15 Å), are not observable by SAED due to extreme broadening.²⁰

On charge, Figures 6.6(c) and 6.6(f), both the nanoscopic size and pseudo-amorphous character of the active material are preserved. The SAED pattern clearly

shows the replacement of the Li_3P reflections by those of LiP^* , but there is no evidence of CoP_3 regeneration. Hence, the electrochemical process seems best characterized as a redox reaction between Li_3P and LiP , in agreement with the findings of Alcántara and co-workers, based on XRD data and thermodynamic considerations.⁹ Table 6.2 summarizes the indexing results.

***Ex-situ* XPS**

An important question remains: whether the cationic or the anionic network plays the major role in the electrochemical redox process of CoP_3 . The reversibility and nature of the intriguing process involved in the electrochemical uptake of lithium by CoP_3 was addressed with *ex-situ* XPS analysis of the cycled material. Since the binding energy is characteristic of the elements present and their chemical states, the x-ray photoelectron spectra provide direct “fingerprint” of the samples.

Figure 6.7 shows the spectra of the fully discharged and charged electrodes after ion sputtering to clean the surface. Unfortunately, the resolvable Co 2p region cannot be used to elucidate the exact role of the cobalt because the $2p_{1/2,3/2}$ states of both metallic and covalent species are almost at the same energy level and the thresholds do not change significantly upon cycling (measured thresholds of Co 2p states in pristine CoP_3 , discharged, and charged materials were, respectively, 793.5/778.4 eV,

* The diffraction diaphragm opening was increased 10x, in order to enlarge the data sampling area; this explains the brightness of the SAED pattern obtained for a *quasi*-amorphous phase with relatively featureless XRD pattern. This technique is commonly used in samples containing nano-sized particles that do not show discrete features in their XRD pattern.^{21,22}

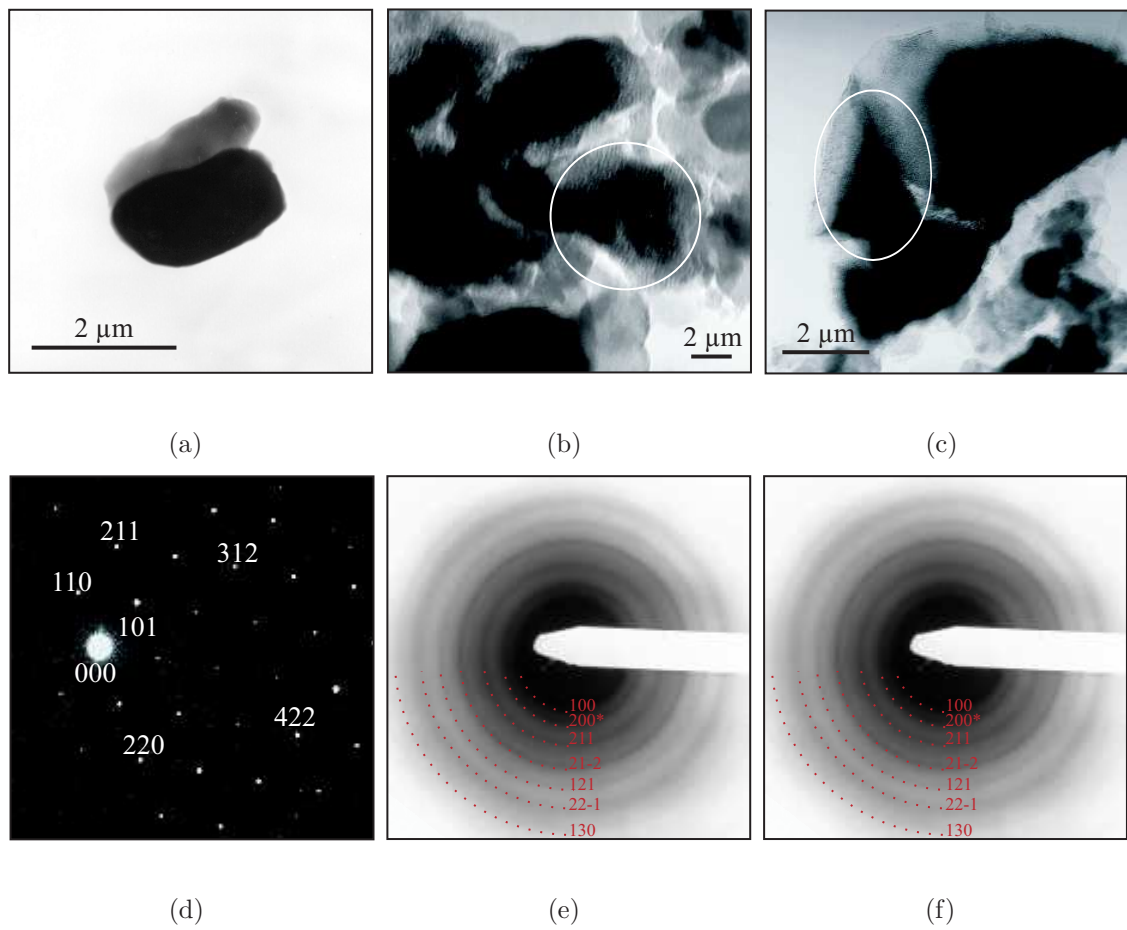


Figure 6.6: *Ex-situ* TEM micrographs (a, b, c) and SAED patterns (d, e, f) of pristine, discharged, and charged CoP₃ respectively.

Table 6.2: SAED pattern indexing results for pristine and cycled CoP_3 .

Reference			Measured Data				
Material	d -spacing	hkl	Sample	SAED		XRD	
				d -spacing	hkl	d -spacing	hkl
CoP_3	5.450	110	Pristine	5.412	110	5.447	110
	3.854	200		–	–	3.852	200
	3.146	211		3.157	211	3.145	211
	2.725	220		2.706	220	2.723	220
	2.060	312		2.066	312	2.059	312
	1.643	332		–	–	1.642	332
	1.573	422		1.579	422	1.572	422
Li_3P	3.789	002	Discharged	–	–	3.790	002
	3.693	100		3.701	100	3.697	100
	3.320	101		–	–	3.223	101
	2.645	102		2.643	102	2.646	102
	2.132	110		2.115	110	2.135	110
	2.085	103		1.396	210	2.086	103
	1.396	210		1.175	302	3.854	202 ^a
	1.171	302		1.645	113 ^a	2.725	220 ^a
	–	–		–	–	2.437	301 ^a
LiP	4.922	100	Charged	4.830	100	<i>Amorphous</i>	
	3.694	$\bar{1}11$		3.864	200 ^a		
	3.335	012		3.116	211		
	2.424	$21\bar{1}$		2.415	$21\bar{2}$		
	2.047	121		2.056	121		
	1.829	$22\bar{1}$		1.789	$22\bar{1}$		
	1.562	130		1.533	130		

^a CoP_3

794.0/779.0 eV, and 793.7/778.7 eV). Data collected in the overlapping regions of the Co 3p and Li 1s states, however, is quite revealing. In both spectra, the broad features at 60 eV (P1) can be assigned to the Co 3p ($1/2$, $3/2$) states, by comparison with reference data.²³ Since this peak position should remain unchanged in accordance with the invariance of the Co 3p states, changes in the spectra must thus be rooted in the Li 1s states.

The Li 1s region in the spectra of both cycled materials depicts the signature peak at 56 eV (P2) which corresponds to Li^+ from residual electrolyte (LiPF_6). In the spectrum of the discharged sample, P2 overlaps with another peak P3 at 56.87 eV which, by curve deconvolution and comparison with the literature value of 56.9 eV, is assigned to the Li 1s state in Li_3P .²³ On charge, P3 shifts to a higher binding energy (59 eV) indicating a reduction in the phosphorus oxidation state. Comparison with the spectrum of synthesized LiP reference material provides unequivocal assignment of the peak to Li 1s state in LiP (binding energy 59.03 eV).

These results, along with the electron diffraction data, confirm the formation of LiP on charge. Moreover, the XPS data suggest that cobalt does not play a major role in the redox process, since its binding energy does not change upon reduction or oxidation.

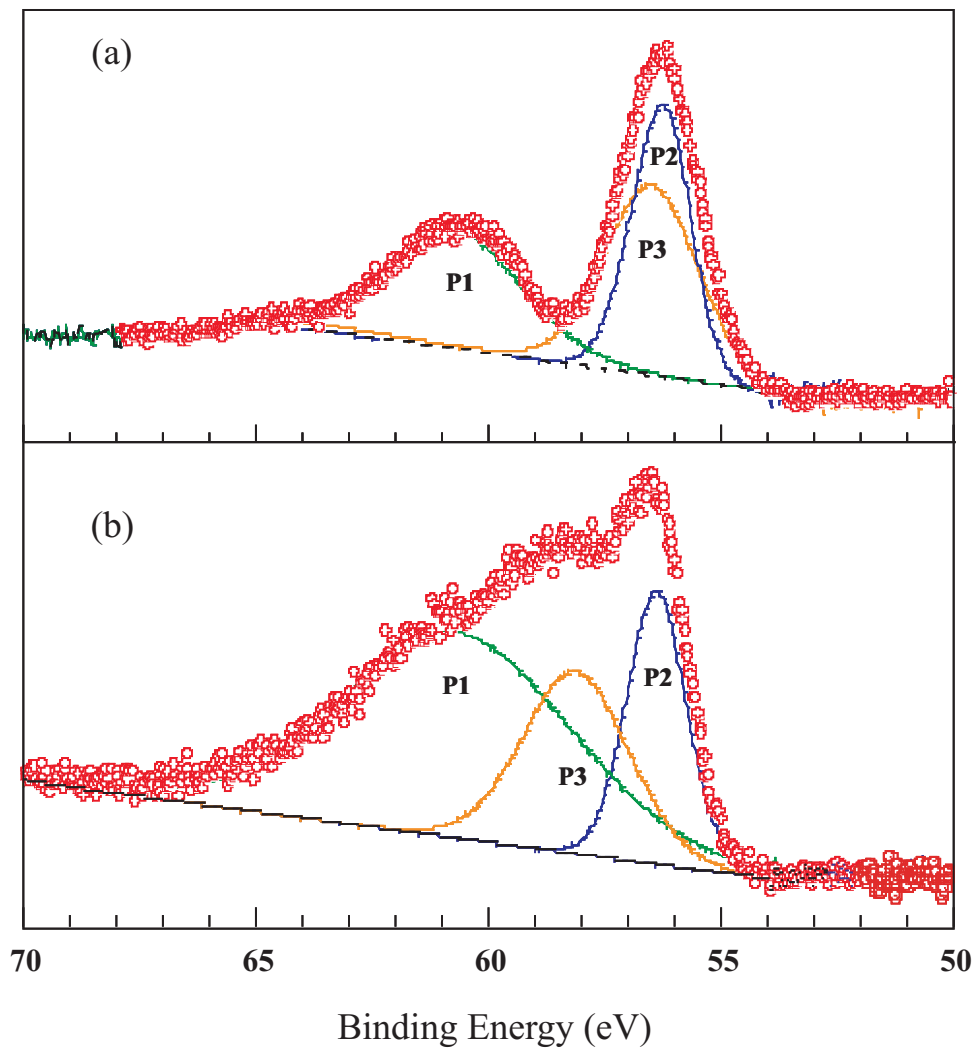
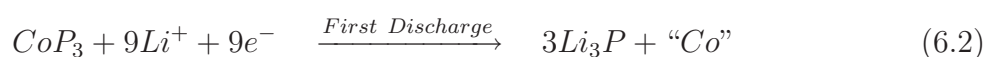


Figure 6.7: *Ex-situ* XPS spectra of cycled CoP₃: (a) discharged (Li₉CoP₃) and (b) charged (Li₃CoP₃).

6.3.4 Proposed Mechanism

Based on the results presented here, a simplified mechanism accounting for the initial reversible capacity of 6 Li can be written:



6.4 Conclusions

In this system, the relatively high electronic conductivity of CoP_3 enhances initial electronic transport within the electrode material and facilitates the decomposition process. After discharge, the high ionic conductivity of Li_3P of 10^{-3} S/cm, a property that has spurred its investigation as a solid electrolyte,²⁴ promotes Li^+ ion transfer within the composite matrix. The X-ray and electron diffraction data clearly show that cobalt is in a highly dispersed state in both the discharged and charged materials. This morphological disorder precludes the investigation of its role (if any) in the redox process. It apparently acts as an “active spectator” after initial discharge since bulk metallic cobalt does not form. The high degree of Co dispersion and bonding to the Li-P matrix may nonetheless enhance Li transport by grain boundary effects.

The fact that neither CoP_3 nor amorphous forms of cobalt phosphide are

regenerated on charge sets this mechanism apart from transition metal oxides, where partial or complete recuperation of the oxide structure occurs.^{2,25} This can be rationalized from a thermodynamic point of view. Formation of LiP, which has a higher lattice energy, hinders the restoration of the starting material CoP_3 upon charge, even as nano-crystallites. On the other hand, highly lithiated ternary phases, *i.e.* Li_xCoP_y with x and y larger than one, are not expected to be present in the discharged material given that these do not exist in the Li-Co-P phase diagram. Notwithstanding, based on the absence of metallic cobalt in the fully reduced material, the system can be regarded as a highly dispersed, phase-separated metastable analog of the transition metal oxides.

The suggested reaction mechanism for electrochemical lithium uptake/extraction by CoP_3 is exactly the same proposed by Alcántara *et al.* This corroborates the validity of the results since the two research groups independently reached the same conclusions.

References

- [1] Idota, Y. US Patent, 548671, 1995.
- [2] Leroux, F.; Goward, G.; Power, W.; Nazar, L. *Electrochem. Solid State Lett.* **1998**, *1*, 255.
- [3] Leroux, F.; Nazar, L. Materials for Batteries and Fuel Cells. In , Vol. 575; Doughty, D.; Nazar, L.; Arakawa, M.; Brack, H.-P.; Naoi, K., Eds.; MRS: Pennsylvania, 2000.
- [4] Denis, S.; Baudrin, E.; Orsini, F.; Oувrard, G.; Touboul, M.; Tarascon, J.-M. *J. Power Sources* **1999**, *81*, 79.
- [5] Obrovac, M.; Dunlap, R. A.; Sanderson, R.; Dahn, J. R. *J. Electrochem. Soc.* **2001**, *148*, A576.
- [6] Biltz, W.; Heimbrecht, M. *Z. Anorg. Allg. Chem.* **1939**, *241*, 238.
- [7] Rundqvist, S.; Ersson, N.-O. *Arkiv för Kemi* **1968**, *Bd.30*, 103.

- [8] Lefebvre-Devos, I.; Lassalle, M.; Wallart, X.; Olivier-Fourcade, J.; anJ.C. Jumas, L. M. *Phys. Rev. B: Condens. Matter* **2001**, *63*, 125110.
- [9] Alcántara, R.; Tirado, J.; Jumas, J.; Monconduit, L.; Oliier-Fourcade, J. *J. Power Sources* **2002**, *109*, 308.
- [10] Pralong, V.; Souza, D.; Leung, K.; Nazar, L. F. *Electrochem. Comm.* **2002**, *4*, 516.
- [11] Zhang, Z.; Yang, J.; Nuli, Y.; Wang, B.; Xu, J. *Solid State Ionics* **2005**, *176*, 693.
- [12] Jolibois, *Electrochem. Solid State Lett.* **1900**, *2*, A21.
- [13] Larson, A.; Dreele, R. V. “General Structure Analysis System (GSAS)”, Technical Report LAUR 86-748, Los Alamos National Laboratory, 2000.
- [14] Toby, B. *J. Appl. Crystall.* **2001**, *34*, 210.
- [15] Rietveld, A. *Acta Cryst.* **1967**, *22*, 151.
- [16] Howard, C. *J. Appl. Crystall.* **1982**, *15*, 615.
- [17] “JCPDS file number 29-496”, .
- [18] Weppner, W.; Huggins, R. *Ann. Rev. Mater. Sci.* **1978**, *8*, 269.
- [19] Alcántara, R.; Fernandez-Madrigal, F.; P. Lavela, J. T.; Jumas, J.-C.; Olivier-Fourcade, J. *J. Chem. Mat.* **1999**, *9*, 2517.

- [20] Fultz, B.; Howe, J. *Transmission Electron Microscopy and Diffractometry of Materials*; Springer-Verlag: Berlin, 2001.
- [21] Treacy, M. NEC, Princeton Labs, Private Communication, 2002.
- [22] Imamura, S.; Ishida, S.; Tarumoto, H.; Saito, Y.; Ito, T. *J. Chem. Soc., Faraday Trans.* **1993**, *89*, 757.
- [23] Chastain, J., Ed.; *Handbook of X-ray Photoelectron Spectroscopy*; Perkin Elmer Corporation: Eden Prairie, 1992.
- [24] Nazri, G. *Solid State Ionics* **1989**, *34*, 97.
- [25] Poizot, P.; Laruelle, S.; Grugeon, S.; Dupont, L.; Tarascon, J.-M. *Nature* **2000**, *407*, 496.

Chapter 7

Conclusions

7.1 Summary

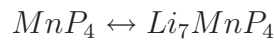
This thesis highlights the importance of the anion in the electrochemical uptake of lithium by metal phosphides. Data from a variety of *in-situ* and *ex-situ* analytical techniques prove that the redox active centers in three different systems (MnP_4 , FeP_2 , and CoP_3) are not necessarily cationic but can be based almost entirely on the anionic network.

The electrochemical processes responsible for reversible Li uptake/extraction in transition metal phosphides depends on the transition metal, and as to whether binary and lithiated ternary phases with the same M:P stoichiometry exist in the phase diagram. The reaction mechanism also depends on the structure of the starting

phase.

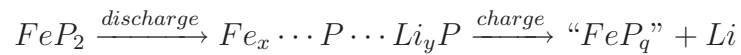
According to the results presented in the previous chapters, the behaviour of transition metal phosphides towards Li intake can be classified as:

- A. Both binary and lithiated ternary phases of the transition metal exist. In this case a topotactic phase transformation between binary and ternary phases occurs upon lithium uptake and removal:

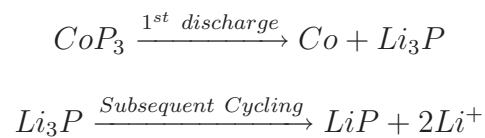


- B. Only the binary phase exists. In this case two different behaviours are observed:

Type I: Lithium uptake leads to the formation of an amorphous material in which short-range order is maintained:



Type II: Lithium uptake causes phase decomposition of the transition metal phosphide forming lithium phosphide which becomes the active material:



Of the results presented here, some comprise major scientific contributions. First, the electrochemically induced reversible crystalline phase transformation outlined

in Chapter 4 represents an exciting finding. With the exception of intercalation reactions, crystalline transformations in the solid state are kinetically hindered and typically occur on geological time scales without the benefit of high temperature, owing to the difficulty of transport within the bulk. Cobalt phosphide displays electrochemical activity towards lithium *via* a disproportionation reaction (see above); in FeP_2 discharge generates an amorphous matrix in which iron is in close contact with phosphorus. These results are of both fundamental and technological interest since they depart from the intercalation or alloying reactions normally observed in lithium-ion battery chemistry.

Secondly, unlike most intercalation compounds that accommodate guest species by redox chemistry at the cationic centers, in metal phosphides it is primarily the anion that undergoes the redox reaction. The cleavage of the covalent P–P bonds is undoubtedly a consequence of the strong anion character of the uppermost filled electronic band.

Third, the three systems studied exhibit very high initial capacities, up to 3 times the specific capacity of carbon, constituting excellent alternative anode materials for carbon in lithium ion batteries. This fact alone has triggered many research groups to investigate other transition metal phosphides, although the cycleability of the electrodes needs improvement.

7.2 Future Work

As stated before, many transition metal phosphides have been examined after we first published our initial results. Nevertheless, the surveys published so far are just the tip of the iceberg. From a technological point of view, transition metal phosphides are attractive materials, but their electrochemical performance needs improvement. For this purpose, some key aspects need further investigation:

- Side reactions between electrode and electrolyte components;
- Effect of additives on the stability window of electrolytes during electrochemical reaction and on mechanism for lithium uptake/extraction;
- Nature of the solid electrolyte interface formed, if any.
- Effect of particle micro-structure control on structural interconversion.